

1995

NDE data fusion using phenomenological approaches

Kai Sun

Iowa State University

Follow this and additional works at: <https://lib.dr.iastate.edu/rtd>



Part of the [Electrical and Electronics Commons](#)

Recommended Citation

Sun, Kai, "NDE data fusion using phenomenological approaches " (1995). *Retrospective Theses and Dissertations*. 11092.
<https://lib.dr.iastate.edu/rtd/11092>

This Dissertation is brought to you for free and open access by the Iowa State University Capstones, Theses and Dissertations at Iowa State University Digital Repository. It has been accepted for inclusion in Retrospective Theses and Dissertations by an authorized administrator of Iowa State University Digital Repository. For more information, please contact digirep@iastate.edu.

INFORMATION TO USERS

This manuscript has been reproduced from the microfilm master. UMI films the text directly from the original or copy submitted. Thus, some thesis and dissertation copies are in typewriter face, while others may be from any type of computer printer.

The quality of this reproduction is dependent upon the quality of the copy submitted. Broken or indistinct print, colored or poor quality illustrations and photographs, print bleedthrough, substandard margins, and improper alignment can adversely affect reproduction.

In the unlikely event that the author did not send UMI a complete manuscript and there are missing pages, these will be noted. Also, if unauthorized copyright material had to be removed, a note will indicate the deletion.

Oversize materials (e.g., maps, drawings, charts) are reproduced by sectioning the original, beginning at the upper left-hand corner and continuing from left to right in equal sections with small overlaps. Each original is also photographed in one exposure and is included in reduced form at the back of the book.

Photographs included in the original manuscript have been reproduced xerographically in this copy. Higher quality 6" x 9" black and white photographic prints are available for any photographs or illustrations appearing in this copy for an additional charge. Contact UMI directly to order.

UMI

A Bell & Howell Information Company
300 North Zeeb Road, Ann Arbor, MI 48106-1346 USA
313/761-4700 800/521-0600



NDE data fusion using phenomenological approaches

by

Kai Sun

**A Dissertation Submitted to the
Graduate Faculty in Partial Fulfillment of the
Requirements for the Degree of
DOCTOR OF PHILOSOPHY**

**Department: Electrical and Computer Engineering
Major: Electrical Engineering (Communications and Signal Processing)**

Approved:

Signature was redacted for privacy.

In Charge of Major Work

Signature was redacted for privacy.

For the Major Department

Signature was redacted for privacy.

For the Graduate College

Members of the Committee:

Signature was redacted for privacy.

**Iowa State University
Ames, Iowa**

1995

Copyright © Kai Sun, 1995. All rights reserved.

UMI Number: 9610993

**Copyright 1995 by
Sun, Kai
All rights reserved.**

**UMI Microform 9610993
Copyright 1996, by UMI Company. All rights reserved.**

**This microform edition is protected against unauthorized
copying under Title 17, United States Code.**

UMI

**300 North Zeeb Road
Ann Arbor, MI 48103**

TABLE OF CONTENTS

ACKNOWLEDGMENTS	vii
ABSTRACT	viii
CHAPTER I. INTRODUCTION	1
1.1 Overview of Nondestructive Evaluation	1
1.2 Data Fusion in NDE	4
1.3 Phenomenological NDE Study	4
1.4 Scope of the Dissertation	8
CHAPTER II. MODELING OF EDDY CURRENT PHENOMENA	10
2.1 Overview of Eddy Current NDE	10
2.2 Electromagnetic Governing Equation	16
2.3 Eddy Current as a Random Process	19
2.4 Eddy Current as a Diffusion Process	26
2.5 Green's Function for Eddy Current Diffusion Process	30
2.6 Eddy Current Modeling of Flaw Signals	37
2.7 Analytical Modeling of the Electromagnetic Field	44
CHAPTER III. WAVE NDE MODELING	80
3.1 Electromagnetic Wave Scattering	80
3.2 Ultrasonic Wave Scattering	87
3.3 Degradation of Ultrasonic Signals	98
CHAPTER IV. DATA FUSION	101
4.1 Introduction to Data Fusion	101
4.2 Data Fusion Systems	102
4.3 Data Fusion Applications	111
4.4 Data Fusion for NDE Applications	113

CHAPTER V. DATA FUSION USING Q-TRANSFORMATION	117
5.1 Introduction to Q-Transformation	118
5.2 Properties of Q-Transformation	122
5.3 Q-Transformation in NDE Applications	132
5.4 Q-Transformation for Registration of the Ultrasonic and Eddy Current Data	140
CHAPTER VI. CONCLUSIONS AND FUTURE WORK	149
6.1 Summary of Dissertation	149
6.2 Future Work	151
BIBLIOGRAPHY	152

LIST OF FIGURES

Figure 1.1.	Block diagram of a generic NDE system	2
Figure 2.1.	Generic eddy current NDE setup	12
Figure 2.2.	Characteristic eddy current excitation coil impedance change	12
Figure 2.3.	A typical differential probe used for inspecting tubes	14
Figure 2.4.	Differential coil impedance plane trajectory	14
Figure 2.5.	Typical eddy current image	15
Figure 2.6.	(a). Schematic representation of an electron with a lattice atom; (b). Velocity of electrons due to an electrostatic force and a counteracting damping force. The electron eventually reaches the final velocity	22
Figure 2.7.	Green's function for diffusion for one dimension case, as a function of R for different times t . $t_1 < t_2 < t_3 < t_4$	33
Figure 2.8.	The Green's functions including the wave term, plotted for different c 's. $c_1 < c_2 < c_3 < c_4$. The time instant is the same as t_1 in Figure 2.7	35
Figure 2.9.	Coordinate of eddy current setup with a conducting half plane	47
Figure 2.10.	Magnetic vector potential variation in the z direction for a finite cross-section coil	51
Figure 2.11.	Magnetic vector potential variation in the r direction	52
Figure 2.12.	Induced voltage change by a tiny flaw as a function of the radial distance r from the center	53
Figure 2.13.	Contour of magnetic vector potential distribution, amplitude	54
Figure 2.14.	Contour of magnetic vector potential distribution, phase	55
Figure 2.15.	Constant magnetic flux density lines over space	56
Figure 2.16.	Model configuration with a conducting slab	57

Figure 2.17.	Induced voltage in pickup coil, same copper slab, different pickup coil locations	68
Figure 2.18.	Induced voltage in pickup coil, different copper slab thickness	69
Figure 2.19.	Flaw kernel of induced voltage for a flaw near the top of the specimen	70
Figure 2.20.	Flaw kernel of induced voltage for a flaw at the middle of the specimen	71
Figure 2.21.	Signal generated due to a flaw at $(r, z) = (1.0, -0.5 \text{ mm})$ excited by a 0.1 ms wide pulse	72
Figure 2.22.	Signal generated due to a flaw at $(r, z) = (3.0, -0.5 \text{ mm})$ excited by a 0.1 ms wide pulse	73
Figure 2.23.	Real part of A , $f = 100 \text{ GHz}$	74
Figure 2.24.	Imaginary part of A , $f = 100 \text{ GHz}$	75
Figure 2.25.	Magnitude of A , $f = 100 \text{ GHz}$	76
Figure 2.26.	Phase of A , $f = 100 \text{ GHz}$	77
Figure 2.27.	Amplitude of flaw magnetic time signal over r direction	78
Figure 2.28.	Image of the flaw magnetic field	79
Figure 3.1.	Scattered electromagnetic energy by a tiny flaw	86
Figure 3.2.	Ultrasonic NDE setup in pulse-echo mode	89
Figure 3.3.	Ultrasonic NDE output signal	90
Figure 3.4.	The raised-cosine excitation signal used in modeling studies	93
Figure 3.5.	Fourier transformation of the raised-cosine excitation signal	93
Figure 3.6.	Ultrasonic A-scan signal with flaw	94
Figure 3.7.	Ultrasonic A-scan signal without flaw	95
Figure 3.8.	Ultrasonic A-scan signal due to flaw	96
Figure 3.9.	Ultrasonic C-scan image	97

Figure 4.1.	A generic data fusion system model	102
Figure 4.2.	Centralized data fusion architecture	107
Figure 4.3.	Autonomous data fusion architecture	108
Figure 5.1	Eddy current and ultrasonic data registration approach using Q-transform	117
Figure 5.2.	Time shifted signal $U_2(q)$ vs. the original signal $U_1(q)$	130
Figure 5.3.	Smearing kernel $h(t)$	131
Figure 5.4.	Ultrasonic scattering signal	141
Figure 5.5.	Eddy current change of magnetic field signal	142
Figure 5.6.	Q-transform of the ultrasonic wave scattering signal	143
Figure 5.7.	Q-transform of the raised cosine function with duration = 3.0×10^{-7} s	144
Figure 5.8.	FFT of the raised cosine function Q-transform	145
Figure 5.9.	Eddy current signal with driving current corresponding to the Q-transform of the raised cosine function	146
Figure 5.10.	Q-transform of time shifted wave signals	147

ACKNOWLEDGMENTS

I would like to express my sincere gratitude to my advisor, Dr. Satish S. Udpa, for his invaluable guidance, support and encouragement throughout my graduate program. He is a respectable person for me not only as a professor but also as a senior of life. His professional and personal guidance will be beneficial to me for a life time.

I would like to extend my thanks to Dr. Lalita Udpa, Dr. William Lord, Dr. Jennifer Davidson, Dr. Yushi Sun and Dr. Sharon Filipowski for willingly taking the time to serve on my graduate committee. I also appreciate them for sharing their rich knowledge and helpful discussions. Thanks are also due to Mr. T. Xue who performed most of the ultrasonic finite element modeling work.

I would particularly like to express my thanks to my family: my dear wife Helen (Hong) Gao, and my son Daniel Sun, for their sacrifice, encouragement and patient support, as well as the joys they bring to me. Also, special thanks are due my parents, who sacrificed so much to make my dreams come true.

Finally but not the least, I would like to thank many friends here at Ames, whose advice, thoughts, expertise and friendship have enriched my life.

ABSTRACT

Data fusion techniques are beginning to attract considerable attention. In the NDE context, such techniques can be used to combine information from two or more NDE test methods to improve the probability of detection and enhance characterization results. An example of such an application involves the fusion of eddy current and ultrasonic NDE data. The eddy current phenomena relies on the diffusion process to propagate energy. Ultrasonic phenomena, in contrast, rely on wave propagation. The manner in which the energy interacts with the material under test is fundamentally different. It can therefore be argued that each test method provides a different perspective and consequently approaches that allow data from the two test methodologies to be fused have the potential for offering an improved understanding of the condition of the material.

This dissertation presents an incremental step towards the development of a very novel phenomenological approach to data fusion. The method involves mapping of the wave field to a diffusion field using Q-transforms. The transformed and diffusion fields are then combined to synthesize the fused image. A systematic study of the issues involved in fusion and the registration of the data was conducted. The study was accomplished by developing and using a two-dimensional analytical model that includes both the diffusion and wave propagation contributions. The ultrasonic tests were simulated using an existing finite element model. The dissertation presents results obtained by transforming the ultrasonic data into the diffusion domain. The effect of Q-transform properties, especially its time shift property, on data registration is analyzed. A modified version of the Q-transform is also

presented to overcome the problems associated with large differences in the values of the underlying partial differential equation coefficients. Theoretical results obtained using the approach together with a discussion on additional work that needs to be undertaken are presented.

CHAPTER I. INTRODUCTION

1.1 Overview of Nondestructive Evaluation

Nondestructive evaluation (NDE) is used in industry to assess the character of structures and materials non-invasively. This differs from destructive testing methods in which a material must in some way be modified to determine its properties. NDE techniques are used widely in the inspection of aircraft, railroads, ships, gas pipelines and numerous other structures which have the potential of catastrophic failure. As examples, NDE is used periodically to determine the presence of anomalies and corrosion in underground gas pipelines and nuclear steam generator tubing.

To be able to provide quantitative results, NDE must not only detect flaws in structures, but also characterize the exact nature of the flaws in order to be able to assess the risk they pose to the overall integrity of the structure. This is important because flaws can often exist for many years without inducing failures. It would be inefficient to declare a structure as unsafe based on the presence of a small flaw when in reality the flaw may remain benign for a number of years or operational cycles. Therefore, the challenge in NDE is to be able to characterize flaws quantitatively in order to determine if a defect is benign or catastrophic.

A block diagram of a generic NDE system is shown in Figure 1.1. A typical NDE procedure involves application of an appropriate form of energy to the test specimen. The material/energy interaction process is then observed through an output transducer. The signal

from the transducer is processed and analyzed to determine the size, shape and location of the flaw. NDE techniques can be classified on the basis of the type of energy that is employed in interrogating the test specimen. A variety of NDE methods utilizing a diverse range of energy sources have been proposed. These include ultrasonic, electromagnetic, thermal, radiographic, visual and optical techniques.

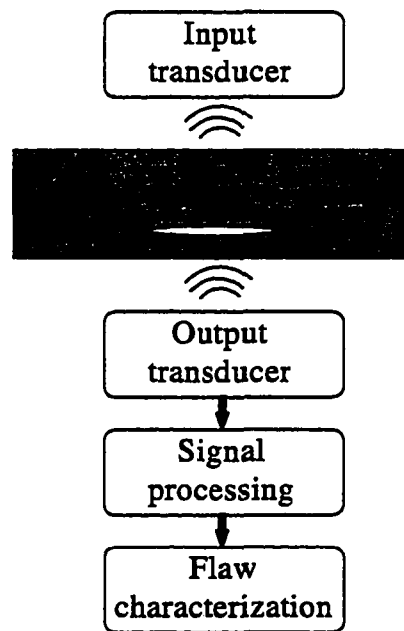


Figure 1.1. Block diagram of a generic NDE system

The methods used in nondestructive evaluation are based on a variety of principles [62, 66], ranging from static methods, to quasi-static and wave based methods. Static techniques include magnetostatic and residual methods. As an example, magnetic particle testing [89, 90] is done by inducing a magnetic field in a ferro-magnetic material and dusting

the surface with iron particles. Surface imperfections distort the magnetic field and concentrate the iron particles near the imperfections, thus indicating their presence. Magnetic flux leakage (MFL) techniques [91, 92, 93] directly measure the magnetic flux density over a ferro-magnetic sample surface. The measured magnetic leakage field is used to identify the presence of flaws as well as to determine their shape, size and location. Similarly, residual leakage field techniques [94, 95] measure the leakage fields which are set up around defects in ferromagnetic materials after the active source of d.c. excitation has been removed.

Diffusion based methods include eddy current and thermal techniques. In eddy current tests [83, 84], electric currents are generated in a conductive test sample by an induced magnetic field. Interruptions in the flow of the electric currents by flaws will cause changes in the induced magnetic field. Perturbations in the field values indicate the presence of flaws and provide information for characterizing them. Thermal methods are increasingly being used to inspect composite and other materials. As an example, thermal techniques [96, 97] are used to measure the thermal conductivity of homogeneous and inhomogeneous multilayered materials.

Wave based methods include electromagnetic/microwave and ultrasonic techniques. Microwave NDE uses electromagnetic waves at very high frequencies to interrogate the test sample [67, 68, 98, 99]. It generally involves measuring the waves scattered by, or transmitted through the sample. Signals scattered from the flaws and sample property variations are used as a basis for characterizing the sample. Ultrasonic NDE relies on the transmission of high frequency sound waves into a material to detect imperfections or

changes in the material properties. Signals representing reflections (echoes) from internal flaws and from geometrical boundaries are utilized to characterize the test specimen. Each type of NDE method has its own special characteristics and, therefore, has its own unique set of applications.

1.2 Data Fusion in NDE

Each NDE technique provides some information concerning the condition of the test specimen. The nature of the information is dependent on the type and propagation mode associated with the energy used to excite the material under test. Some of the data generated by a test may overlap with data provided by other tests. The rest of the data may either be redundant or complementary. It is therefore advantageous to combine or fuse data from several tests to obtain more comprehensive information about the test object [86, 87]. The objective of the research is to model eddy current and ultrasound NDE processes and to develop procedures for fusing NDE data from multiple tests. More specifically, issues relating to the registration of eddy current and ultrasound data are investigated. This dissertation also explores the feasibility of using Q-transforms as a tool for performing the data registration.

1.3 Phenomenological NDE Study

The application of electromagnetic nondestructive evaluation (NDE) techniques has a long history. Advances in computer technologies have provided powerful computational tools for modeling the electromagnetic process and gaining a greater understanding of the

physical principles underlying a variety of NDE methods. This has helped a great deal in promoting the rapid application of electromagnetic methods in nondestructive evaluation. The application of electromagnetic NDE can be found in a number of industries, including the gas, oil and aerospace industries.

Research in NDE modeling is mainly concerned with the development of forward and inverse models [63, 64, 65]. Forward models are concerned with simulating the underlying physical process and provide an alternative to experimental testing of various setups. The use of such models provides valuable insight into the physics underlying the test method. Such models can also serve as a source of data for developing inverse models.

Eddy current NDE method, which is one of the two methods being studied as part of this research, rely for their operation on the use of a coil excited by an alternating current source to establish the primary field. This in turn induces secondary currents and fields in the specimen undergoing inspection. Defects in the specimen cause changes in both induced currents and fields, resulting in measurable impedance variations in a nearby pickup coil. The process can be observed using experimental techniques or through simulation using either numerical or analytical models.

Experimental models are those that are based on data obtained from measurements on actual eddy current NDE test rigs. Although such experimental tests are useful for validation studies, they tend to be inflexible and cannot be readily extended to include a wide variety of test configurations and defect shapes that are necessary for the development of realistic defect characterization schemes.

Numerical models can be employed to mimic the experimental test by solving the governing field equations. These models typically involve discretization of the region of interest. The governing equation is then solved either directly or indirectly which ultimately leads to a matrix equation whose solution satisfies the original field equations.

Currently, a major portion of the thrust towards building forward models is focused on the use of numerical modeling techniques [1, 82]. Finite difference [80, 81, 82], finite element [1, 50, 54, 55, 57, 76] and boundary element methods [52, 79] are widely used for building such models. Numerical models have become a mature tool in NDE research and rapid advances in computing technology have accelerated their application.

Analytical models are those that are derived from basic field and circuit theory considerations. Instead of spatial and/or temporal discretization of the field, analytical models solve the field equations directly. Closed form solutions are obtained, usually in the form of an integral, for a specified eddy current setup. These models take into consideration such factors as specimen and defect symmetry and boundary conditions. Often the use of these analytical models is limited to applications with regular symmetry.

Analytical studies [1, 2, 88] of electromagnetic NDE phenomena are not as popular as numerical models. This does not imply that analytical tools are less important or less interesting; it merely reflects the difficulty involved in developing analytical models. Also, analytical NDE research is limited to applications where sample boundaries are simple, and where the defect to be modeled has an analytically expressible form. Despite the difficulties involved, and limited practical applications, analytical NDE models are a powerful tool for

understanding the underlying physical process. In this research, an analytical eddy current model is employed.

A number of approaches have been applied to eddy current signal processing [100]. Direct inversion can be performed when a mathematical relationship relating the measured fields to the character of the test structure exists [104]. Direct inversion schemes are often limited to highly special cases where the shape of the defect is often known a priori. As a result, many indirect inversion methods have been proposed. One commonly used technique is to employ calibration curves [105-107]. Such curves, relating the measurement variable and specific defect characteristic of interest, are derived using experimental data or results generated using forward models. Alternative approaches involve treatment of the characterization problem as a classification problem. Such approaches use such tools as neural networks [64, 65, 101] and pattern classification [102, 103, 117] for flaw identification and classification. A variety of transformations and signal processing techniques [63, 108] are used for extracting features that are relevant for discriminating between signals. However, they all fall into the category of heuristic approaches. Future successes will hinge critically on our ability to use the underlying physics as a basis for developing signal processing techniques. Attention is increasingly being focused on the study of the physical meaning of procedures used for processing eddy current NDE signals. This is important since it can provide guidance for extracting features for signal processing and for making use of the features in a more meaningful way.

1.4 Scope of the Dissertation

The first step in the fusion algorithm is data alignment and registration. This is further explained in Chapter 4. For a data fusion system using heterogeneous sensors [24, 109], data registration is required to relate individual sensor measurements to each other and to determine how they can be grouped and transformed into the same format.

The goal of the research is to investigate data registration issues for combining eddy current and ultrasonic NDE signals. Analytical and numerical models characterizing electromagnetic and ultrasonic wave scattering are used to provide a basis and rationale for identifying candidate wave signal features for data fusion. Although numerical studies are far more flexible, this dissertation reports the use of an analytical formulation that is potentially capable of providing information for establishing closed-form relations between the output signals and the corresponding sample/flaw properties.

Eddy current signals are derived from phenomena that are essentially diffusive in nature and consequently have characteristics that are different relative to signals derived from wave based processes. For data fusion, proper registration of the eddy current data with wave data is necessary. This dissertation explores the use of Q-transforms as a technique for performing the registration.

The dissertation is organized as follows. Chapter 2 is devoted to eddy current modeling. The chapter includes a discussion on eddy current as a diffusion process, presents the applicable Green's function, as well as describes a closed form model simulating a two dimensional eddy current test geometry. Chapter 3 is concerned with wave scattering in

general and ultrasonic wave scattering processes in particular. A finite element ultrasonic NDE model simulating the experimental configuration is presented. In Chapter 4, the concept of data fusion is presented. Issues in data fusion, including the topic of data registration are outlined. Chapter 5 describes the Q-transform together with its properties and its potential application in NDE as a technique for registering eddy current and ultrasonic data. Results and discussions relating to the issue are presented. Finally, Chapter 6 presents some concluding remarks and suggests potential areas for pursuing research in the future.

CHAPTER II. MODELING OF EDDY CURRENT PHENOMENA

2.1 Overview of Eddy Current NDE

2.1.1 Background

Figure 1.1 shows the five essential ingredients of a complete NDE system. Among these steps, the interpretation of the defect signal represents the most important stage. This stage generates information regarding the flaw size, shape and location. Recent progress in developing a solution to the inversion problem has become possible only due to the development of viable theoretical models that are capable of simulating the interactions of many variables influencing the measured signal.

Good theoretical models in NDE can be used to gain an understanding of the interaction between the incident energy and the test specimen and to serve as a theoretical test bed to determine the output signal in situations where an experimental simulation is either difficult or impossible. They can also be employed to obtain probe output signals for a variety of defects, avoiding expensive and time consuming defect sample preparation. These theoretically generated signals can be used to identify defect characterization parameters and to train signal analyzers.

The governing equations describing electromagnetic phenomena are well known, yet direct solutions to these equations are not easily obtained because of the nonlinear and frequency dependent properties of ferromagnetic and electrically conducting materials and awkward boundary conditions. Classical closed form solutions of the eddy current problem

have been obtained using multiple integrals of ordinary and modified Bessel functions, Fourier transforms, etc. In general, simplifying approximations have to be made with regard to the number of dimensions, linearity of material properties, setup symmetry, boundary conditions and the defect shape, size and location to obtain an analytical result.

2.1.2 Generic eddy current NDE

In a generic eddy current NDE setup, an exciting coil is placed above the sample under test. A pulse or sinusoidal current is applied to the exciting coil. This current generates a magnetic field around the coil, including the space occupied by the test specimen. The magnetic field interacts with the sample. The interaction is observed through a second pickup coil. The voltage induced in the pickup coil potentially contains information about the sample under investigation. As an example, one could infer the sample magnetic and electrical properties, measure the sample physical size, detect the presence of any flaws within the sample or estimate the flaw size, shape and location of the defect based on information contained in the signal. It must be mentioned that in many eddy current NDE setups, the exciting coil is also used as a pickup coil. A generic eddy current setup is shown in Figure 2.1.

When the eddy current excitation is sinusoidal, the interaction between the magnetic field and the test specimen is characterized by a change in the excitation coil impedance. The characteristic excitation coil impedance change behavior is shown in Figure 2.2. When the excitation coil is away from a conducting test specimen, the coil has an intrinsic resistance R_0 and inductance L_0 . This corresponds to the point O in the figure. When the coil is

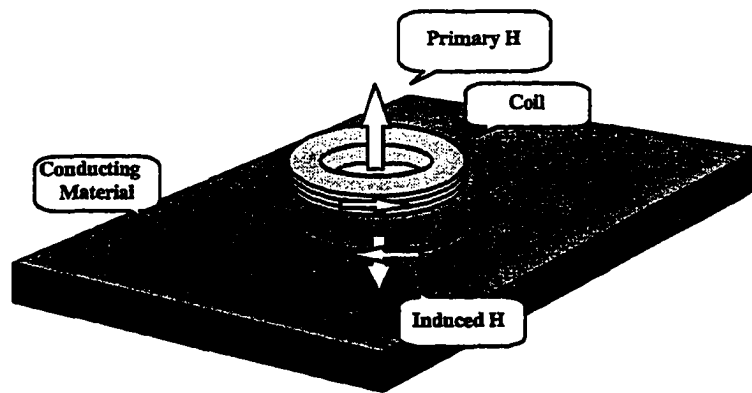


Figure 2.1. Generic eddy current NDE setup (after Yim [86])

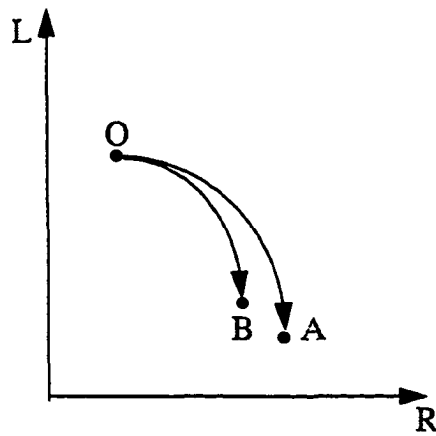


Figure 2.2. Characteristic eddy current excitation coil impedance change

moved closer to a conducting material, the time varying magnetic field induces eddy currents in the material. The eddy current energy dissipation manifests itself in the form of an increase in the resistance of the coil. At the same time, the induced eddy current generates a secondary magnetic field which opposes the field established by the primary coil. This results in a decrease in the coil inductance and corresponds to the point *A* in the impedance plane. When there are flaws inside the specimen, the effective excitation coil is not perturbed as much. In most cases, the conductance of a flaw is smaller than that of the specimen. Consequently the change in impedance is less pronounced. This corresponds to the point *B* in the figure. By monitoring the impedance change, one can in principle, detect the presence of flaws in the test specimen.

In many eddy current applications, a differential pickup coil is used. A typical differential probe used for inspecting tubes is shown in Figure 2.3. The probe consists of two identical coils mounted on the same axis as the tube but spaced apart by a small distance, forming two arms of a bridge circuit. A differential coil is sensitive only to changes in the specimen characteristics and therefore offers better sensitivity. As an example, when a differential probe shown in Figure 2.3 passes across a flaw, an impedance plane trajectory shown in Figure 2.4 is produced. The crossover point corresponds to the signal background level, or baseline.

When a test specimen is scanned and the magnitude of the impedance change is recorded for each probe location, a two-dimensional eddy current image is obtained. Figure 2.5 shows an image obtained by scanning a specimen containing a surface breaking crack.

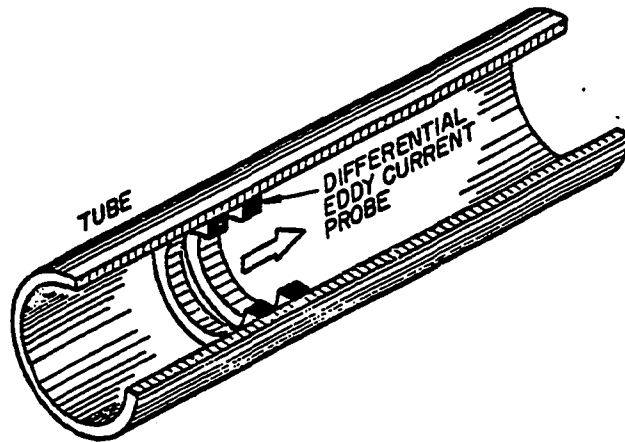


Figure 2.3. A typical differential probe used for inspecting tubes (after Udpa [117])

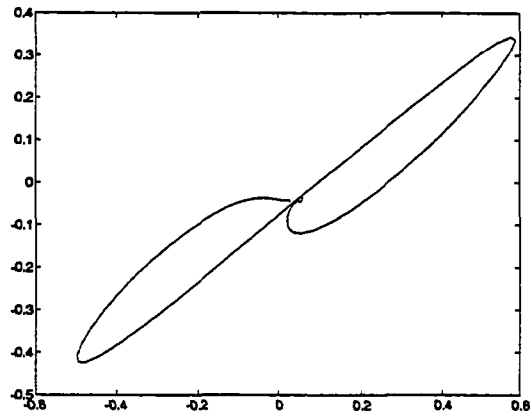


Figure 2.4. Differential coil impedance plane trajectory

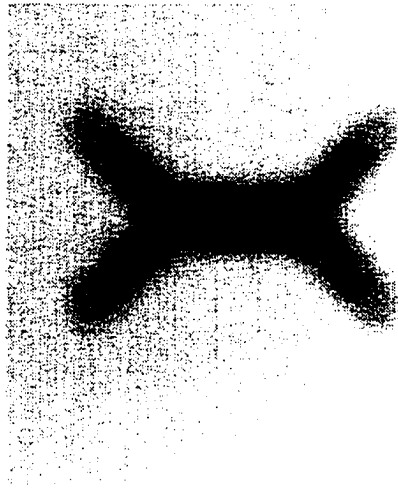


Figure 2.5. Typical eddy current image

When the eddy current excitation is non-sinusoidal, it is not possible to use impedance measurements as a basis for defect characterization. In such cases, the induced voltage in the pickup coil, or the magnetic flux density as measured by a Hall probe, can be used for analysis [69, 70]. The issue will be discussed in greater detail in Section 2.6.

In the following sections, the electromagnetic governing equations for eddy current and wave propagation cases are first derived from Maxwell's equations. The results are used as the starting point for modeling eddy currents in materials. The eddy current phenomenon is then viewed as a random process to gain an understanding of the underlying physics at a more fundamental level. The energy propagation process associated with eddy currents as well as the Green's function characterizing the phenomenon is presented. Finally, an analytical two dimensional eddy current model is presented.

2.2 Electromagnetic Governing Equation

We begin with Maxwell's equations:

$$\begin{aligned}
 \nabla \times \vec{E} &= -\partial \vec{B} / \partial t \\
 \nabla \times \vec{H} &= \vec{J} + \partial \vec{D} / \partial t \\
 \nabla \cdot \vec{D} &= \rho_0 \\
 \nabla \cdot \vec{B} &= 0
 \end{aligned}
 \tag{2.1}$$

where \vec{E} is the electrical field intensity, \vec{H} is the magnetic field intensity, \vec{D} is the electrical flux density, \vec{B} is the magnetic flux density, \vec{J} is the current density and ρ_0 is the electrical charge density.

The constitutive relations between \vec{E} and \vec{D} , \vec{B} and \vec{H} , \vec{J} and \vec{E} are given by:

$$\begin{aligned}
 \vec{D} &= \epsilon \vec{E} \\
 \vec{B} &= \mu \vec{H} \\
 \vec{J} &= \sigma \vec{E},
 \end{aligned}
 \tag{2.2}$$

where ϵ is the electric permittivity, μ is the magnetic permeability, and σ is the electrical conductivity.

If we define two other variables: \vec{A} , the magnetic vector potential, and ϕ , the electrical scalar potential, then,

$$\begin{aligned}
 \vec{B} &= \nabla \times \vec{A} \\
 \vec{E} &= -\nabla \phi - \partial \vec{A} / \partial t.
 \end{aligned}
 \tag{2.3}$$

To obtain a unique \vec{A} and ϕ corresponding to a given electromagnetic field distribution, we force \vec{A} and ϕ to satisfy the Lorentz gauge:

$$\nabla \cdot \vec{A} + \frac{1}{c^2} \frac{\partial \phi}{\partial t} = 0. \quad (2.4)$$

From Maxwell's equations, one can derive the following governing equation for the magnetic vector potential \vec{A} in an electric charge free medium:

$$\nabla \times \left(\frac{1}{\mu} \nabla \times \vec{A} \right) - \mu \nabla \left(\frac{1}{\mu} \nabla \cdot \vec{A} \right) = \vec{J}_0 - \sigma \frac{\partial \vec{A}}{\partial t} - \epsilon \frac{\partial^2 \vec{A}}{\partial t^2}. \quad (2.5)$$

There are two terms in the governing equation for \vec{A} . One involves the first derivative of \vec{A} with respect to time t , the other one the second time derivative of \vec{A} . The first term describes a diffusion component of the field \vec{A} , while the second term describes the wave propagation behavior. We will label the two terms as the diffusion term and wave term, respectively.

In lossless media, the electrical conductivity σ is zero and the diffusion term disappears. The wave and the source current term govern the field behavior. This corresponds to a standard wave propagation equation:

$$\nabla \times \left(\frac{1}{\mu} \nabla \times \vec{A} \right) - \mu \nabla \left(\frac{1}{\mu} \nabla \cdot \vec{A} \right) = \vec{J}_0 - \epsilon \frac{\partial^2 \vec{A}}{\partial t^2}. \quad (2.6)$$

In low frequency situations, the contribution from the wave term is much smaller than the contribution from the source current term. The magnetic vector potential distribution is essentially described by the free current spatial distribution and its time variation. Thus the whole process is static in nature. As the frequency increases, the wave term begins to contribute noticeably to the field behavior, and consequently the process develops into a wave radiation problem.

In the case where the medium is lossy, such as in a conducting material, the diffusion term is much larger than the wave term. Therefore, the wave term can be ignored, and we obtain the well known eddy current diffusion equation that is described in most eddy current literature [1, 2, 6, 83, 84]:

$$\nabla \times \left(\frac{1}{\mu} \nabla \times \bar{A} \right) - \mu \nabla \left(\frac{1}{\mu} \nabla \bar{A} \right) = \bar{J}_0 - \sigma \frac{\partial \bar{A}}{\partial t}. \quad (2.7)$$

In this research, both the diffusion and the wave terms are studied. Both terms are included in the eddy current model to allow a variety of situations to be simulated. The model allows both low and high frequency processes to be simulated by choosing an appropriate value of σ . The model can as well be applied to situations in which the material conductivity is low and so the wave term makes a significant contribution to the overall magnetic vector potential distribution. Before proceeding to present the eddy current model, a brief discussion viewing eddy current as a random process is given.

2.3 Eddy Current as a Random Process

2.3.1 Introduction

The eddy current process is fundamentally a stochastic process. The interaction of a varying magnetic field with a conducting medium is through the free electrons in the conductor. The behavior of the electron movement is stochastic in nature.

In a conductor, when an external magnetic field changes, the free electrons are excited by the induced electrical field. The excitation and relaxation of the electrons cause energy dissipation in the process. This section describes eddy current process at the microscopic level, by studying the electron interaction with the induced electrical field. In Section 2.4, the eddy current diffusion process is studied at the macroscopic level.

2.3.2 Free electron relaxation time τ_R

Upon application of an electrical field (the induced electrical field in the eddy current case) to a conductor, the free electrons rearrange themselves to cancel the applied field exactly, assuming electrostatic conditions. The question is, how long does it take for this relaxation process to reach equilibrium? Assuming the conductor to be a continuous medium and without considering the underlying micro-physical process, the question can be answered by studying a set of equations including the electrical charge continuity equation, Ohm's law and Gauss' law [43, 44],

$$\begin{aligned}
\nabla \cdot \bar{\mathbf{j}} &= -\frac{\partial \rho}{\partial t} \\
\nabla \cdot \bar{\mathbf{E}} &= \frac{\rho}{\epsilon} \\
\bar{\mathbf{j}} &= \sigma \bar{\mathbf{E}}
\end{aligned}
\tag{2.8}$$

Combining the last two equations into the first continuity equation, one gets

$$\rho = -\frac{\epsilon}{\sigma} \frac{\partial \rho}{\partial t},
\tag{2.9}$$

the solution of which has a decaying form in terms of time:

$$\rho = \rho_0 e^{-\frac{\sigma}{\epsilon} t}
\tag{2.10}$$

with a characteristic relaxation time τ_R of

$$\tau_R = \epsilon / \sigma.
\tag{2.11}$$

The characteristic time calculated in this way for aluminum with $\sigma = 5.77 \times 10^7 \text{ S/m}$ and $\epsilon = \epsilon_0$ is $\tau_R = 1.5 \times 10^{-19} \text{ s}$. Based on this relaxation time calculation, for the eddy current process, the settlement of electrons is almost instantaneous compared with the time scale it takes for the electrical field to change.

2.3.3 Free electron mean time between collision τ_c

The exact random nature of the eddy current process comes from the electron collision with the atomic lattice structure in a metal [20]. The classical approach to describe

this, is to postulate a free “electron gas” or “plasma”, consisting of the valence electrons of the individual atoms in a crystal. In the absence of an external electrical field, the free electrons move randomly (in all possible directions) so that their individual velocities cancel and no net velocity results.

This situation changes when an electrical field is applied. Upon being subjected to an external electric field, the electrons are accelerated in the negative direction of the applied field. A net drift of electrons result. If the external electrical field is the only source asserting force on the electrons, the electrons would be constantly accelerated as long as an electrical field persists. After the field is removed, the electrons would keep drifting with constant velocity through the crystal. In reality, this is not observed except under superconducting conditions. The electron acceleration process does not continue without any interruption. In fact, a free electron is subject to continued collision with atoms in the lattice structure. It is assumed that the energy gained from the acceleration is lost every time an electron collides with an atom. The velocity of the electron settles back to a velocity corresponding to its band energy. Then the acceleration process starts over again. This continues as long as the external electrical field exists. The schematic representation of an electron within a lattice structure is shown in Figure 2.6(a). It is postulated that the resistance in metals and alloys is due to interactions of the drifting electrons with some lattice atoms, i.e., essentially with the imperfections in the crystal lattice, such as impurity atoms, vacancies, grain boundaries, dislocations, etc.

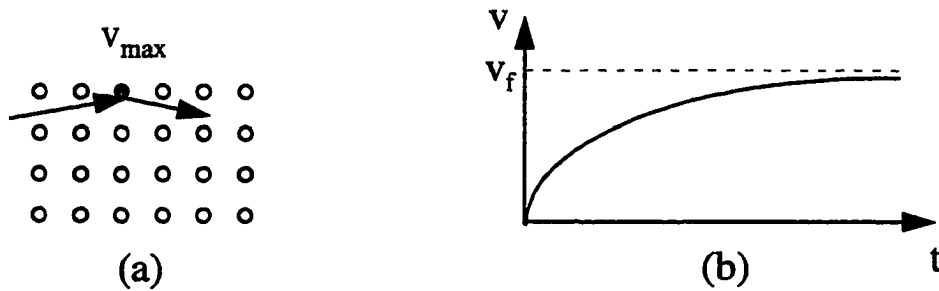


Figure 2.6. (a) Schematic representation of an electron with a lattice atom; (b) Velocity of electrons due to an electrostatic force and a counteracting damping force. The electron eventually reaches the final velocity.

The mean time between two consecutive collisions, τ_c , can be derived by studying the motion of the free electrons.

$$m \frac{\partial \vec{v}(\vec{r}, t)}{\partial t} = -e\vec{E}(\vec{r}, t) - \gamma\vec{v}(\vec{r}, t) \quad (2.12)$$

The left hand side is the acceleration rate of the electron multiplied by its mass. The two terms on the right hand side are the forces asserted on the electron. The first term is the force from the external electric field, being negative because an electron has a negative charge (-e). The second term is a damping force. It is derived from the consideration of the free electron collisions with atomic lattice structure. As can be expected, this damping force is proportional to the drifting velocity of the electron.

The electrons are thought to be accelerated until a final drifting velocity v_f is reached (see Figure 2.6(b)). At that time, the electron field force and the friction force are equal in

magnitude and the acceleration decreases to zero. If $dv/dt = 0$, then the equation of motion becomes

$$-e\vec{E} - \gamma\vec{v}_f = 0 \quad (2.13)$$

which yields

$$\gamma = -e\vec{E}/\vec{v}_f . \quad (2.14)$$

We insert the expression for γ into equation 2.12, to obtain:

$$m \frac{\partial \vec{v}(\vec{r}, t)}{\partial t} = -e\vec{E}(\vec{r}, t) + \frac{e\vec{E}}{\vec{v}_f} \vec{v}(\vec{r}, t) \quad (2.15)$$

The solution to this equation is

$$\vec{v} = \vec{v}_f [1 - \exp(-(-\frac{eE}{mv_f})t)] \quad (2.16)$$

We define the factor

$$\tau_c = -\frac{mv_f}{eE} \quad (2.17)$$

as a relaxation time or, more precisely, as the mean time between collisions.

Using the relation

$$J = -N_f v_f e = \sigma E , \quad (2.18)$$

we can rewrite the expression for the mean time between collisions as:

$$\tau_c = \frac{m\sigma}{N_f e^2}, \quad (2.19)$$

where, $m = 9.11 \times 10^{-31} \text{ Kg}$, is the mass of a free electron,
 $\sigma = 5.77 \times 10^7 \text{ S/m}$, is the conductivity for Aluminum,
 $N_f = 6.3 \times 10^{28} \text{ 1/m}^3$, is the free electron density, and
 $e = -1.602 \times 10^{-19} \text{ C}$, is the electric charge for an electron.

This gives a result of $\tau_c = 3.3 \times 10^{-14} \text{ s}$, which is roughly a factor of 10^5 times greater than the relaxation time computed based on considerations of electrical charge continuation. It is unreasonable to expect the charge relaxation time to be less than the mean time between collisions.

2.3.4 Fitting of free electron relaxation time and mean time between collision

So far, we have derived two characteristic times for an eddy current random process, relaxation time τ_R and mean time τ_c between collisions. In the following, we will investigate how the two characteristic times fit together to form a more complete picture describing the eddy current random process.

To do this, let us repeat the process similar to the derivation of the mean time between collisions. Consider a free electron. The equation of motion from Newton's second law, written in terms of τ_c for the damping term, is

$$\frac{\partial \bar{v}(\bar{r}, t)}{\partial t} = -\frac{e\bar{E}(\bar{r}, t)}{m} - \frac{\bar{v}(\bar{r}, t)}{\tau_c} \quad (2.20)$$

Multiplying both sides by eN_f gives an equation for the current density

$$\bar{J}(\bar{r}, t) = -eN_f \bar{v}(\bar{r}, t):$$

$$\frac{\partial \bar{J}(\bar{r}, t)}{\partial t} = \frac{e^2 N_f \bar{E}(\bar{r}, t)}{m} - \frac{\bar{J}(\bar{r}, t)}{\tau_c} \quad (2.21)$$

Taking the divergence on both sides of the equation and applying the continuity equation and Gauss's law, we have a differential equation for the electrical charge density:

$$\frac{\partial^2 \rho(\bar{r}, t)}{\partial t^2} + \frac{1}{\tau_c} \frac{\partial \rho}{\partial t} + \omega_p \rho = 0 \quad (2.22)$$

where, ω_p is defined as the *plasma frequency*, $\omega_p = \frac{N_f e^2}{m\epsilon}$. The solution for this equation is

$$\rho(\bar{r}, t) = \rho(\bar{r}, 0) e^{-st}, \quad (2.23)$$

where

$$\begin{aligned} s &= \frac{1}{2} \left(\frac{1}{\tau_c} \pm \sqrt{\left(\frac{1}{\tau_c} \right)^2 - 4\omega_p^2} \right) \\ &= \frac{1}{2\tau_c} \pm j \sqrt{\omega_p^2 - \left(\frac{1}{2\tau_c} \right)^2} \\ &= \frac{1}{2\tau_c} \pm j\nu. \end{aligned} \quad (2.24)$$

When $\omega_p \tau_c > 1/2$, the charge density settles down with a characteristic time of $2\tau_c$ and an oscillation frequency ν . If we use aluminum for example, $\omega_p \tau_c = 460 \gg 1/2$, $2\tau_c = 6.6 \times 10^{-14} \text{ s}$ and $\nu \approx \omega_p = 1.4 \times 10^{16}$.

When $\omega_p \tau_c < 1/2$, there is no charge density oscillation and there are two characteristic decay times $s^{-1} = 1 / \left(\frac{1}{2\tau_c} \pm \sqrt{\left(\frac{1}{2\tau_c}\right)^2 - \omega_p^2} \right)$. When $\omega_p \tau_c \ll 1/2$, the two decay times approach $s^{-1} = \tau_c, \epsilon/\sigma$. Note that the first time constant is simply the mean time between collisions and the second one is exactly the relaxation time τ_R , derived from electrical charge continuity considerations. The greater of the two relaxation times governs the overall charge density decay rate. Normally in most metals, $\tau_c \gg \epsilon/\sigma$, the mean time between collisions is much longer than the relaxation time τ_R . Therefore, the overall charge density relaxation time is governed by the mean time between collisions τ_c for the electrons.

2.4 Eddy Current as a Diffusion Process

There has been a vigorous debate concerning the nature of the eddy current process [6, 10, 11, 71]. One group of scholars had chosen to treat eddy currents as an electromagnetic wave phenomenon and process the signal using wave based approaches [4, 5, 7, 8, 9]. The other side of the debate treats eddy currents as a diffusion process [12]. The discussion presented in this section reinforces the statement that the eddy current process is a diffusion process and that the use of wave based approaches to process eddy current signals can lead to erroneous results.

In practical applications, the exciting current frequency used in eddy current NDE is less than a few megahertz. In this frequency range, the contribution from the wave term in the complete governing equation is negligible. The resulting eddy current governing equation is therefore given by:

$$\nabla \times \left(\frac{1}{\mu} \nabla \times \bar{A} \right) - \mu \nabla \left(\frac{1}{\mu} \nabla \bar{A} \right) = \bar{J}_0 - \sigma \frac{\partial \bar{A}}{\partial t} \quad (2.25)$$

If this equation is solved in one dimensional space and a time harmonic boundary condition is assumed, i.e., $\bar{A}(x=0, t) = \bar{A}(x=0)e^{j\omega t}$, then one obtains the following solution for \bar{A} over space and time:

$$\bar{A}(x, t) = \bar{A}_0 \exp\left(-\frac{1}{\delta} x\right) \cos\left(-\frac{1}{\delta} x + \omega t\right) \quad (2.26)$$

where $\delta = 2\sqrt{2 / \omega \mu \sigma}$ is defined as skin depth. At one skin depth, the eddy current signal attenuates exponentially to $1/e$ of its value at $x = 0$. Notice that there is a signal phase delay, which is proportional to x .

To illustrate the fact that the eddy current equation describes a diffusion process, we first compare the eddy current governing equation with a standard heat transfer governing equation. The heat transfer equation describes a diffusion process by its very nature.

$$u_{xx} - \frac{1}{a^2} u_t = q \quad (2.27)$$

The heat transfer from the surface of earth towards its core follows this heat transfer equation. If we assume that the temperature of the earth's surface is $u(x=0, t) = u_0 e^{j\omega t}$, then the temperature distribution underneath the earth surface is

$$u(x, t) = u_0 \exp(-\sqrt{\omega / 2a^2} x) \cos(-\sqrt{\omega / 2a^2} x + \omega t) \quad (2.28)$$

This expression has the same form as the eddy current solution in the one-dimensional case. As in eddy current NDE, the signal attenuates with the penetration depth. At the same time, the phase delay gets larger and larger. The sinusoidal form of the expression is totally incidental arising as a result of the form of the boundary condition. The sinusoidal form of the eddy current expression does not imply that the eddy current process is an electromagnetic wave phenomenon. It has the sinusoidal form because it follows the same form as the boundary condition after steady state has been reached. In general, eddy current signals take sinusoidal forms because of sinusoidal driving current sources.

If we compare the diffusion term with the wave term, when $\sigma \gg \omega \epsilon$; i.e., in the quasi-static case, the conducting current term dominates and the displacement current ($\partial D / \partial t$) can be neglected. Hence, the rotational magnetic field induced by the electric field no longer exists. Although the field is time varying, it is essentially "static" and does not propagate.

In eddy current applications, the exciting current is usually harmonic, and the physical quantities are time harmonic functions. The field distribution, therefore, depends only on the

position and phase delay at each point in space. Eddy current models can be used to determine the field distribution, for example, in conducting regions and in free space.

We note that, though eddy current and heat transfer problems follow the same form of the diffusion equation, there is a major difference that distinguishes the two processes. In heat transfer, when there is a spatial temperature distribution, it takes time for the molecular or atomic vibration to bring the temperature distribution into balance. In the case of eddy currents, the spatial variation of magnetic flux density does not necessarily cause the diffusion process. It is the time variation of the magnetic flux density that triggers the diffusion process. When there is a time variation in \vec{B} , it induces eddy currents locally. The eddy current resists changes in the magnetic field. At the same time, the eddy current causes energy dissipation resulting in magnetic field attenuation.

In heat transfer, the final steady state is in a temperature equilibrium state. When there is no heat source, the temperature distribution is uniform across space. When there are heat sources or sinks, the steady state temperature distribution, although static, is no longer uniform. Under this condition, heat diffusion still takes place. In contrast, in the case of eddy currents, in the final steady state, irrespective of the nature of distribution (uniform or nonuniform distribution), there is no longer any diffusion of energy. The field can possess any spatial distribution, and as long as it does not vary with time, then there is no diffusion associated with the process.

The issue will be discussed further in the next section by studying the Green's function corresponding to the process.

2.5 Green's Function for Eddy Current Diffusion Process

In a homogeneous medium the complete electromagnetic governing equation satisfies:

$$\nabla \times \nabla \times \bar{E} + \mu\sigma \frac{\partial \bar{E}}{\partial t} = -\mu \frac{\partial \bar{J}}{\partial t}, \quad (2.28)$$

or,

$$\nabla^2 \bar{A} - \mu\sigma \frac{\partial \bar{A}}{\partial t} - \mu\epsilon \frac{\partial^2 \bar{A}}{\partial t^2} = -\mu \bar{J}_0 \quad (2.29)$$

Neglecting the wave term, the governing equation for the magnetic vector potential is:

$$\nabla^2 \bar{A} - \mu\sigma \frac{\partial \bar{A}}{\partial t} = -\mu \bar{J}_0 \quad (2.30)$$

2.5.1 Eddy current process time asymmetry

Note that the eddy current governing equation is asymmetric with respect to time:

$$\nabla^2 \bar{A}(r, -t) + \mu\sigma \frac{\partial \bar{A}}{\partial(-t)} = -\mu \bar{J}_0(r, -t) \quad (2.31)$$

Thus the equation carries with it a directionality in time, i.e., it differentiates between past and future. The directionality in time of the diffusion equation is a consequence of the fact that the field represents the behavior of some average property of an ensemble of many

particles. Looking to the future, entropy which represents the order of the system increases; looking back to the past, the entropy is smaller.

2.5.2 Eddy current Green's function

As in the case of the scalar wave equation, it is possible to solve various inhomogeneous problems and initial value eddy current problems in terms of a Green's function that satisfies homogeneous boundary and causality conditions:

$$\begin{aligned}\nabla^2 \bar{G} - \mu\sigma \frac{\partial \bar{G}}{\partial t} &= -4\pi\delta(\bar{r} - \bar{r}_0)\delta(t - t_0) \\ \bar{G}(\bar{r}, t; \bar{r}_0, t_0) &= 0 \text{ if } t < t_0\end{aligned}\tag{2.32}$$

Once the Green's function is derived, the solution for a generic problem with inhomogeneous boundary conditions can be obtained.

$$\nabla^2 \bar{A} - \mu\sigma \frac{\partial \bar{A}}{\partial t} = -4\pi\bar{J}(\bar{r}_0, t_0)\tag{2.33}$$

The solution can be expressed in terms of the Green's function:

$$\begin{aligned}\bar{A}(\bar{r}, t) &= \int_0^t dt_0 \int dV_0 J(r_0, t_0) G(r, t; r_0, t_0) \\ &+ \frac{1}{4\pi} \int_0^t dt_0 \int dS_0 [G \nabla_0 A - A \nabla_0 G] \\ &+ \frac{\mu\sigma}{4\pi} \int dV_0 [AG]_{t_0=0}\end{aligned}\tag{2.34}$$

where the first term represents the contribution from the volume sources, the second term is derived from the boundary conditions and the last term is from the initial value of $A(r,t)$.

The Green's function in a homogeneous infinite domain can be written as [42]

$$G(R,\tau) = \frac{4\pi}{\mu\sigma} \left(\frac{\sqrt{\mu\sigma}}{2\sqrt{\pi\tau}} \right)^n \cdot e^{-(\mu\sigma R^2/4\tau)} u(\tau), \quad (2.35)$$

where, $R = |\bar{r} - \bar{r}_0|$,

$\tau = t - t_0$, and

n is the dimension of the problem.

For example, for a one-dimensional initial value problem,

$$\begin{aligned} A(r,t) &= \frac{\mu\sigma}{4\pi} \int dV_0 A(r_0,0) G(R,t) \\ A(x,t) &= \frac{\mu\sigma}{2\sqrt{\pi\alpha}} \int_{-\infty}^{\infty} e^{-(\mu\sigma(x-x_0)^2/4t)} A(x_0,0) dx_0 \end{aligned} \quad (2.36)$$

The one-dimensional Green's functions are plotted in Figure 2.7, for several different times t . We note that the curves have a sharp maximum at $R=0$, and the width of the curve increases with increasing time. At time $t=0$, the curve has zero width, since the source has just been applied and is concentrated at $r=0$. As t increases from zero, the value immediately rises everywhere, the most pronounced rise occurring near $R=0$.

This means that the eddy current Green's function indicates infinite diffusion velocity. In a finite time interval, the Green's function has a finite value (though not equally) everywhere over space, given the initial point source. We know that this is not the

real case. An eddy current diffusion process is just one of the many electromagnetic phenomena. The speed of energy propagation has to be bounded. We note that the eddy current diffusion equation is only a real world approximation, accounting for the averaging effect of the microscopic ensemble. In reality, due to inertia, there is a finite velocity of propagation. This can be explained by including the wave term in the eddy current diffusion equation.

$$\nabla^2 \bar{A} - \mu\sigma \frac{\partial \bar{A}}{\partial t} - \frac{1}{c^2} \frac{\partial^2 \bar{A}}{\partial t^2} = -4\pi \bar{J}(\bar{r}_0, t_0) \quad (2.37)$$

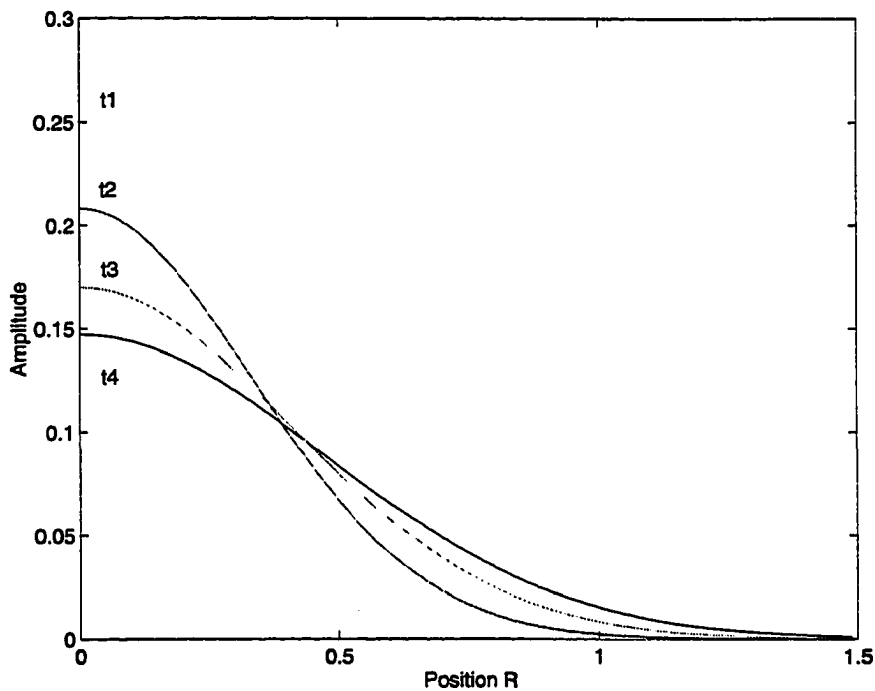


Figure 2.7. Green's function for diffusion for one dimension case, as a function of R for different times t . $t_1 < t_2 < t_3 < t_4$.

The Green's function of the complete equation contains all the information about eddy current phenomena. Let $\mu\sigma = a^2$, and concentrating only on the one dimensional case, the Green's function for this complete eddy current equation satisfies

$$\nabla^2 G - \mu\sigma \frac{\partial G}{\partial t} - \frac{1}{c^2} \frac{\partial^2 G}{\partial t^2} = -4\pi\delta(r - r_0)\delta(t - t_0) \quad (2.38)$$

The solution has a nice closed form expression [42]

$$G(R, \tau) = 2\pi c e^{-\frac{1}{2}a^2 c^2 \tau} J_0\left[\frac{a^2 c}{2} \sqrt{R^2 - c^2 \tau^2}\right] u(c\tau - |R|) \quad (2.39)$$

Now, by adding the wave propagation term (inertia term), the diffusion speed becomes finite. The speed of the diffusion energy propagation is strictly bounded by the speed of wave propagation, c . The diffusion equation without the inertia term represents a long term averaging effect. That is, when $c \rightarrow \infty$ and $c\tau \gg R$, the Green's function for the complete equation would approach that for the simplified diffusion equation. In order to obtain a better perspective, the Green's functions for different c 's are shown in Figure 2.8. The time instant at which the curves are plotted is the same as the one corresponding to t_1 in Figure 2.7. We see that when the wave term is relatively large (c is small), the effect on the energy propagation speed and its bounding effect is apparent. As the speed c becomes larger, the energy propagation speed limit is still applicable. However, now the space covered by the allowable velocity is much larger. The effect of the variation in velocity does not show up in the limited spatial range under consideration, and the value approaches the value

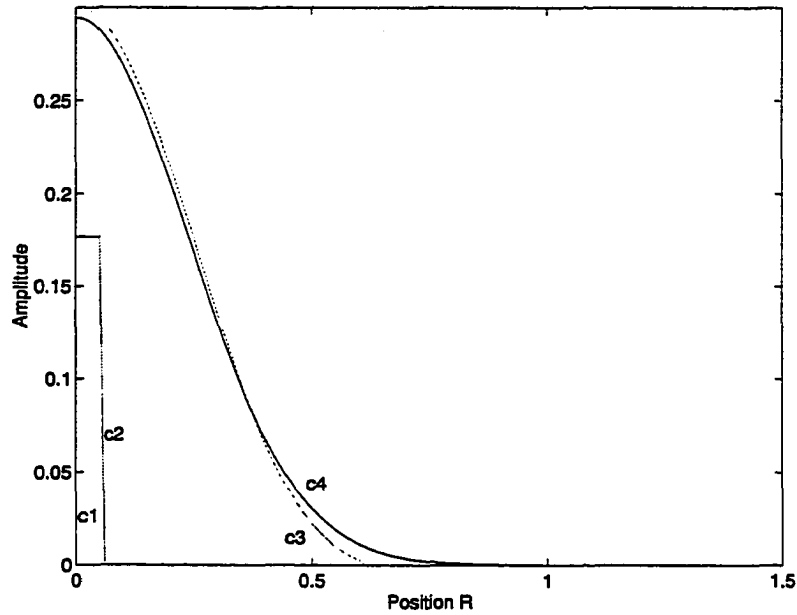


Figure 2.8. The Green's functions including the wave term, plotted for different c 's. $c_1 < c_2 < c_3 < c_4$. The time instant is the same as t_1 in Figure 2.7.

obtained from the diffusion equation. Therefore, the diffusion equation is a limiting case in which the contribution from the wave term is averaged out over time.

This approximation of the eddy current diffusion Green's function to the complete Green's function can also be shown analytically by taking the following limiting values for the complete Green's function:

$$u(c\tau - |R|) \xrightarrow{c \rightarrow \infty} u(c\tau) = u(\tau) \quad (2.40)$$

$$\begin{aligned}
J_0\left[\frac{a^2c}{2}\sqrt{R^2-c^2\tau^2}\right] &\xrightarrow{c\rightarrow\infty} \sqrt{\frac{2}{\pi\left(\frac{a^2c}{2}\sqrt{R^2-c^2\tau^2}\right)}} \cos\left(\frac{a^2c}{2}\sqrt{R^2-c^2\tau^2} - \frac{\pi}{4}\right) \\
&\xrightarrow{c\gg R} \sqrt{\frac{2}{\pi\left(\frac{a^2c}{2}\cdot jc\tau\right)}} \cos\left(\frac{a^2c}{2}\cdot j\sqrt{c^2\tau^2-R^2} - \frac{\pi}{4}\right)
\end{aligned} \tag{2.41}$$

Then,

$$\begin{aligned}
G(R,\tau) &= 2\pi ce^{-\frac{1}{2}a^2c^2\tau} J_0\left[\frac{a^2c}{2}\sqrt{R^2-c^2\tau^2}\right] u(c\tau - |R|) \\
&\rightarrow 2\pi ce^{-\frac{1}{2}a^2c^2\tau} \sqrt{\frac{2}{\pi\left(\frac{a^2c}{2}\cdot jc\tau\right)}} \cos\left(\frac{a^2c}{2}\cdot j\sqrt{c^2\tau^2-R^2} - \frac{\pi}{4}\right) u(\tau) \\
&= 2\pi ce^{-\frac{1}{2}a^2c^2\tau} \frac{2}{ac} \frac{1}{\sqrt{\pi\tau}} e^{-j\frac{\pi}{4}} \frac{1}{2} \left[e^{-\frac{a^2c}{2}\sqrt{c^2\tau^2-R^2}-j\frac{\pi}{4}} + e^{\frac{a^2c}{2}\sqrt{c^2\tau^2-R^2}+j\frac{\pi}{4}} \right] u(\tau) \\
&\rightarrow \frac{2\pi}{a} \frac{1}{\sqrt{\pi\tau}} e^{-\frac{1}{2}a^2c^2\tau} e^{-j\frac{\pi}{4}} e^{\frac{a^2c}{2}\sqrt{c^2\tau^2-R^2}} e^{j\frac{\pi}{4}} u(\tau) \\
&= \frac{2\pi}{a} \frac{1}{\sqrt{\pi\tau}} e^{-\frac{1}{2}a^2c^2\tau} e^{\frac{a^2c^2\tau}{2}\sqrt{1-R^2/c^2\tau^2}} u(\tau) \\
&\rightarrow \frac{2\pi}{a} \frac{1}{\sqrt{\pi\tau}} e^{-\frac{1}{2}a^2c^2\tau} e^{\frac{a^2c^2\tau}{2}(1-R^2/2c^2\tau^2)} u(\tau) \\
&= \frac{2\pi}{a} \frac{1}{\sqrt{\pi\tau}} e^{-a^2R^2/4\tau} u(\tau)
\end{aligned} \tag{2.42}$$

The limiting result is exactly the same as the Green's function for eddy current diffusion.

2.6 Eddy Current Modeling of Flaw Signals

2.6.1 Eddy current flaw kernel

The eddy current method is used very widely in nondestructive evaluation. In most applications, it is used for flaw characterization inside or on the surface of a conducting material. In a standard setup, an exciting coil is placed above a sample. The coil is scanned across the surface of the test specimen to detect the presence of any flaws. In the case of a point flaw, the coil picks up the flaw signal over a range larger than the coil size [12]. In other words, even for a tiny flaw, the support of the flaw signature is at least equal to the coil diameter. A point size flaw image therefore has a large footprint. If the flaw is single and small, we can determine its location by making use of spatial symmetry in the output signal. However, if the flaw is large and of irregular shape, or if there exist multiple flaws, the smearing effect would make the task of characterizing the flaw(s) very difficult.

The flaw smearing kernels associated with voltage induced in the pickup coil and the magnetic field are derived based on a current dipole model [13]. This is useful since a knowledge of the eddy current smearing kernel allows reconstruction of the flaw by deconvolving the measured eddy current image. In this way, the number, locations, and sizes of flaws can be estimated from the reconstructed image.

2.6.2 Derivation of eddy current flaw kernels with the current dipole model

2.6.2.1 Overview In deriving the eddy current kernels using the current dipole model, a few assumptions need to be made. First, it is assumed that the flaw is spherical in

shape with radius a . Second, the flaw size is small (much smaller than the eddy current skin depth), so that if the flaw does not exist, the eddy current flowing over the flaw region would be uniform. The sample has electrical conductivity σ while the flaw has conductivity σ_f . The existence of the flaw disturbs the flow of the eddy current both within and the area surrounding it.

The change in eddy current distribution around the flaw changes the magnetic field intensity distribution. Hence, the change can be measured using a Hall probe or a pickup coil.

By applying the boundary conditions on the surface of the flaw for the eddy current and electrical field density, one can calculate the change in eddy current spatial distribution due to the flaw. Interestingly the effect of the flaw on its surrounding area is equivalent to the effect of a current dipole [13] as we see in the derivation below.

By using the current dipole model, one can regard the current dipole and pickup coil as the primary and secondary coil, respectively, as in a transformer. A change in the exciting coil current introduces a change in dipole current. Also, the change in dipole current changes the induced voltage in the pickup coil. By applying the reciprocity theorem as in transformer theory, one can derive the formula for the change in induced voltage. In the following section, the pickup coil voltage flaw kernel is first derived. The corresponding magnetic field distribution is then derived.

2.6.2.2 Current dipole model The existence of the tiny flaw affects its local eddy current distribution. The uniform excitation local eddy current is directed along the z axis of a spherical polar coordinate system, whose origin coincides with the flaw.

The study can be initiated with a description of the flaw boundary conditions [13]:

$$\begin{cases} (\bar{J}_s + \bar{J}_i - \bar{J}_f) \bullet \bar{n}|_{r=a} = 0 \\ (\bar{E}_s + \bar{E}_i - \bar{E}_f) \times \bar{n}|_{r=a} = 0 \end{cases} \quad (2.43)$$

Here, \bar{n} is the surface normal vector, and the sub-indices s , i and f refer to the scattered field, the incident field and the field within the flaw, respectively.

The equation for the electrical scalar potential to be satisfied is $\nabla^2 \Phi = 0$, with $\bar{E} = -\nabla \Phi$. Therefore the boundary conditions for Φ are:

$$\begin{cases} (\sigma(\nabla \Phi_s + \nabla \Phi_i) - \sigma_f \nabla \Phi_f) \bullet \bar{n}|_{r=a} = 0 \\ (\Phi_s + \Phi_i - \Phi_f)|_{r=a} = 0 \end{cases} \quad (2.44)$$

Writing the potentials in terms of Legendre polynomials and using

$$\Phi_i = -E_i r \cos \theta, \quad (2.45)$$

one obtains:

$$\begin{cases} \Phi_s = -\frac{\sigma - \sigma_f}{2\sigma + \sigma_f} a^3 E_i \frac{1}{r^2} \cos \theta \\ \Phi_f = -\frac{3\sigma}{2\sigma + \sigma_f} E_i r \cos \theta \end{cases} \quad (2.46)$$

The scattered potential corresponds to an eddy current distribution given by

$$\bar{J}_s = \frac{\bar{E}_s}{\sigma} = -J_i \frac{\sigma - \sigma_f}{2\sigma + \sigma_f} \frac{a^3}{r^3} (\bar{r} 2 \cos \theta + \bar{\theta} \sin \theta) \quad (2.47)$$

When this is compared with the field of a current dipole $P_j \bar{z}$ at the origin [85], given by

$$\bar{J} = \frac{P_j}{4\pi r^3} (\bar{r} 2 \cos \theta + \bar{\theta} \sin \theta) \quad (2.48)$$

it is clear that the effect of current scattering by a spherical flaw may be replaced by the current dipole [13]:

$$\bar{P}_j = -4\pi a^3 \frac{\sigma - \sigma_f}{2\sigma + \sigma_f} \bar{J}_i \quad (2.49)$$

The induced voltage in the pickup coil can then be derived using the current dipole model.

2.6.2.3 Induced voltage in pickup coil by a current dipole To account for the induced voltage in the pickup coil by the current dipole, the dipole can be regarded as the limiting state of a spherical region of uniform current. The equivalent current, \bar{J}_1' , is the difference between the actual current in the flaw and the current in the flaw region, if no flaws exist. When the flaw is nonconducting,

$$\begin{aligned}\bar{J}_1' &= \bar{J}_f - \bar{J}_i \\ &= -\bar{J}_i\end{aligned}\tag{2.50}$$

The electrical field due to the flaw equivalent current (current I_1 in the excitation coil) is denoted by \bar{E}_1 . Similarly the electrical field in the small sphere due to an imaginary current I_2 flowing in the pickup coil is denoted by \bar{E}_f . Using the reciprocity theorem:

$$I_2 \int_C \bar{E}_1 d\bar{l}_2 = \int_V \bar{E}_f \bar{J}_1' dV\tag{2.51}$$

Note that, $\int_C \bar{E}_1 d\bar{l}_2$ is the induced voltage in the pickup coil,

$$\bar{E}_f = \frac{3\sigma}{2\sigma + \sigma_f} \bar{E}_2 = \frac{3}{2} \bar{E}_2,\tag{2.52}$$

$$\bar{J}_1' = -\bar{J}_i = -\sigma \bar{E}_1\tag{2.53}$$

Therefore,

$$V = -\frac{3}{2} \sigma (\text{Vol}) \frac{\bar{E}_1 \bar{E}_2}{I_1 I_2} I_1,\tag{2.54}$$

where,

I_1 is the exciting current in the exciting coil,

I_2 is the imaginary exciting current in the pickup coil,

\vec{E}_1 is the \vec{E} field produced at the flaw location by the exciting current,
 \vec{E}_2 is produced at the flaw location by the imaginary pickup coil current,
 and Vol is the volume of the flaw.

Apply the relationship between \vec{E} and \vec{A} ,

$$\vec{E} = -\frac{\partial \vec{A}}{\partial t} = -j\omega \vec{A}, \quad (2.55)$$

one obtains the expression for the voltage change due to the flaw in terms of \vec{A} :

$$V = \frac{3}{2}(Vol)\sigma\omega^2 \frac{\vec{A}_1}{I_1} \frac{\vec{A}_2}{I_2} I_1 \quad (2.56)$$

The impedance change is then:

$$\nabla Z = V / I_1 \quad (2.57)$$

Once the eddy current induced voltage flaw signal is derived for single frequency excitation, the voltage change for any arbitrary form of excitation signal can be calculated in terms of its Fourier components. Suppose that the excitation signal has frequency component $F(\omega)$ at ω , then the overall voltage change is:

$$V = \frac{1}{2\pi} \int_{-\infty}^{\infty} F(\omega) V(\omega) e^{j\omega t} d\omega \quad (2.58)$$

Since voltage is a real physical quantity, it can also be written in another form:

$$V = \frac{1}{\pi} \int_0^{\infty} \text{Re}[F(\omega)V(\omega)e^{j\omega t}]d\omega \quad (2.59)$$

2.6.2.4 Magnetic flux density change due to a tiny flaw by a current dipole

Using the same current dipole model, we further derive the change in the magnetic flux density due to a tiny flaw. The derived result will be applicable only for the magnetic flux density component that is normal to the pickup coil orientation. This magnetic field can be measured using a Hall probe, for example.

When the eddy current excitation is sinusoidal, the change in induced voltage can be related to the magnetic field generated by a tiny flaw.

$$V(\omega) = -\frac{\partial\Phi}{\partial t} = -\oint \frac{\partial B}{\partial t} dS \quad (2.60)$$

When the size of the pickup coil approaches zero, the magnetic field circled by the coil is uniform. Denoting the size of the tiny pickup coil as ΔS ,

$$\begin{aligned} V(\omega) &= -\frac{\partial B}{\partial t} \Delta S = -j\omega B(\omega)\Delta S \\ &= \frac{3}{2}(Vol)\sigma\omega^2 \frac{\bar{A}_1}{I_1} \frac{\bar{A}_2}{I_2} I_1 \end{aligned} \quad (2.61)$$

and

$$B(\omega) = j \frac{3}{2\Delta S} (Vol)\sigma\omega^2 \frac{\bar{A}_1}{I_1} \frac{\bar{A}_2}{I_2} I_1 \quad (2.62)$$

The magnetic flaw signal obtained with sinusoidal excitation is now derived. In the case of non-sinusoidal excitation, the flaw kernel is a function of time. The time varying magnetic field can be derived using the procedure employed for deriving the induced voltage. Again, note that the magnetic field is a real physical quantity. Therefore,

$$\begin{aligned}
 B &= \frac{1}{\pi} \int_0^{\infty} \text{Re}[F(\omega)B(\omega)e^{j\omega t}] d\omega \\
 &= -\frac{3}{2\pi\Delta S} (\text{Vol}) \int_0^{\infty} \text{Im}[F(\omega)\sigma\omega \frac{\bar{A}_1}{I_1} \frac{\bar{A}_2}{I_2} I_1 e^{j\omega t}] d\omega
 \end{aligned} \tag{2.63}$$

The size of the pickup coil ΔS appears in the denominator in the expression. The magnetic field change is independent of the pickup coil since the \bar{A}_2 term in the formula cancels the term ΔS .

2.7 Analytical Modeling of the Electromagnetic Field

In Section 2.6, we derived the expression for the induced voltage in the pickup coil and the magnetic field due to a flaw. The closed form results are expressed in terms of magnetic vector potentials inside the test specimen. Therefore, in this section, we will develop analytical models for calculating the magnetic vector potential distributions.

All the problems are assumed to have two-dimensional axisymmetric geometries where the magnetic vector potential \bar{A} has only a θ component, simply written as A .

2.7.1 Post processing

Once the magnetic vector potential \bar{A} distribution is known, flux signals as well as other variables of interest can be calculated.

Electrical field \bar{E}

$$\bar{E} = -\nabla\Phi - \frac{\partial\bar{A}}{\partial t} \quad (2.64)$$

where Φ is the electrical scalar potential. Since there are free electrical charges, $\Phi = 0$ in two-dimensional and axisymmetric cases. Hence if we assume sinusoidal excitation, i.e.,

$\bar{A} = Ae^{j\omega t}\hat{\theta}$, then

$$\bar{E} = -j\omega A\hat{\theta} \quad (2.65)$$

The electrical field has only θ component and consequently the induced eddy current inside the conducting specimen is:

$$\bar{J} = \sigma\bar{E} = -j\sigma\omega A\hat{\theta} \quad (2.66)$$

Magnetic field \bar{B}

$$\begin{aligned} \bar{B} &= \nabla \times \bar{A} \\ &= -\frac{\partial A}{\partial z}\hat{r} + \frac{1}{r}\frac{\partial}{\partial r}(rA)\hat{z} \end{aligned} \quad (2.67)$$

Electrical and magnetic fields are two fundamental electromagnetic field quantities.

The rest of the physical quantities can be written in terms of the \vec{E} and \vec{B} fields. For

example:

Electrical energy density

$$W_E = \frac{1}{2} \vec{E} \cdot \vec{D} = \frac{1}{2} \epsilon E^2 \quad (2.68)$$

Magnetic energy density

$$W_B = \frac{1}{2} \vec{H} \cdot \vec{B} = \frac{1}{2\mu} B^2 \quad (2.69)$$

Electromagnetic energy flow

$$\begin{aligned} \vec{S} &= \vec{E} \times \vec{H} \\ &= \frac{j\omega}{\mu} A \left[-\frac{\partial A}{\partial z} \hat{z} - \frac{1}{r} \frac{\partial}{\partial r} (rA) \hat{r} \right] \end{aligned} \quad (2.70)$$

2.7.2 Application to a conducting half plane

In this section, the eddy current field generated by a coil over a conducting half plane is analyzed. The test configuration is shown in Figure 2.1. The model is used to draw some basic conclusions that a simple model like this can provide.

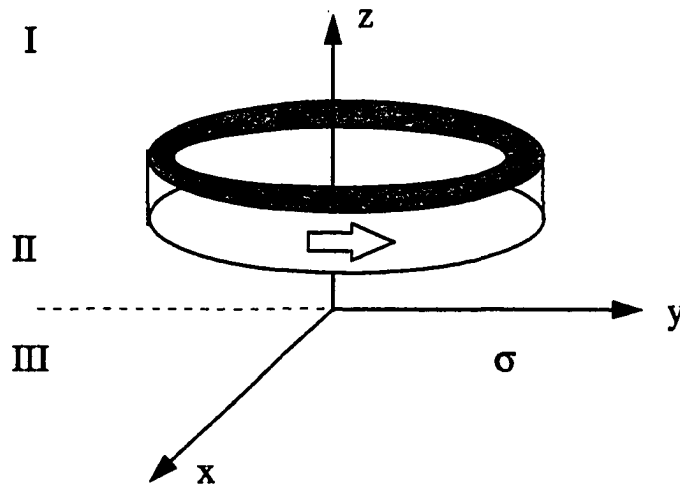


Figure 2.9. Coordinate of eddy current setup with a conducting half plane

A cylindrical coordinate system is adopted to exploit the symmetry in the geometry. The coil is circular with a rectangular cross section. The cross section ranges from l_1 to l_2 in the z direction and from r_1 to r_2 in the r direction. The conducting half space is copper and has a conductivity of $\sigma = 5.77 \times 10^7$ Siemens/meter. Because of the cylindrical symmetry, the θ component A_θ denoted as A has to be considered. The space is divided into three regions as shown in Figure 2.9.

To solve the problem with a finite size coil, we first solve the same problem with a “Dirac delta function coil”. The result is then integrated over the finite coil cross section to obtain the solution. For a Dirac delta function coil located at $(r, z) = (r_0, l)$, the governing equation expressed in a cylindrical coordinate system is:

$$\frac{\partial^2 A}{\partial r^2} + \frac{1}{r} \frac{\partial A}{\partial r} + \frac{\partial^2 A}{\partial z^2} - \frac{A}{r^2} - j\omega\mu\sigma A + \mu I \delta(r - r_0) \delta(z - l) = 0 \quad (2.71)$$

In regions I and II:

$$\frac{\partial^2 A}{\partial r^2} + \frac{1}{r} \frac{\partial A}{\partial r} + \frac{\partial^2 A}{\partial z^2} - \frac{A}{r^2} = 0 \quad (2.72)$$

In region III:

$$\frac{\partial^2 A}{\partial r^2} + \frac{1}{r} \frac{\partial A}{\partial r} + \frac{\partial^2 A}{\partial z^2} - \frac{A}{r^2} - j\omega\mu\sigma A = 0 \quad (2.73)$$

If the magnetic vector potential fields for regions I, II and III are denoted as $A^{(1)}(r, z)$, $A^{(2)}(r, z)$ and $A^{(3)}(r, z)$, respectively, then the boundary conditions are:

$$\begin{cases} A^{(1)}(r, l) = A^{(2)}(r, l) \\ \frac{\partial}{\partial z} A^{(1)}|_{z=l} = \frac{\partial}{\partial z} A^{(2)}|_{z=l} - \mu I \delta(r - r_0) \end{cases} \quad (2.74)$$

$$\begin{cases} A^{(2)}(r, 0) = A^{(3)}(r, 0) \\ \frac{\partial}{\partial z} A^{(2)}|_{z=0} = \frac{\partial}{\partial z} A^{(3)}|_{z=0} \end{cases} \quad (2.75)$$

Solving the equations for regions I, II and III, and applying the appropriate boundary conditions, we obtain the following solutions for regions I, II and III, respectively:

$$\begin{aligned}
A^{(1)} &= \frac{1}{2} \mu I r_0 \int_0^{\infty} J_1(\alpha r_0) J_1(\alpha r) \times \left[e^{-\alpha(z-l)} + \frac{\alpha - \alpha_1}{\alpha + \alpha_1} e^{-\alpha(z+l)} \right] d\alpha \\
A^{(2)} &= \frac{1}{2} \mu I r_0 \int_0^{\infty} J_1(\alpha r_0) J_1(\alpha r) \times \left[e^{\alpha(z-l)} + \frac{\alpha - \alpha_1}{\alpha + \alpha_1} e^{-\alpha(z+l)} \right] d\alpha \\
A^{(3)} &= \mu I r_0 \int_0^{\infty} J_1(\alpha r_0) J_1(\alpha r) \times \left[\frac{\alpha}{\alpha + \alpha_1} e^{\alpha_1 z} e^{-\alpha l} \right] d\alpha
\end{aligned} \tag{2.76}$$

where $\alpha_1 = \sqrt{\alpha^2 + j\omega\mu\alpha}$,

$J_1(x)$ is the first order Bessel function.

Since we have the results for a delta function coil, the magnetic vector potential for a finite cross section coil can now be derived by integrating:

$$\bar{A}(r, z) = \int_{r_1}^{r_2} dr_0 \int_{l_1}^{l_2} \bar{A}(r, z, r_0, l) dl \tag{2.77}$$

The results for regions I, the region between I and II, II and III are denoted as

$A^{(1)}(r, z)$, $A^{(12)}(r, z)$, $A^{(2)}(r, z)$ and $A^{(3)}(r, z)$, respectively and can be derived.

$$\begin{aligned}
A^{(1)} &= \frac{1}{2} \mu I \int_{r_1}^{r_2} r_0 \int_0^{\infty} \frac{1}{\alpha} J_1(\alpha r_0) J_1(\alpha r) \times e^{-\alpha z} \left[(e^{\alpha l_2} - e^{\alpha l_1}) + \frac{\alpha - \alpha_1}{\alpha + \alpha_1} (e^{-\alpha l_2} - e^{-\alpha l_1}) \right] d\alpha dr_0 \\
A^{(12)} &= \frac{1}{2} \mu I \int_{r_1}^{r_2} r_0 \int_0^{\infty} \frac{1}{\alpha} J_1(\alpha r_0) J_1(\alpha r) \times \left[(2 - e^{-\alpha(z-l_1)} - e^{\alpha(z-l_2)}) + \frac{\alpha - \alpha_1}{\alpha + \alpha_1} (e^{-\alpha(z+l_1)} - e^{-\alpha(z+l_2)}) \right] d\alpha dr_0 \\
A^{(2)} &= \frac{1}{2} \mu I \int_{r_1}^{r_2} r_0 \int_0^{\infty} \frac{1}{\alpha} J_1(\alpha r_0) J_1(\alpha r) \times (e^{-\alpha l_1} - e^{-\alpha l_2}) \left[e^{\alpha z} + \frac{\alpha - \alpha_1}{\alpha + \alpha_1} e^{-\alpha z} \right] d\alpha dr_0 \\
A^{(3)} &= \mu I \int_{r_1}^{r_2} r_0 \int_0^{\infty} J_1(\alpha r_0) J_1(\alpha r) \times (e^{-\alpha l_1} - e^{-\alpha l_2}) \left[\frac{1}{\alpha + \alpha_1} e^{\alpha_1 z} \right] d\alpha dr_0
\end{aligned} \tag{2.78}$$

The values of A were computed using the above expressions for a coil geometry with $(r_1, r_2) = (0.5, 1.5 \text{ mm})$ and $(l_1, l_2) = (0.0, 1.0 \text{ mm})$. Figure 2.10 shows the corresponding variation in A in the z direction. The dotted line represents the result obtained using the classical skin depth formula. One can observe that the actual magnetic field attenuates at a rate that is much faster than an exponential decay [45, 46, 47, 48]. The rate of decay is identical only in the one-dimensional case. This gives a realistic assessment of the ability of the eddy current method with regard to its ability to “penetrate” the test object in a standard eddy current setup. It should also be mentioned that, when the liftoff increases, the penetration profile approximates the exponential form more closely.

Figure 2.11 shows the variation in A in the r direction. It indicates that the magnetic vector potential is the strongest at the point directly below the exciting coil. The first plot shows the variation of the real part of A as a function of r . The second plot shows the imaginary part while the last figure depicts the amplitude of the magnetic vector potential.

The corresponding eddy current imaging kernels are plotted in Figure 2.12. The kernels represent the voltage induced in the coil due to the flaw. The results were normalized by the volume of the flaw. The horizontal axis indicates flaw location while the vertical axis represents the corresponding change in the induced voltage due to the flaw. The three plots, from top to bottom, show the real part, imaginary part and the amplitude of the change in the output voltage signal, respectively. The figure indicates that the flaw signal is the strongest when the flaw is directly below the coil and the flaw image is smeared out to a size that is larger than the excitation coil. Note that there is a dead zone at the center, showing that the

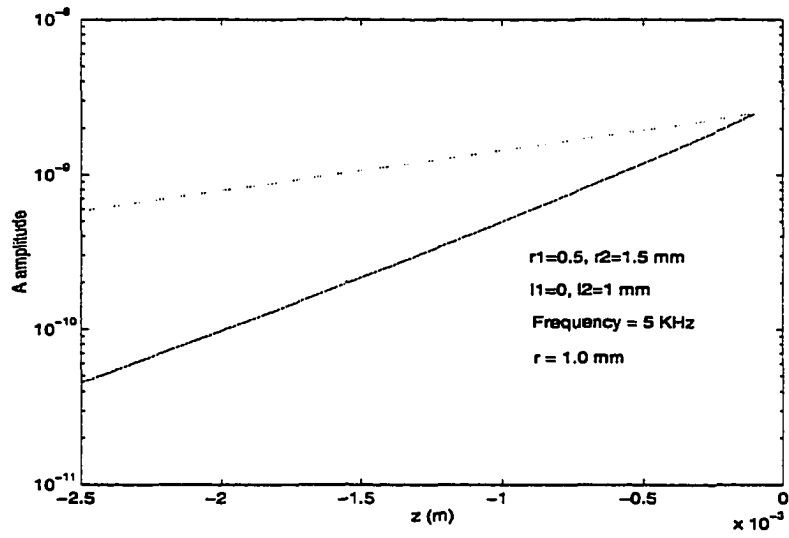


Figure 2.10. Magnetic vector potential variation in the z direction for a finite cross-section coil

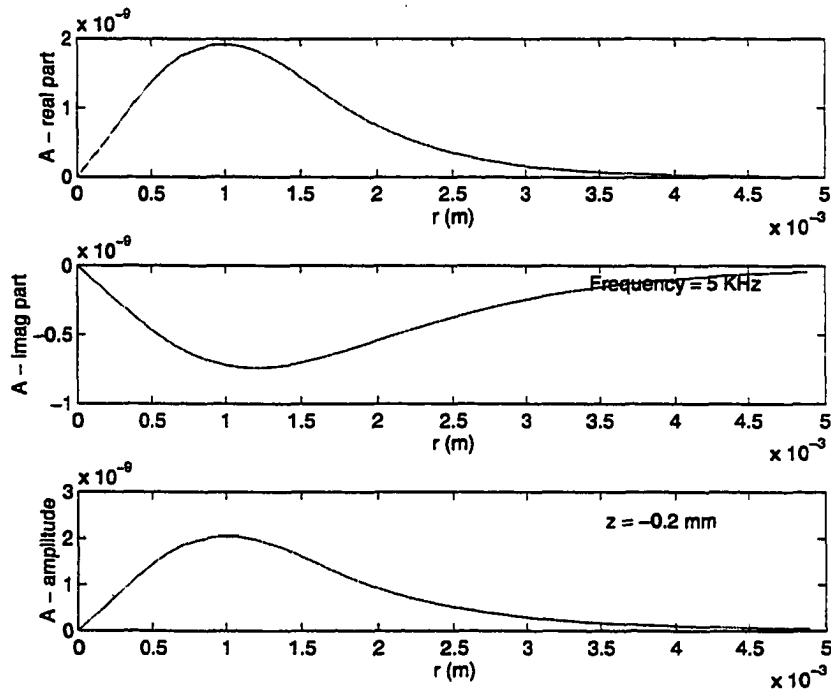


Figure 2.11. Magnetic vector potential variation in the r direction

signal generated is zero when the coil sits exactly above a flaw.

The corresponding magnetic vector potential distribution over space is shown in Figures 2.13 and 2.14. Figure 2.13 shows the equi-A potential contours over the region where $z = 0$ represents the interface between the air and the conducting half plane. Figure 2.14 shows the corresponding equi-phase contours.

As mentioned in the section for post signal processing, other physical quantities can

be obtained once the magnetic vector potential A is calculated. As an illustration, constant magnetic flux density lines over space are plotted in Figure 2.15. This is simply the constant contours of rA . Since the problem is axisymmetric, the magnetic flux is directly proportional to rA :

$$\Phi = \oint \vec{A} \cdot d\vec{l} = 2\pi rA \quad (2.79)$$

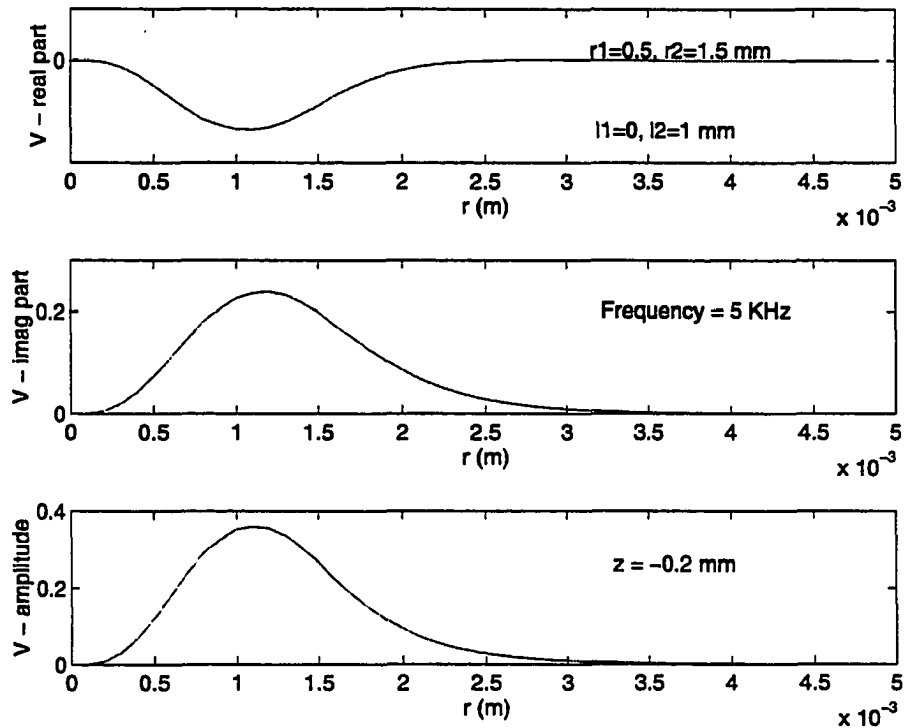


Figure 2.12. Induced voltage change by a tiny flaw as a function of the radial distance r from the center

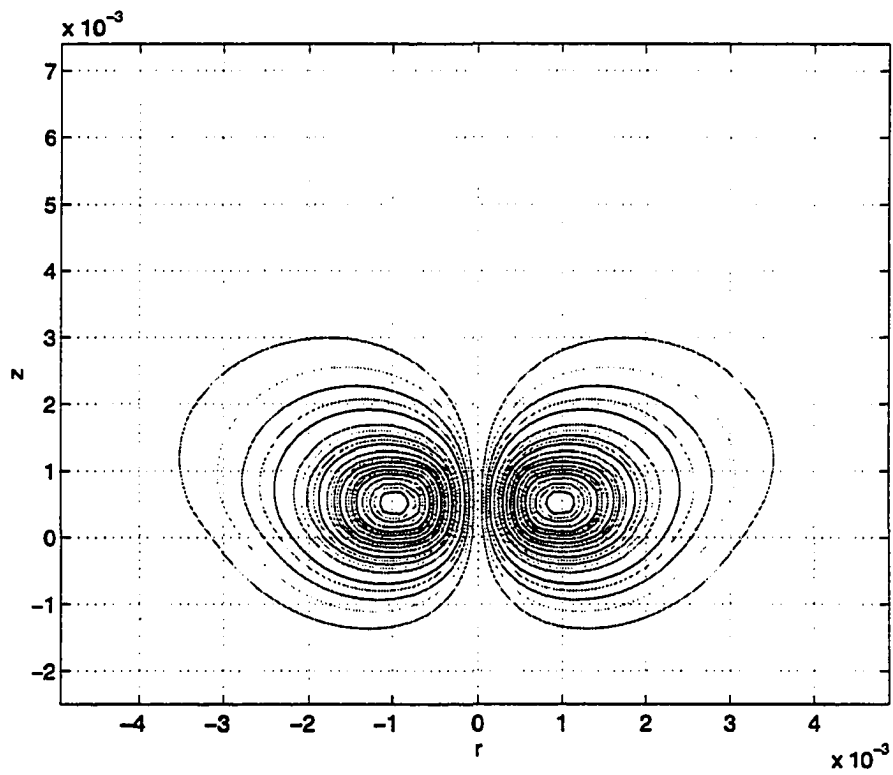


Figure 2.13. Contour of magnetic vector potential distribution, amplitude

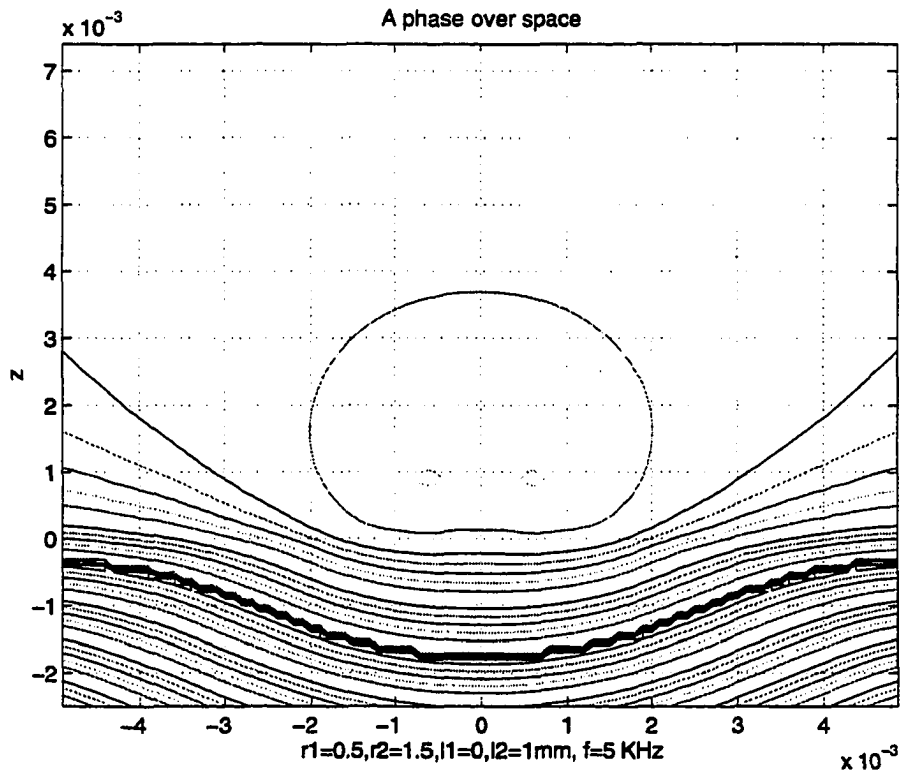


Figure 2.14. Contour of magnetic vector potential distribution,
phase

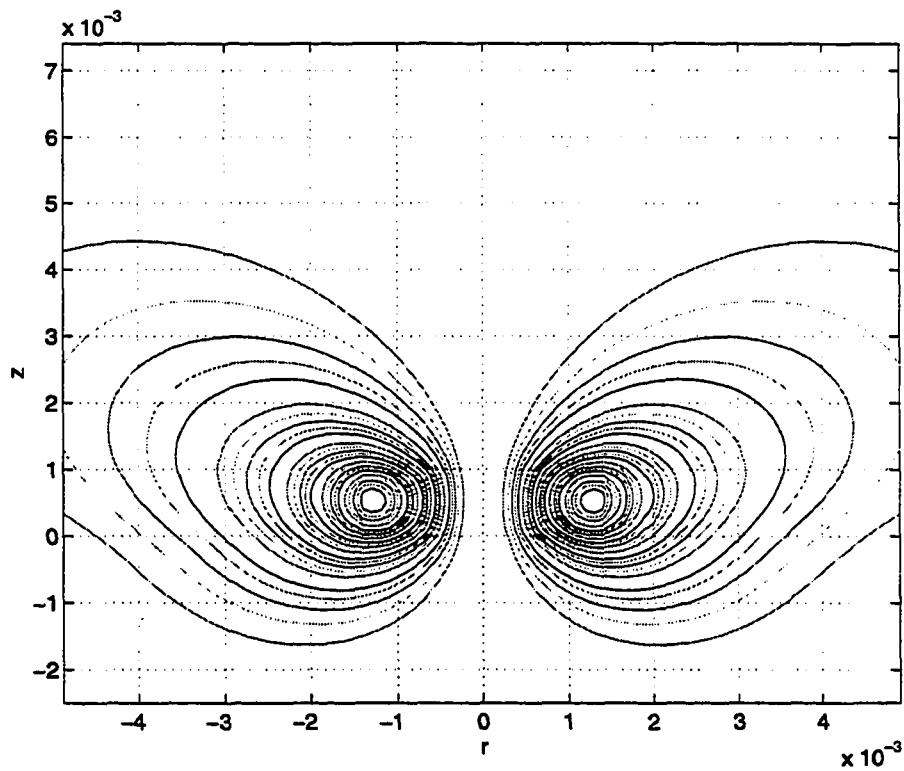


Figure 2.15. Constant magnetic flux density lines over space

Therefore, constant magnetic flux lines align themselves along the contours of rA .

2.7.3 Application to a conducting slab

In the last section, the eddy current model was used to simulate a conducting half plane geometry where only the diffusion term is considered and the wave term in the complete governing equation is neglected.

In this section, the full eddy current model which includes the wave term is used to

simulate a conducting slab of thickness m . The objective is to control selectively both the diffusion and wave terms and compare their contribution. A circular coil with rectangular cross section is placed above the conducting copper slab. The setup, shown in Figure 2.16, consists of five regions: region I above the coil, region between I and II where the coil is located, region II below the coil and above the slab, region III for the conducting slab, and region IV below the conducting slab. The magnetic vector potential for the five regions are denoted as $A^{(1)}(r,z)$, $A^{(12)}(r,z)$, $A^{(2)}(r,z)$, $A^{(3)}(r,z)$ and $A^{(4)}(r,z)$, respectively.

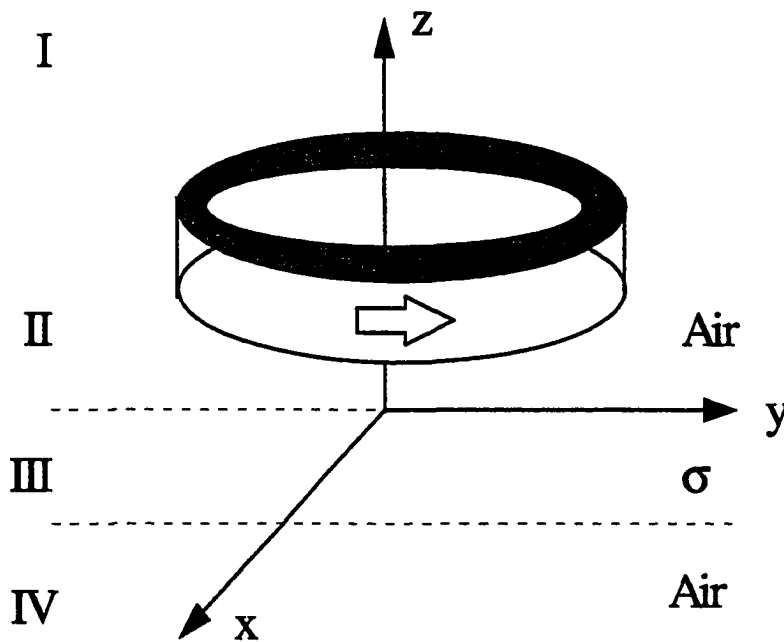


Figure 2.16. Model configuration with a conducting slab

Again, we start with a “delta function” coil located at $(r, z) = (r_0, l)$ and then obtain the result for a finite cross section coil by integrating the result appropriately. The full governing equation is:

$$\frac{\partial^2 A}{\partial r^2} + \frac{1}{r} \frac{\partial A}{\partial r} + \frac{\partial^2 A}{\partial z^2} - \frac{A}{r^2} + (\omega^2 \mu \epsilon - j \omega \mu \sigma) A + \mu I \delta(r - r_0) \delta(z - l) = 0 \quad (2.80)$$

Equation (2.79) can be simplified depending on the region.

In regions I, II and IV:

$$\frac{\partial^2 A}{\partial r^2} + \frac{1}{r} \frac{\partial A}{\partial r} + \frac{\partial^2 A}{\partial z^2} - \frac{A}{r^2} + (\omega^2 \mu \epsilon) A = 0 \quad (2.81)$$

In region III:

$$\frac{\partial^2 A}{\partial r^2} + \frac{1}{r} \frac{\partial A}{\partial r} + \frac{\partial^2 A}{\partial z^2} - \frac{A}{r^2} + (\omega^2 \mu \epsilon - j \omega \mu \sigma) A = 0 \quad (2.82)$$

The boundary conditions for the magnetic vector potentials are:

$$\begin{cases} A^{(1)}(r, l) = A^{(2)}(r, l) \\ \frac{\partial}{\partial z} A^{(1)}|_{z=l} = \frac{\partial}{\partial z} A^{(2)}|_{z=l} - \mu I \delta(r - r_0) \end{cases} \quad (2.83)$$

$$\begin{cases} A^{(2)}(r, 0) = A^{(3)}(r, 0) \\ \frac{\partial}{\partial z} A^{(2)}|_{z=0} = \frac{\partial}{\partial z} A^{(3)}|_{z=0} \end{cases} \quad (2.84)$$

$$\begin{cases} A^{(3)}(r, m) = A^{(4)}(r, m) \\ \frac{\partial}{\partial z} A^{(3)}|_{z=m} = \frac{\partial}{\partial z} A^{(4)}|_{z=m} \end{cases} \quad (2.85)$$

The solutions for the magnetic vector potentials are given by:

$$\begin{aligned} A^{(1)}(r, z, r_0, l) = & \frac{1}{2} \mu I r_0 \int_0^\infty J_1(\alpha r_0) J_1(\alpha r) [e^{\alpha_1 l - \alpha_1 z} \\ & + \frac{(\alpha_1^2 - \alpha_3^2)(e^{-\alpha_3 m} - e^{\alpha_3 m})}{(\alpha_1 + \alpha_3)^2 e^{-\alpha_3 m} - (\alpha_1 - \alpha_3)^2 e^{\alpha_3 m}} e^{-\alpha_1 l - \alpha_1 z}] d\alpha \end{aligned} \quad (2.86a)$$

$$\begin{aligned} A^{(2)}(r, z, r_0, l) = & \frac{1}{2} \mu I r_0 \int_0^\infty J_1(\alpha r_0) J_1(\alpha r) [e^{-\alpha_1 l + \alpha_1 z} \\ & + \frac{(\alpha_1^2 - \alpha_3^2)(e^{-\alpha_3 m} - e^{\alpha_3 m})}{(\alpha_1 + \alpha_3)^2 e^{-\alpha_3 m} - (\alpha_1 - \alpha_3)^2 e^{\alpha_3 m}} e^{-\alpha_1 l - \alpha_1 z}] d\alpha \end{aligned} \quad (2.86b)$$

$$\begin{aligned} A^{(3)}(r, z, r_0, l) = & \frac{1}{2} \mu I r_0 \int_0^\infty J_1(\alpha r_0) J_1(\alpha r) e^{-\alpha_1 l} \\ & \times \frac{2\alpha_1(\alpha_1 + \alpha_3)e^{\alpha_3(z-m)} - 2\alpha_1(\alpha_1 - \alpha_3)e^{-\alpha_3(z-m)}}{(\alpha_1 + \alpha_3)^2 e^{-\alpha_3 m} - (\alpha_1 - \alpha_3)^2 e^{\alpha_3 m}}] d\alpha \end{aligned} \quad (2.86c)$$

$$\begin{aligned} A^{(4)}(r, z, r_0, l) = & \frac{1}{2} \mu I r_0 \int_0^\infty J_1(\alpha r_0) J_1(\alpha r) e^{-\alpha_1 l} \\ & \times \frac{4\alpha_1 \alpha_3 e^{\alpha_1(z-m)}}{(\alpha_1 + \alpha_3)^2 e^{-\alpha_3 m} - (\alpha_1 - \alpha_3)^2 e^{\alpha_3 m}}] d\alpha \end{aligned} \quad (2.86d)$$

where

$$\alpha_1 = \sqrt{\omega^2 \mu \epsilon - \alpha^2},$$

$$\alpha_3 = \sqrt{\alpha^2 - \omega^2 \mu \epsilon + j\omega \mu \sigma_1},$$

α is the integration variable,

σ_1 is the electrical conductivity of the metal slab,

l is the location of the exciting coil in the z direction,

r_0 is the location of the exciting coil in the r direction,

m is the lower boundary position of the metal slab, its upper boundary is at

$z=0$ position, and

$J_1(x)$ is the first order Bessel function.

Integrating the expression over the coil cross section, we obtain the following solutions for a finite cross section coil.

$$A^{(1)}(r, z) = \frac{1}{2} \mu I \int_{r_1}^{r_2} r_0 \int_0^{\infty} J_1(\alpha r_0) J_1(\alpha r) \frac{1}{\alpha_1} e^{-\alpha_1 z} [(e^{\alpha_1 l_2} - e^{\alpha_1 l_1}) + \frac{(\alpha_1^2 - \alpha_3^2)(e^{-\alpha_3 m} - e^{\alpha_3 m})}{(\alpha_1 + \alpha_3)^2 e^{-\alpha_3 m} - (\alpha_1 - \alpha_3)^2 e^{\alpha_3 m}} (e^{-\alpha_1 l_1} - e^{-\alpha_1 l_2})] d\alpha dr_0 \quad (2.87a)$$

$$A^{(12)}(r, z) = \frac{1}{2} \mu I \int_{r_1}^{r_2} r_0 \int_0^{\infty} J_1(\alpha r_0) J_1(\alpha r) \frac{1}{\alpha_1} [[2 - e^{-\alpha_1(z-l_1)} - e^{\alpha_1(z-l_2)}] + \frac{(\alpha_1^2 - \alpha_3^2)(e^{-\alpha_3 m} - e^{\alpha_3 m})}{(\alpha_1 + \alpha_3)^2 e^{-\alpha_3 m} - (\alpha_1 - \alpha_3)^2 e^{\alpha_3 m}} (e^{-\alpha_1(z+l_1)} - e^{-\alpha_1(z+l_2)})] d\alpha dr_0 \quad (2.87b)$$

$$A^{(2)}(r, z) = \frac{1}{2} \mu I \int_{r_1}^{r_2} r_0 \int_0^{\infty} J_1(\alpha r_0) J_1(\alpha r) \frac{1}{\alpha_1} [e^{-\alpha_1 l_1} - e^{-\alpha_1 l_2}] \times [e^{\alpha_1 z} + \frac{(\alpha_1^2 - \alpha_3^2)(e^{-\alpha_3 m} - e^{\alpha_3 m})}{(\alpha_1 + \alpha_3)^2 e^{-\alpha_3 m} - (\alpha_1 - \alpha_3)^2 e^{\alpha_3 m}} e^{-\alpha_1 z}] d\alpha dr_0 \quad (2.87c)$$

$$A^{(3)}(r, z) = \frac{1}{2} \mu I \int_{r_1}^{r_2} r_0 \int_0^{\infty} J_1(\alpha r_0) J_1(\alpha r) (e^{-\alpha l_1} - e^{-\alpha l_2}) \times \frac{2(\alpha_1 + \alpha_3) e^{\alpha_3(z-m)} - 2(\alpha_1 - \alpha_3) e^{-\alpha_3(z-m)}}{(\alpha_1 + \alpha_3)^2 e^{-\alpha_3 m} - (\alpha_1 - \alpha_3)^2 e^{\alpha_3 m}} d\alpha dr_0 \quad (2.87d)$$

$$A^{(4)}(r, z) = \frac{1}{2} \mu I \int_{r_1}^{r_2} r_0 \int_0^{\infty} J_1(\alpha r_0) J_1(\alpha r) (e^{-\alpha l_1} - e^{-\alpha l_2}) \times \frac{4\alpha_3 e^{\alpha_3(z-m)}}{(\alpha_1 + \alpha_3)^2 e^{-\alpha_3 m} - (\alpha_1 - \alpha_3)^2 e^{\alpha_3 m}} d\alpha dr_0 \quad (2.87e)$$

where,

l_1 and l_2 are exciting coil boundaries in the z direction,

r_1 and r_2 are exciting coil boundaries in the r direction.

Note that as σ increases from zero to $\sqrt{\omega^2 \mu \epsilon}$, α^2 becomes positive. This corresponds to a propagating wave. As α increases further, α^2 becomes negative. This corresponds to a pure diffusion process. Therefore, the magnetic vector potential at every point has two parts; one arising from wave propagation, the other is due to the diffusion process. This is as expected because the wave term is now considered in the governing equation. In general, $\sqrt{\omega^2 \mu \epsilon}$ is very small, and hence the wave contribution is much smaller than the diffusion contribution. We will label the wave contribution and diffusion contribution as $A_1^{(i)}$ and $A_2^{(i)}$, respectively. The corresponding analytical expressions are given below.

$$\begin{aligned}
A_1^1(r, z) = & \frac{1}{2} \mu I \int_{r_1}^{r_2} r_0 \int_0^{\sqrt{\omega^2 \mu \varepsilon}} J_1(\alpha r_0) J_1(\alpha r) \frac{2}{b_1} \sin(b_1 \frac{l_2 - l_1}{2}) \times \\
& \{ [\cos(b_1(\frac{l_1 + l_2}{2} - z)) + j \sin(b_1(\frac{l_1 + l_2}{2} - z))] \\
& - \frac{\omega \mu \sigma_1}{C_{11}} [\sin(b_1(\frac{l_1 + l_2}{2} + z)) + e^{2a_3 m} \sin(2b_3 m - b_1(\frac{l_1 + l_2}{2} + z))] \\
& - j \frac{\omega \mu \sigma_1}{C_{11}} [\cos(b_1(\frac{l_1 + l_2}{2} + z)) - e^{2a_3 m} \cos(2b_3 m - b_1(\frac{l_1 + l_2}{2} + z))] \} dr_0 d\alpha
\end{aligned} \tag{2.88a}$$

$$\begin{aligned}
A_2^1(r, z) = & \frac{1}{2} \mu I \int_{r_1}^{r_2} r_0 \int_0^m \frac{1}{\sqrt{\omega^2 \mu \varepsilon}} J_1(\alpha r_0) J_1(\alpha r) \frac{1}{a_1} \times \\
& \{ [e^{a_1(l_2 - z)} - e^{a_1(l_1 - z)}] \\
& - \frac{\omega \mu \sigma_1}{C_{21}} [e^{2a_3 m} \sin(2b_3 m) \\
& + j(1 - e^{2a_3 m} \cos(2b_3 m))(e^{-a_1(z+l_1)} - e^{-a_1(z+l_2)})] \} dr_0 d\alpha
\end{aligned} \tag{2.88b}$$

$$\begin{aligned}
A_1^{12}(r, z) = & \frac{1}{2} \mu I \int_{r_1}^{r_2} r_0 \int_0^{\sqrt{\omega^2 \mu \varepsilon}} J_1(\alpha r_0) J_1(\alpha r) \frac{1}{b_1} \times \\
& \{ [\sin(b_1(z - l_1)) - \sin(b_1(z - l_2))] \\
& + j[\cos(b_1(z - l_1)) + \cos(b_1(z - l_2)) - 2] \\
& - 2 \frac{\omega \mu \sigma_1}{C_{11}} \sin(b_1 \frac{l_2 - l_1}{2}) \times \\
& [[e^{2a_3 m} \sin(2b_3 m) \cos(b_1(z + \frac{l_1 + l_2}{2})) \\
& + (1 - e^{2a_3 m} \cos(2b_3 m)) \sin(b_1(z + \frac{l_1 + l_2}{2}))] \\
& + j[(1 - e^{2a_3 m} \cos(2b_3 m)) \cos(b_1(z + \frac{l_1 + l_2}{2})) \\
& - e^{2a_3 m} \sin(2b_3 m) \sin(b_1(z + \frac{l_1 + l_2}{2}))]] \} dr_0 d\alpha
\end{aligned} \tag{2.88c}$$

$$\begin{aligned}
A_2^{12}(r, z) &= \frac{1}{2} \mu I \int_{r_1}^{r_2} r_0 \int_{\sqrt{\omega^2 \mu \epsilon}}^{\infty} J_1(\alpha r_0) J_1(\alpha r) \frac{1}{a_1} \times \\
&\quad \{ [2 - e^{-a_1(z-l_1)} - e^{a_1(z-l_2)}] \\
&\quad - \frac{\omega \mu \sigma_1}{C_{21}} (e^{-a_1(z+l_1)} - e^{-a_1(z+l_2)}) \times \\
&\quad [e^{2a_3 m} \sin(2b_3 m) + j(1 - e^{2a_3 m} \cos(2b_3 m))] \} dr_0 d\alpha
\end{aligned} \tag{2.88d}$$

$$\begin{aligned}
A_1^2(r, z) &= \frac{1}{2} \mu I \int_{r_1}^{r_2} r_0 \int_0^{\sqrt{\omega^2 \mu \epsilon}} J_1(\alpha r_0) J_1(\alpha r) \frac{2}{b_1} \sin(b_1 \frac{l_2 - l_1}{2}) \times \\
&\quad \{ [\cos(b_1(z - \frac{l_1 + l_2}{2})) + j \sin(b_1(z - \frac{l_1 + l_2}{2}))] \\
&\quad - \frac{\omega \mu \sigma_1}{C_{11}} [[\sin(b_1(z + \frac{l_1 + l_2}{2})) + e^{2a_3 m} \sin(2b_3 m - b_1(z + \frac{l_1 + l_2}{2}))] \\
&\quad + j [\cos(b_1(z + \frac{l_1 + l_2}{2})) - e^{2a_3 m} \cos(2b_3 m - b_1(z + \frac{l_1 + l_2}{2}))] \} dr_0 d\alpha
\end{aligned} \tag{2.88e}$$

$$\begin{aligned}
A_2^2(r, z) &= \frac{1}{2} \mu I \int_{r_1}^{r_2} r_0 \int_{\sqrt{\omega^2 \mu \epsilon}}^{\infty} J_1(\alpha r_0) J_1(\alpha r) \frac{1}{a_1} (e^{-a_1 l_1} - e^{-a_1 l_2}) \times \\
&\quad \{ e^{a_1 z} \\
&\quad - \frac{\omega \mu \sigma_1}{C_{21}} e^{-a_1 z} [e^{2a_3 m} \sin(2b_3 m) + j(1 - e^{2a_3 m} \cos(2b_3 m))] \} dr_0 d\alpha
\end{aligned} \tag{2.88f}$$

$$\begin{aligned}
A_1^3(r, z) = & \frac{1}{2} \mu I \int_{r_1}^{r_2} r_0 \int_0^{\sqrt{\omega^2 \mu \epsilon}} J_1(\alpha r_0) J_1(\alpha r) \sin(b_1 \frac{l_2 - l_1}{2}) \frac{4}{C_{11}} \times \\
& \{e^{a_3 z} [-(b_1 + b_3) \cos(b_3 z - b_1 \frac{l_1 + l_2}{2}) - a_3 \sin(b_3 z - b_1 \frac{l_1 + l_2}{2})] \\
& + e^{-a_3(z-2m)} [(b_1 - b_3) \cos(b_3(z-2m) + b_1 \frac{l_1 + l_2}{2}) \\
& + a_3 \sin(b_3(z-2m) + b_1 \frac{l_1 + l_2}{2})] \\
& + j e^{a_3 z} [a_3 \cos(b_3 z - b_1 \frac{l_1 + l_2}{2}) - (b_1 + b_3) \sin(b_3 z - b_1 \frac{l_1 + l_2}{2})] \\
& + j e^{-a_3(z-2m)} [a_3 \cos(b_3(z-2m) + b_1 \frac{l_1 + l_2}{2}) \\
& - (b_1 - b_3) \sin(b_3(z-2m) + b_1 \frac{l_1 + l_2}{2})] \} dr_0 d\alpha
\end{aligned} \tag{2.88g}$$

$$\begin{aligned}
A_2^3(r, z) = & \frac{1}{2} \mu I \int_{r_1}^{r_2} r_0 \int_0^{\infty} \frac{1}{\sqrt{\omega^2 \mu \epsilon}} J_1(\alpha r_0) J_1(\alpha r) [e^{-a_1 l_1} - e^{-a_1 l_2}] \frac{2}{C_{21}} \times \\
& \{e^{a_3 z} [(a_1 + a_3) \cos(b_3 z) - b_3 \sin(b_3 z)] \\
& + e^{-a_3(z-2m)} [-(a_1 - a_3) \cos(b_3(z-2m)) + b_3 \sin(b_3(z-2m))] \\
& + j e^{a_3 z} [b_3 \cos(b_3 z) + (a_1 + a_3) \sin(b_3 z)] \\
& + j e^{-a_3(z-2m)} [b_3 \cos(b_3(z-2m)) + (a_1 - a_3) \sin(b_3(z-2m))] \} dr_0 d\alpha
\end{aligned} \tag{2.88h}$$

$$\begin{aligned}
A_1^4(r, z) = & \frac{1}{2} \mu I \int_{r_1}^{r_2} r_0 \int_0^{\sqrt{\omega^2 \mu \epsilon}} J_1(\alpha r_0) J_1(\alpha r) \sin(b_1 \frac{l_2 - l_1}{2}) \frac{8}{C_{11}} e^{a_3 m} \times \\
& \{[-b_3 \cos(b_1(z-m - \frac{l_1 + l_2}{2}) + b_3 m) - a_3 \sin(b_1(z-m - \frac{l_1 + l_2}{2}) + b_3 m)] \\
& + j [a_3 \cos(b_1(z-m - \frac{l_1 + l_2}{2}) + b_3 m) - b_3 \sin(b_1(z-m - \frac{l_1 + l_2}{2}) + b_3 m)] \} dr_0 d\alpha
\end{aligned} \tag{2.88i}$$

$$\begin{aligned}
A_2^4(r, z) = & \frac{1}{2} \mu I \int_{r_1}^{r_2} r_0 \int_{\sqrt{\omega^2 \mu \epsilon}}^{\infty} J_1(\alpha r_0) J_1(\alpha r) [e^{a_1(z-m-l_1)+a_3 m} - e^{a_1(z-m-l_2)+a_3 m}] \\
& \times \frac{4}{C_{21}} \{ [a_3 \cos(b_3 m) - b_3 \sin(b_3 m)] \\
& + j [b_3 \cos(b_3 m) + a_3 \sin(b_3 m)] \} dr_0 d\alpha
\end{aligned} \tag{2.88j}$$

where

$$\alpha_1 = a_1 + j b_1,$$

$$\alpha_3 = a_3 + j b_3,$$

$$a_1 = \sqrt{\alpha^2 - \omega^2 \mu \epsilon}, \alpha^2 > \omega^2 \mu \epsilon,$$

$$b_1 = \sqrt{\omega^2 \mu \epsilon - \alpha^2}, \alpha^2 < \omega^2 \mu \epsilon,$$

$$a_3 = \sqrt{\frac{1}{2} [(\alpha^2 - \omega^2 \mu \epsilon) + \sqrt{(\alpha^2 - \omega^2 \mu \epsilon)^2 + (\omega \mu \sigma_1)^2}],}$$

$$b_3 = \sqrt{\frac{1}{2} [-(\alpha^2 - \omega^2 \mu \epsilon) + \sqrt{(\alpha^2 - \omega^2 \mu \epsilon)^2 + (\omega \mu \sigma_1)^2}],}$$

$$C_{11} = (a_3 + j(b_1 + b_3))^2 - (a_3 - j(b_1 - b_3))^2 e^{2(a_3 + j b_3)m},$$

$$C_{21} = ((a_1 + a_3) + j b_3)^2 - ((a_1 - a_3) - j b_3)^2 e^{2(a_3 + j b_3)m}.$$

Since this is a complete electromagnetic process model, the result is general for two-dimensional configurations and can be applied to the following cases:

- Normal eddy current applications, where the wave term is negligible.
- High frequency applications, where the effect of the wave propagation dominates.

- Low material conductivity applications, where the wave and the diffusion terms are comparable.

When the thickness of the conducting slab extends to infinity, we have a configuration consisting of a coil over a conducting half plane.

2.7.3.1 Diffusion delay The following simulation results are obtained assuming a coil with a finite cross section of dimensions $(r_1, r_2) = (1.4, 1.5 \text{ mm})$ and $(l_1, l_2) = (0.0, 1.0 \text{ mm})$. The excitation signal consists of a positive square pulse with 0.1 ms duration.

For a conducting slab, it takes time for energy to diffuse through it. When the energy starts to diffuse into the slab, it will be some time later before the magnetic field perturbation reaches the other side. This can be demonstrated if a pickup coil is placed over the other side of the conducting lab.

The induced voltage in the pickup coil without any flaw existing in the specimen is

$$V = -\oint \vec{E} \cdot d\vec{l} \quad (2.89)$$

If the pickup coil, of radius a , is placed at the center of origin, then the electrical field along the coil is constant. Therefore,

$$\begin{aligned} V &= -2\pi a E \\ &= -2\pi a \left(-\frac{\partial}{\partial t} A - \nabla \Phi \right) \\ &= 2\pi a \frac{\partial}{\partial t} A \end{aligned} \quad (2.90)$$

Once the variation of A over time at the pickup coil location is calculated, the induced voltage signal due to the square pulse excitation can be calculated.

Figure 2.17 shows the induced voltage in the pickup coils for two different lift-off values assuming the same metal slab thickness. Here, the copper slab thickness is 1.0 mm. The first plot shows the induced voltage obtained when the pickup coil is placed in contact with the bottom of the slab at $(r, z) = (1.0, -1.0 \text{ mm})$. The second plot shows the result when the pickup coil is placed one millimeter away from the slab, at $(r, z) = (1.0, -2.0 \text{ mm})$. It is apparent that the induced voltages obtained with different pickup coil locations have the same shape, although the amplitude of the signal decays as the pickup coil moves further from the slab. The signal “arrival” time is independent of the pickup coil location (neglecting the wave propagation delay). This is in agreement with the analytical results. At low frequencies, the governing eddy current equation provides static distribution of the magnetic vector potential in lossless space. The time variation of the response depends on the time variation of the exciting current. In other words, in a lossless media, the magnetic vector potential does not exhibit wave propagation behavior. There is no time delay associated with lossless media.

Figure 2.18 shows induced voltages in the pickup coils for two different metal slab thickness. The first plot was obtained assuming that the copper slab thickness is 1.0 mm, and that the pickup coil is located at $(r, z) = (1.0, -2.0 \text{ mm})$. For the second plot, the copper slab is 2.0 mm thick and the pickup coil is located one millimeter away from the slab, at $(r, z) = (1.0, -3.0 \text{ mm})$. Comparing the induced voltages for different slab thickness, we immediately

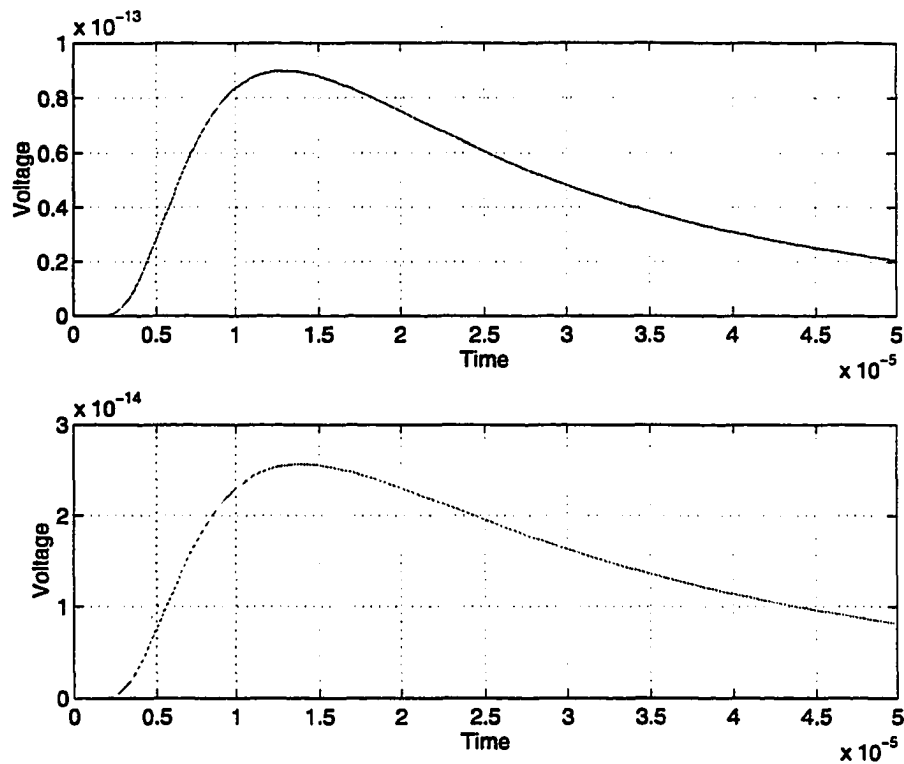


Figure 2.17. Induced voltage in pickup coil, same copper slab, different pickup coil locations

observe the difference in the signal arrival times. The signal in the second plot commences to rise at a much later time. The difference can be attributed to the difference in metal slab thickness. In fact, the solution of the eddy current governing equation is a harmonic function, both in time and in space when the input signal is a time varying harmonic. Of course, there is attenuation with respect to space. The time harmonic solution in a lossy media has the same form as a wave propagation solution. Similarly, as in the case of electromagnetic wave propagation, a lossy media introduces time delay in the eddy current signal.

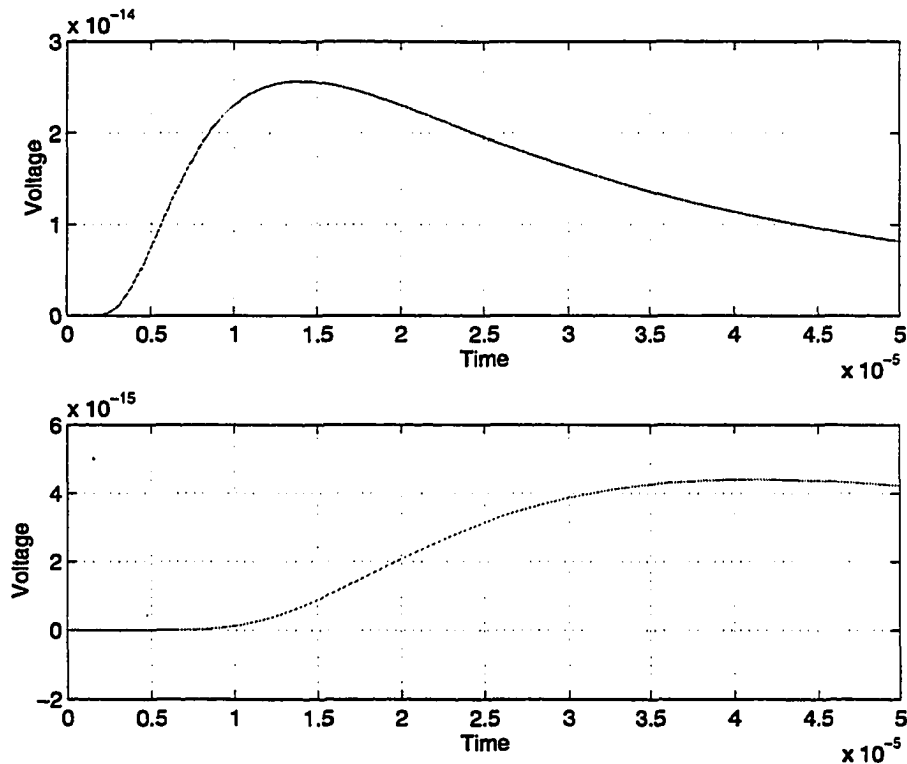


Figure 2.18. Induced voltage in pickup coil, different copper slab thickness

Note that there is a fundamental difference between the signal delay in this case and the wave signal delay. For electromagnetic propagation, the time delay associated with a signal is the time required for the wave signal to travel from one point to another. In the case of eddy currents, the delay is introduced by the diffusion process.

2.7.3.2 Flaw response at a single excitation frequency We can calculate the flaw kernels once the magnetic vector potential is calculated. Figure 2.19 shows the induced voltage flaw kernel for a tiny flaw near the top of a 5 mm thick copper slab, at $z = -0.5$ mm. The excitation coil, which also serves as a pickup coil, is located at $(r_1, r_2) = (1.4, 1.5$ mm),

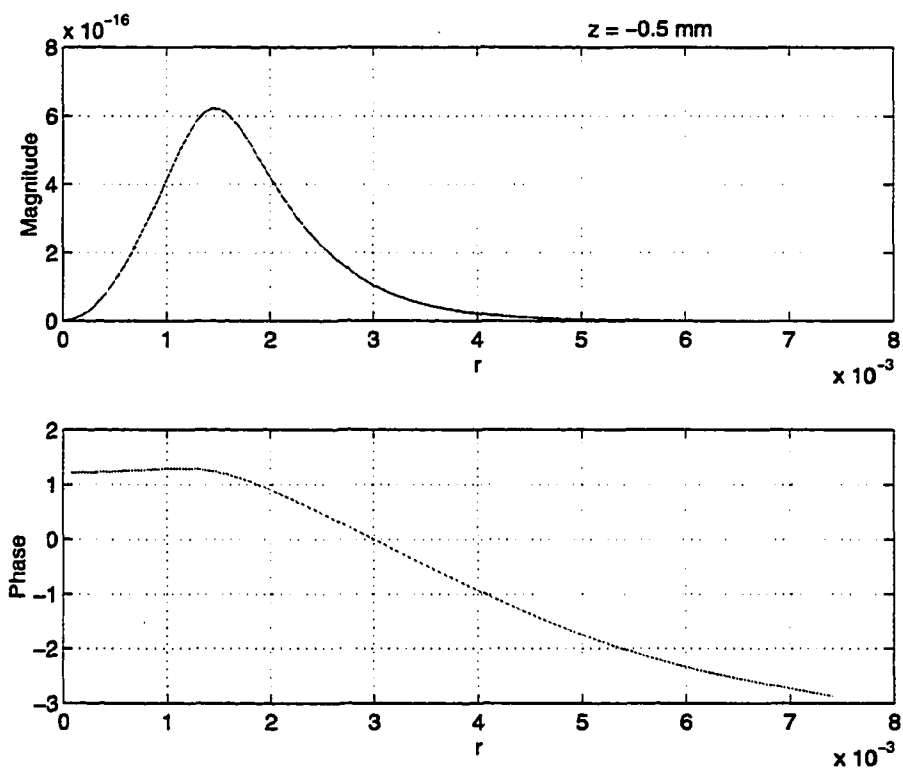


Figure 2.19. Flaw kernel of induced voltage for a flaw near the top of the specimen

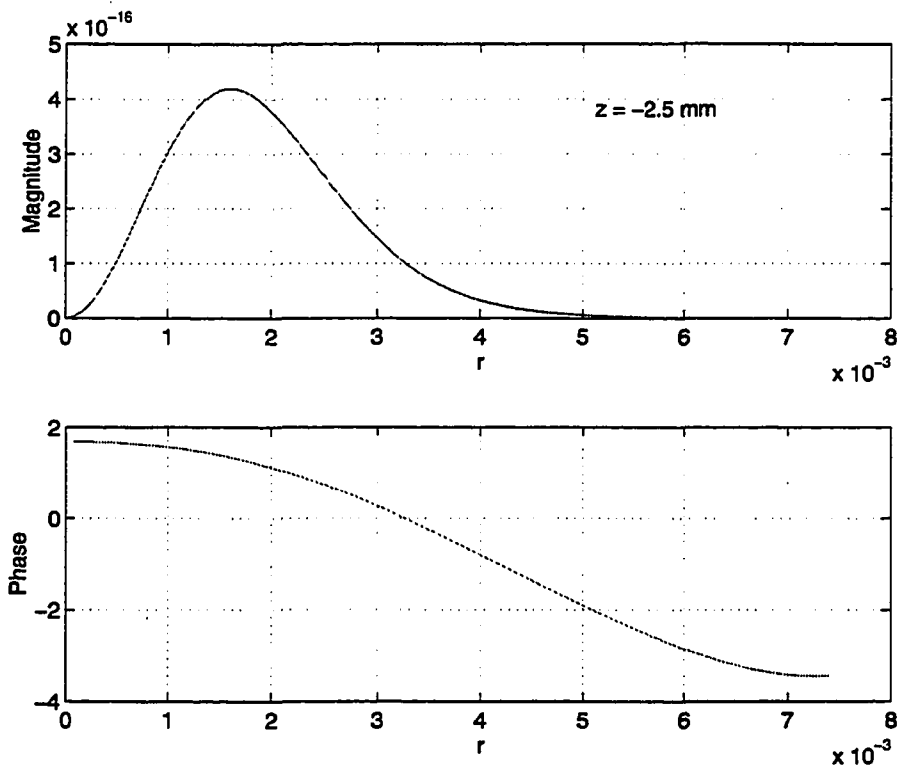


Figure 2.20. Flaw kernel of induced voltage for a flaw at the middle of the specimen

$(l_1, l_2) = (0.0, 0.1 \text{ mm})$. The excitation frequency is 5 KHz. The first plot shows the magnitude of voltage change due to the flaw while the second plot indicates the change in phase.

Similarly, Figure 2.20 shows the induced voltage signal for a tiny flaw right located at the center of the specimen, at $z = -2.5 \text{ mm}$.

As the depth of the flaw increases, the signal amplitude not only decreases, but also spreads.

2.7.3.3 Voltage change in time due to a flaw Once the flaw kernel for a single frequency is known, the flaw signal generated by a non-sinusoidal excitation source can be calculated by integrating over its constituent Fourier components. Figure 2.21 shows the signal due to a tiny flaw located inside the copper slab at $(r, z) = (1.0, -0.5 \text{ mm})$, when an excitation pulse of width 0.1 ms is applied at $t=0$ seconds.

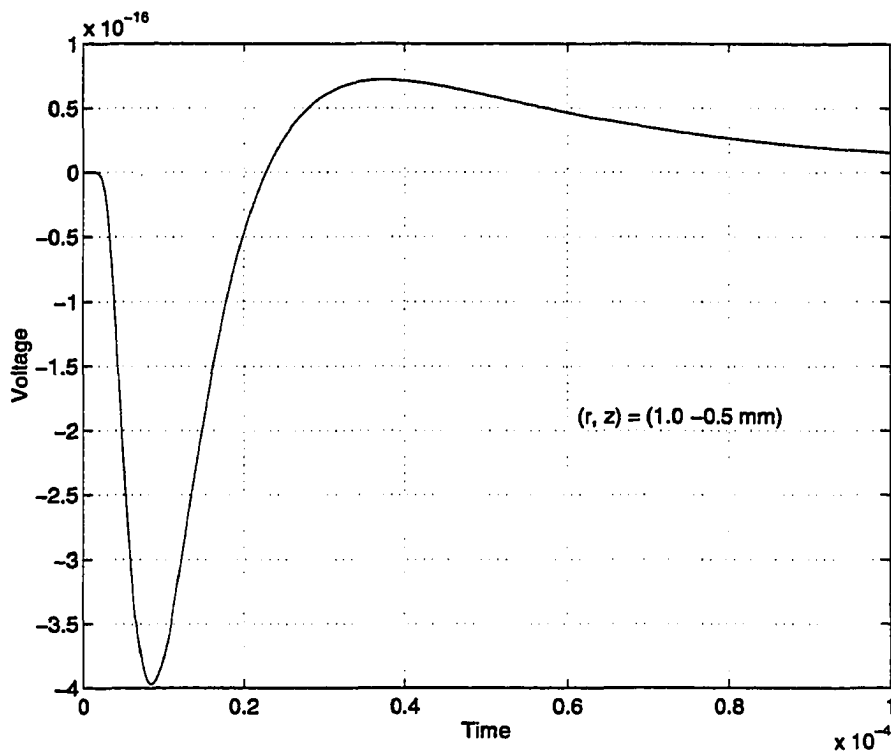


Figure 2.21. Signal generated due to a flaw at $(r, z) = (1.0, -0.5 \text{ mm})$ excited by a 0.1 ms wide pulse

Similarly, Figure 2.22 shows the signal prediction for a flaw located further away from the center, at $(r, z) = (3.0, -0.5 \text{ mm})$. The plots show that as flaw moves away from the coil, the signal spread becomes larger while the amplitude becomes smaller.

2.7.3.4 Wave propagation study As mentioned earlier, the model is capable of simulating wave effects. We consider a case where the excitation coil is located at $(r_1, r_2) = (0.5, 1.5 \text{ mm})$ and $(l_1, l_2) = (0.0, 1.0 \text{ mm})$. The excitation frequency is 100 GHz and so that

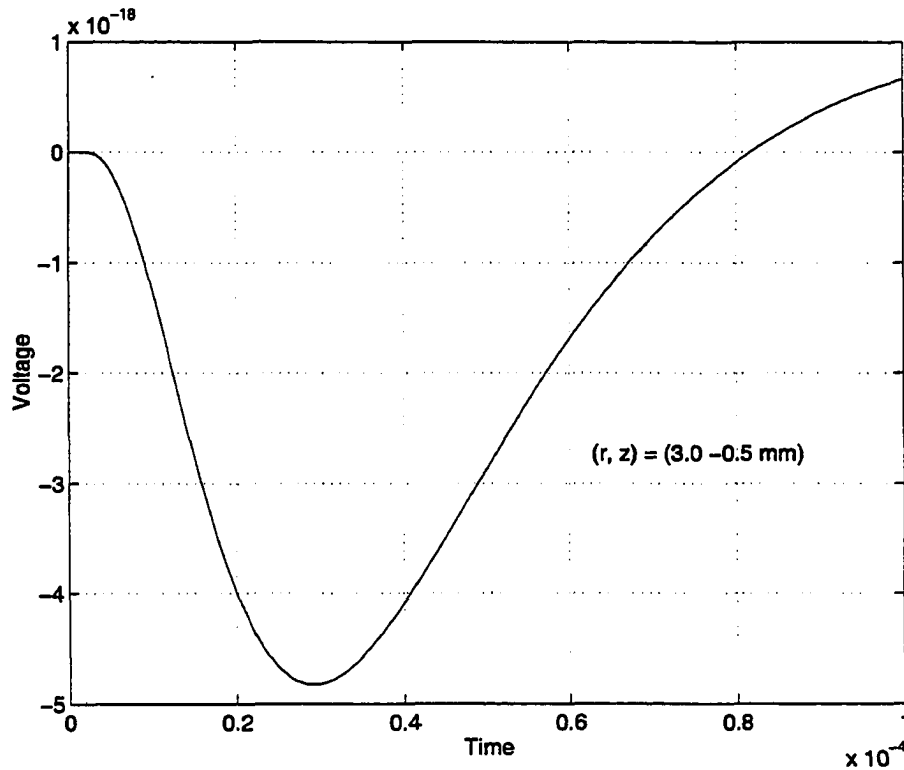


Figure 2.22. Signal generated due to a flaw at $(r, z) = (3.0, -0.5 \text{ mm})$ excited by a 0.1 ms wide pulse

the wave term has a significant effect. Figures 2.23, 2.24, 2.25 and 2.26 show the real part, imaginary part, amplitude and phase, respectively, of the magnetic vector potential A distribution over space. From the figures, and in particular from the plots of the real part and imaginary part of A , the wave propagation effect in free space is apparent. Inside the conductor, however, the attenuation is so rapid that there is virtually no electromagnetic field.

2.7.3.5 Flaw induced magnetic field signals In Section 2.6, the expressions for the flaw signal and the change in magnetic field were derived. These studies represent an important step towards developing a strategy for data fusion. The studies provide a basis for

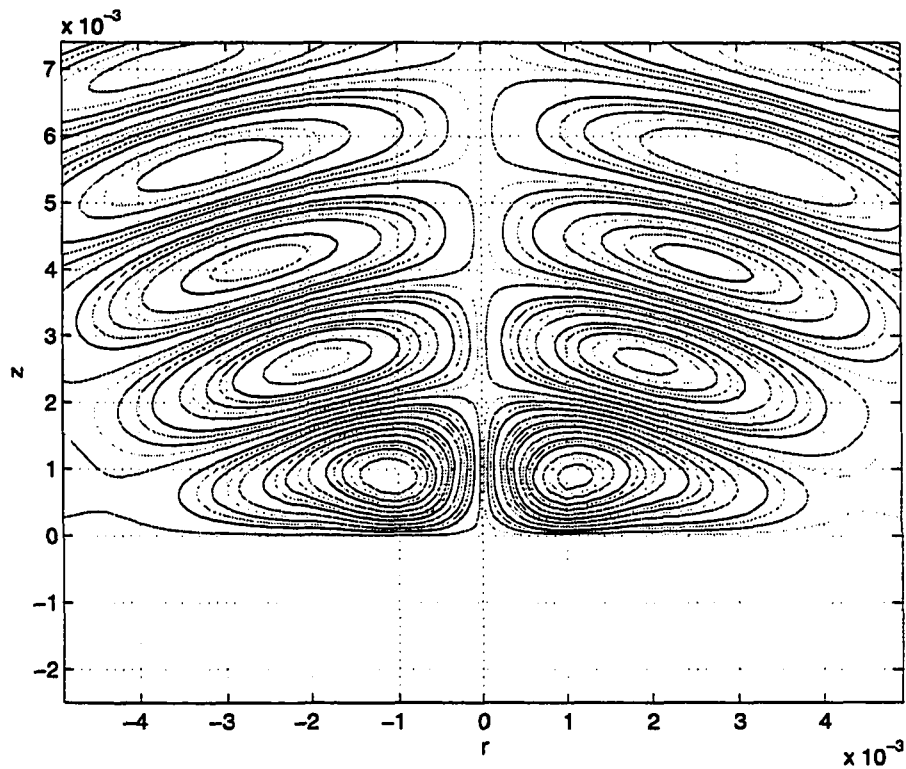


Figure 2.23. Real part of A , $f = 100$ GHz

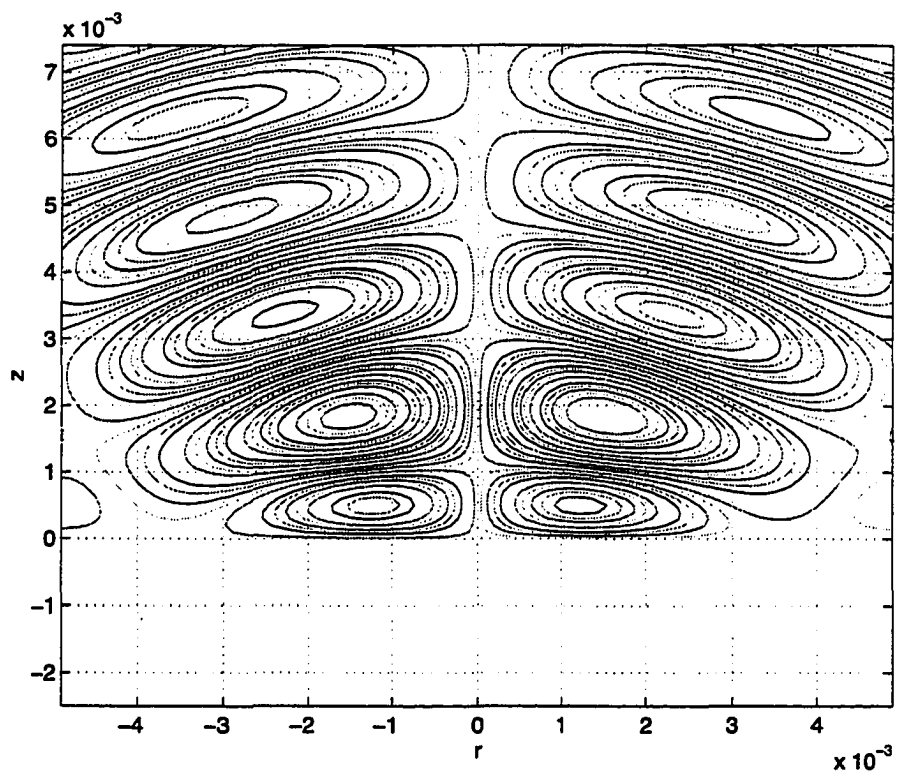


Figure 2.24. Imaginary part of A , $f = 100$ GHz

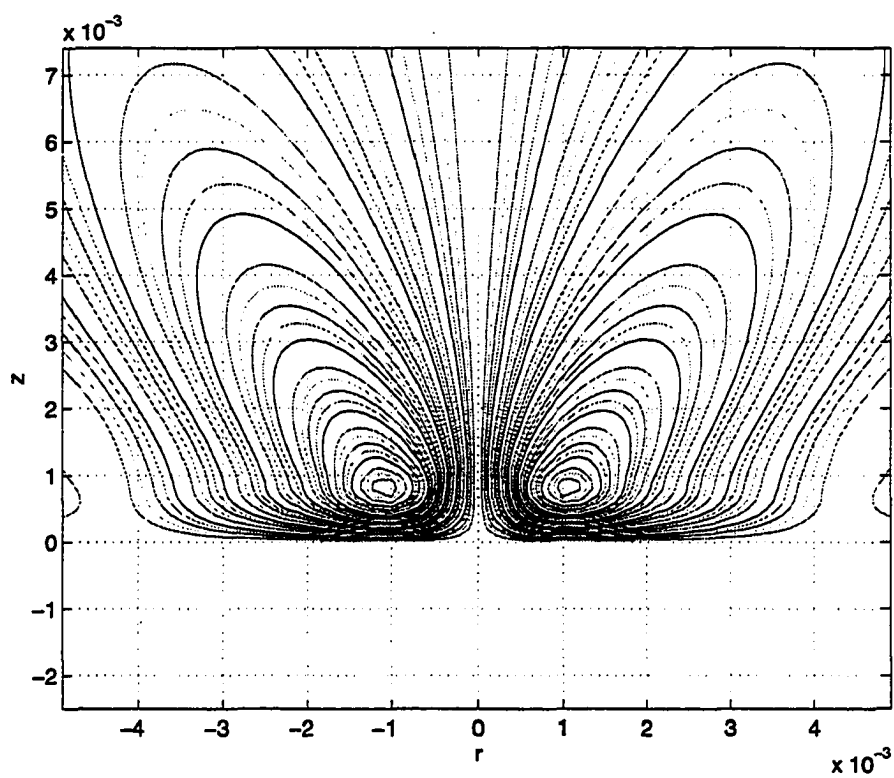


Figure 2.25. Magnitude of A , $f = 100$ GHz

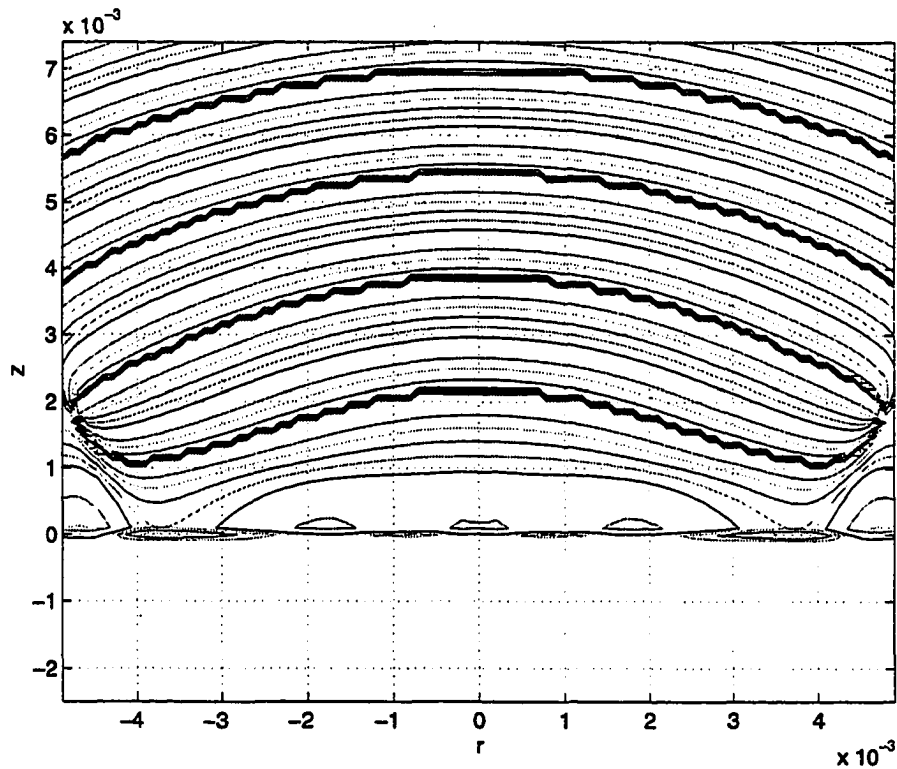


Figure 2.26. Phase of A , $f = 100$ GHz

generating field distributions for any arbitrary excitation signal. In generating these signals over a two dimensional grid, a three dimensional signal is obtained. Capturing the maximum or peak value of each time signal, one obtains a distribution of the peak values as a function of r as shown in Figure 2.27.

The copper conducting slab simulated in this study has a thickness of 5 mm. The flaw is 0.5 millimeters underneath the specimen surface and the excitation coil is at $(r_1, r_2) = (0.5, 1.5 \text{ mm})$ and $(l_1, l_2) = (0.0, 1.0 \text{ mm})$. Exploiting the spatial symmetry, one can obtain an image by plotting the amplitude of B as a function of r over a two dimensional grid. The resulting image is shown in Figure 2.28.

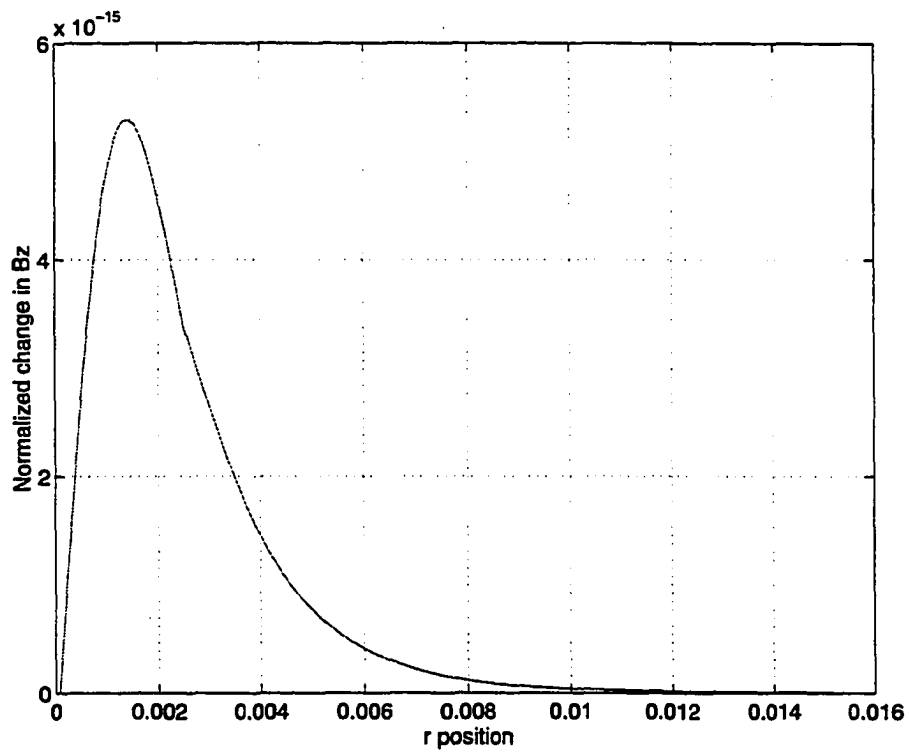


Figure 2.27. Amplitude of flaw magnetic time signal over r direction

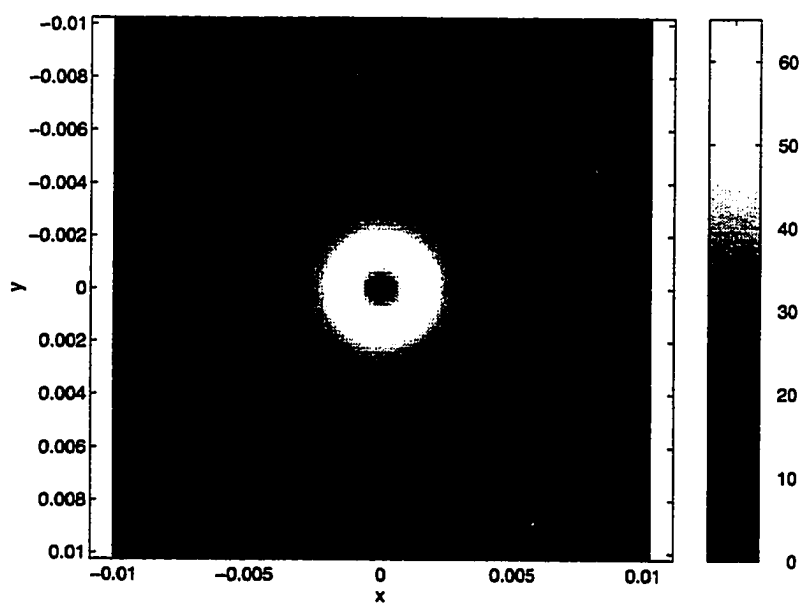


Figure 2.28. Image of the flaw magnetic field

CHAPTER III. WAVE NDE MODELING

Nondestructive evaluation methods, utilizing energy that rely on wave propagation, can exploit a variety of physical principles to evaluate the properties of the test specimen. Physical processes that are often used include wave reflection, diffraction, and scattering. For the detection and characterization of flaws, wave scattering can be used conveniently as a mechanism to derive information relating to the condition of the material. In this chapter, first a discussion relating to the analytical study of electromagnetic scattering is presented followed by the use of an existing finite element model for characterizing ultrasonic phenomena. The results will be utilized subsequently in the later chapters to generate both insight and data for implementing the fusion algorithms

3.1 Electromagnetic Wave Scattering

Electromagnetic scattering processes can be modeled in various ways [49], ranging from analytical to numerical methods such as finite element [50, 54, 55] and boundary integral methods [51, 52, 53]. In this section, the scattering process is investigated analytically. The derivation follows the procedure from Balanis [56].

Suppose that there is a conducting sphere of radius a at the origin of a spherical coordinate system. If the incident wave propagates in the positive z direction, with polarization in the x direction, then

$$\vec{E}^i = E_x^i \hat{x} = E_0 e^{-jkz} \hat{x} = E_0 e^{-jkr \cos \theta} \hat{x} \quad (3.1)$$

where $k = \omega/c$.

In spherical coordinates,

$$\bar{E}^i = E_r^i \hat{r} + E_\theta^i \hat{\theta} + E_\phi^i \hat{\phi} \quad (3.2)$$

where

$$\begin{cases} E_r^i = E_x^i \sin \theta \cos \phi = E_0 \frac{\cos \phi}{jkr} \frac{\partial}{\partial \theta} (e^{-jkr \cos \theta}) \\ E_\theta^i = E_x^i \cos \theta \cos \phi = E_0 \cos \theta \cos \phi e^{-jkr \cos \theta} \\ E_\phi^i = -E_x^i \sin \phi = -E_0 \sin \phi e^{-jkr \cos \theta} \end{cases} \quad (3.3)$$

We make use of the following transformation to write the electrical components in terms of the spherical Bessel functions:

$$e^{-jkr \cos \theta} = \sum_{n=0}^{\infty} a_n j_n(kr) P_n(\cos \theta) \quad (3.4)$$

where $a_n = j^{-n}(2n+1)$, and

$$j_n(kr) = \sqrt{\frac{\pi}{2kr}} J_{n+\frac{1}{2}}(kr), \text{ are the spherical Bessel functions.}$$

We also define

$$\bar{J}_n(x) = x j_n(x) \quad (3.5)$$

$$\partial P_n(\cos\theta)/\partial\theta = P_n'(\cos\theta) \quad (3.6)$$

Then the electrical field components are:

$$\begin{cases} E_r^i = -jE_0 \frac{\cos\phi}{(kr)^2} \sum_{n=0}^{\infty} j^{-n} (2n+1) \hat{J}_n(kr) P_n'(\cos\theta) \\ E_\theta^i = E_0 \frac{\cos\theta \cos\phi}{kr} \sum_{n=0}^{\infty} j^{-n} (2n+1) \hat{J}_n(kr) P_n(\cos\theta) \\ E_\phi^i = -E_0 \frac{\sin\phi}{kr} \sum_{n=0}^{\infty} j^{-n} (2n+1) \hat{J}_n(kr) P_n(\cos\theta) \end{cases} \quad (3.7)$$

The incident and scattered fields can be expressed as a superposition of the transverse electric (TE^r) and transverse magnetic (TM^r) components, respectively.

The TE^r fields are constructed by letting $\bar{A} = 0$ and $\bar{F} = F_r(r, \theta, \phi) \bar{r}$.

The TM^r fields are constructed by letting $\bar{F} = 0$ and $\bar{A} = A_r(r, \theta, \phi) \bar{r}$.

Letting $E_r^i = \frac{1}{j\omega\mu\epsilon} (\frac{\partial^2}{\partial r^2} + k^2) A_r^i$, we have

$$A_r^i = E_0 \frac{\cos\phi}{\omega} \sum_{n=1}^{\infty} a_n \hat{J}_n(kr) P_n'(\cos\theta) \quad (3.8)$$

where $a_n = j^{-n} \frac{2n+1}{n(n+1)}$. This expression for A_r^i gives the correct E_r^i and $H_r^i = 0$ at the

same time. Similarly, the TE^r mode ($H_r^i \neq 0, E_r^i = 0$) can be expressed as:

$$F_r^i = E_0 \frac{\sin\phi}{\omega\mu} \sum_{n=1}^{\infty} a_n \hat{J}_n(kr) P_n(\cos\theta) \quad (3.9)$$

The sum of A_r^i and F_r^i gives the correct incident wave for all three components.

The scattered field can also be represented by TM' and TE' modes:

$$\begin{cases} A_r^s = E_0 \frac{\cos \phi}{\omega} \sum_{n=1}^{\infty} b_n \hat{H}_n^{(2)}(kr) P_n'(\cos \theta) \\ F_r^s = E_0 \frac{\sin \phi}{\omega \mu} \sum_{n=1}^{\infty} c_n \hat{H}_n^{(2)}(kr) P_n'(\cos \theta) \end{cases} \quad (3.10)$$

where the spherical Hankel function of the second kind $\hat{H}_n^{(2)}$ represents outward traveling waves and b_n and c_n are to be determined by imposing appropriate boundary conditions.

The total field is the sum of the incident and the scattered fields, given by

$$\begin{cases} A_r^t = A_r^i + A_r^s \\ F_r^t = F_r^i + F_r^s \end{cases} \quad (3.11)$$

The components of the electromagnetic field are expressed in terms of A_r^t and F_r^t as

follows:

$$\begin{cases} E_r^t = \frac{1}{j\omega\mu\epsilon} \left(\frac{\partial^2}{\partial r^2} + k^2 \right) A_r^t \\ E_\theta^t = \frac{1}{j\omega\mu\epsilon} \frac{1}{r} \frac{\partial^2 A_r^t}{\partial r \partial \theta} - \frac{1}{\epsilon} \frac{1}{r \sin \theta} \frac{\partial F_r^t}{\partial \phi} \\ E_\phi^t = \frac{1}{j\omega\mu\epsilon} \frac{1}{r \sin \theta} \frac{\partial^2 A_r^t}{\partial r \partial \phi} + \frac{1}{\epsilon} \frac{1}{r} \frac{\partial F_r^t}{\partial \theta} \\ H_r^t = \frac{1}{j\omega\mu\epsilon} \left(\frac{\partial^2}{\partial r^2} + k^2 \right) F_r^t \\ H_\theta^t = \frac{1}{\mu} \frac{1}{r \sin \theta} \frac{\partial A_r^t}{\partial \phi} + \frac{1}{j\omega\mu\epsilon} \frac{1}{r} \frac{\partial^2 F_r^t}{\partial r \partial \theta} \\ E_\phi^t = -\frac{1}{\mu} \frac{1}{r} \frac{\partial A_r^t}{\partial \theta} + \frac{1}{j\omega\mu\epsilon} \frac{1}{r \sin \theta} \frac{\partial^2 F_r^t}{\partial r \partial \phi} \end{cases} \quad (3.12)$$

Applying the boundary condition for E on the sphere's surface:

$$\begin{cases} E_\theta^i(r = a, 0 \leq \theta \leq \pi, 0 \leq \phi \leq 2\pi) = 0 \\ E_\phi^i(r = a, 0 \leq \theta \leq \pi, 0 \leq \phi \leq 2\pi) = 0 \end{cases} \quad (3.13)$$

we obtain results for the two unknown coefficients

$$\begin{aligned} b_n &= -a_n \frac{\tilde{J}_n'(ka)}{\tilde{H}_n^{(2)'}(ka)} \\ c_n &= -a_n \frac{\tilde{J}_n(ka)}{\tilde{H}_n^{(2)}(ka)} \end{aligned} \quad (3.14)$$

Therefore,

$$\begin{cases} E_r^s = -jE_0 \cos\phi \sum_{n=1}^{\infty} b_n [\tilde{H}_n^{(2)'}(kr) + \tilde{H}_n^{(2)}(kr)] P_n^1(\cos\theta) \\ E_\theta^s = \frac{E_0}{kr} \cos\phi \sum_{n=1}^{\infty} [jb_n \tilde{H}_n^{(2)'}(kr) \sin\theta P_n^{1'}(\cos\theta) - c_n \tilde{H}_n^{(2)}(kr) \frac{1}{\sin\theta} P_n^1(\cos\theta)] \\ E_\phi^s = \frac{E_0}{kr} \sin\phi \sum_{n=1}^{\infty} [jb_n \tilde{H}_n^{(2)'}(kr) \frac{1}{\sin\theta} P_n^1(\cos\theta) - c_n \tilde{H}_n^{(2)}(kr) \sin\theta P_n^{1'}(\cos\theta)] \end{cases} \quad (3.15)$$

The result can be applied anywhere in space. Focusing the study on the far field region, $kr \rightarrow \infty$, we get

$$\tilde{H}_n^{(2)}(kr) \rightarrow j^{n+1} e^{-jkr} \quad (3.16)$$

Using this result the scattering in the far field region is given by:

$$\begin{cases} E_r^s = 0 \\ E_\theta^s = jE_0 \frac{e^{-jk r}}{kr} \cos \phi \sum_{n=1}^{\infty} j^n [b_n \sin \theta P_n^{1'}(\cos \theta) - c_n \frac{1}{\sin \theta} P_n^1(\cos \theta)] \\ E_\phi^s = jE_0 \frac{e^{-jk r}}{kr} \sin \phi \sum_{n=1}^{\infty} j^n [b_n \frac{1}{\sin \theta} P_n^1(\cos \theta) - c_n \sin \theta P_n^{1'}(\cos \theta)] \end{cases} \quad (3.17)$$

We simplify the expressions further by assuming that the scattering sphere is very small compared to the incident wavelength, $ka \ll 1$. In this case, we can approximate by retaining only one term for each field component. Writing out the b and c coefficients, we obtain:

$$\begin{cases} E_r^s = E_0 \sin \theta \cos \phi (ka)^3 \frac{2j}{(kr)^2} e^{-jk(r-a)} \\ E_\theta^s = E_0 \cos \phi (ka)^3 \left(-\frac{1}{2} \sin 2\theta - \frac{1}{2}\right) \frac{1}{kr} e^{-jk(r-a)} \\ E_\phi^s = E_0 \sin \phi (ka)^3 \left(-\frac{1}{4} \sin 2\theta - 1\right) \frac{1}{kr} e^{-jk(r-a)} \end{cases} \quad (3.18)$$

The scattered field has a much smaller r component.

When the incident field is non-polarized, the measurement represents the scattered energy, which can be calculated by integrating the square of the electric field over ϕ . As an illustration, a typical scattered energy plot is shown in Figure 3.1. The conducting sphere has a radius of 0.1 millimeter and the non-polarizing incident wave has a frequency of 50 GHz. The calculation is performed over a plane 5.0 millimeters above the sphere.

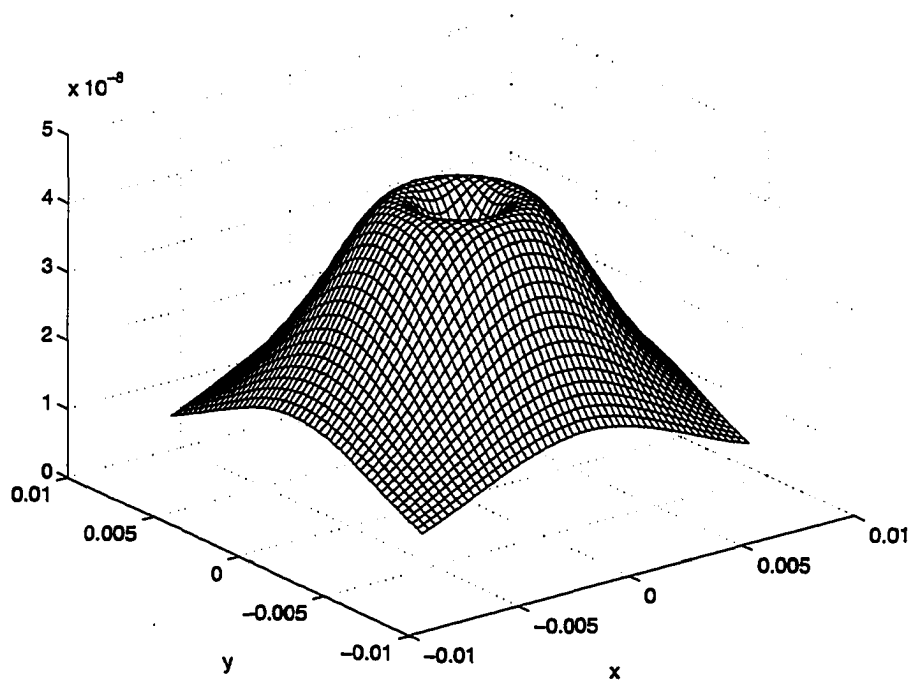


Figure 3.1. Scattered electromagnetic energy by a tiny flaw

In order to develop the data fusion algorithms within a realistic framework, we have chosen to use ultrasonic data instead of high frequency EM fields. Since high frequency EM fields cannot “penetrate” metals and eddy current methods can be used for inspecting conducting materials only, the development of algorithms for fusing data from the two methods is of limited interest. In contrast eddy current and ultrasonic methods can be utilized for inspecting similar kinds of materials and one may therefore profit from fusing data from the two tests. The following section describes the use of ultrasonics in NDE and presents a finite element model characterizing the phenomena.

3.2 Ultrasonic Wave Scattering

3.2.1 Introduction

Ultrasonic wave scattering phenomena is used very widely in nondestructive evaluation. Although many analytical models have been proposed [111-115], the complex tensor expression of the governing equation, together with the awkward nature of the boundary conditions makes numerical methods such as the finite element method [57, 58, 59, 60, 61, 110] highly attractive.

Ultrasonic waves are mechanical vibrations that occur because of the elastic properties of the material. These waves are induced by the vibration of particles in the material. When the particle vibration is sinusoidal, the wavelength, λ , is related to the velocity of the wave, v , by

$$\lambda = v / f \quad (3.19)$$

where f is the frequency of the vibration. The wave velocity of a material is related to its rigidity.

The governing equation for the ultrasonic wave is

$$\nabla \cdot \bar{\bar{T}} + \bar{f} = \rho \frac{\partial^2 \bar{u}}{\partial t^2} \quad (3.20)$$

where $\bar{\bar{T}}$ is the stress tensor,

\bar{f} is the body force,

ρ is the material density, and

\vec{u} is the displacement.

The left hand side represents forces acting on the system and the right hand side represents the material reaction to the force. Note that the first forcing term describes the intrinsic elastic properties of the material while the second term describes the external influence. The solution of the governing equation is the ultrasonic wave field distribution over space and time.

If the displacement of a wave is in the same direction as the one it is traveling, the wave is called a longitudinal wave. Longitudinal waves can exist in solids, liquids and gases. If the direction of displacement is perpendicular to the direction of wave propagation, it is called a shear wave or transverse wave. Shear waves can exist only in a solid material. As a result, mode conversion occurs at liquid-solid interfaces.

3.2.2 Ultrasound generation

Ultrasonic waves can be generated using various methods. In most nondestructive testing applications, piezoelectric transducers are used as both transmitter and receiver probes. A piezoelectric material has the property that it deforms when subjected to an external voltage, that is, it expands or compresses in a certain direction. This piezoelectric effect is exploited to construct ultrasonic transmitters. On the other hand, if a piezoelectric material is subjected to an external pressure, a voltage is produced across the material. This is called inverse piezoelectric effect and is the basis for building transducers that can receive ultrasonic signals and convert them to electrical signals. Therefore, an ultrasonic signal can

be produced with a piezoelectric transducer by applying an appropriate electrical signal to it. There are many materials which display piezoelectric properties. Natural crystals, such as quartz and lithium sulphate as well as fabricated polycrystalline ceramics, such as Barium Titanate, can be used in piezoelectric transducers for ultrasonic NDE applications.

3.2.3 Ultrasonic NDE systems

A typical ultrasonic NDE system setup is in Figure 3.2. The ultrasonic signal is generated by applying an electrical pulse to the transducer. The resulting ultrasonic pulse propagates into the specimen through a coupling medium such as water. Part of the signal propagates through the specimen while a portion of the signal undergoes attenuation during propagation. In addition a portion of the signal is reflected back, by the sample boundaries, sample property inhomogeneities and by flaws in the sample. In a pulse-echo set up, the reflected ultrasonic signal is received by the same transducer. The transducer converts the signal into an electrical signal which is then amplified and analyzed.

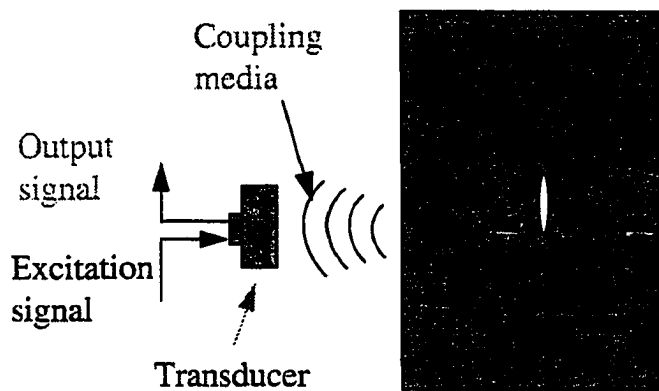


Figure 3.2. Ultrasonic NDE setup in pulse-echo mode

The ultrasonic output signal, therefore, is a signal whose amplitude varies as a function of time. There are multiple peaks in an echo signal due to reflections at various boundaries and flaw locations. A typical output signal is shown in Figure 3.3.

Normally, only a portion of the output ultrasonic signal is used for signal processing. This windowed version of the full one-dimensional signal is called an A-scan signal. If the A-scan signals are collected along a straight line over a specimen, then a two-dimensional image called the B-scan image can be generated. One axis of the B-scan image represents data sampling location, while the other represents the time of the signal at a given point. In many applications, only the peak value of the A-scan signal is captured. If the specimen is scanned and the peak values are collected over a two-dimensional grid, the resulting gray scale image is called a C-scan image.

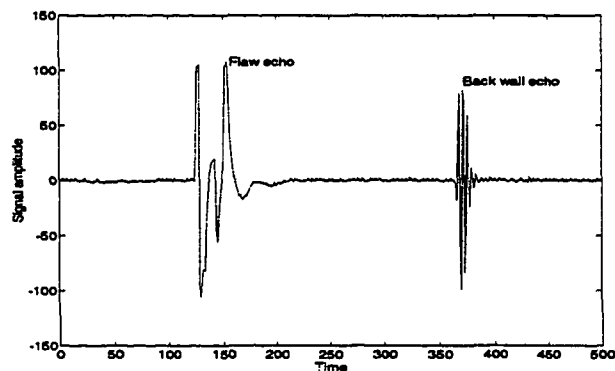


Figure 3.3. Ultrasonic NDE output signal

3.2.4 Finite element study of ultrasonic signals

The finite element method [57, 59-61, 110, 118-120] is a numerical technique for solving the governing partial differential equation (3.20) in a region of interest by decomposing the domain of interest into smaller subdomains, called elements [57]. Instead of solving the governing equation directly the method involves minimization of a global energy functional. The minimization of the energy functional with respect to a set of discrete points, called nodes, produces a field distribution which satisfies the governing equation at all the nodal points. By a proper discretization of the domain, an accurate field distribution (displacement) represented by the values at nodal points can be calculated. In ultrasonics, the energy functional, as the name implies, represents the system total energy, including kinetic and potential energy. The solution of ultrasonic governing equation corresponds to a state with minimum elastic energy.

In the process of minimizing the energy functional, the variation of the energy functional is calculated with respect to a small variation of the displacement at each node. The minimization is achieved by setting the variations to be zero. This produces a set of linear equations with the unknown variables being the displacement at all the nodes.

Once the displacement values at the discretized nodal points are known, the displacement is completely determined at any point by interpolation with a set of predefined shape functions. The finite element model proposed by Lord *et al* [118-121] uses the finite difference method to step through the solution process in time.

In order to minimize the computational effort, we restrict our study to geometries that are two dimensional. The test specimen consists of a 5.0 millimeter thick slab with a longitudinal ultrasonic velocity of 6.3×10^3 m/s. The specimen contains a spherical void of radius 0.5 mm, at the center of the specimen, at location $(x, y, z) = (0.0, 0.0, 2.5 \text{ mm})$. We excite the specimen at the top using a point contact transducer.

The excitation signal is a raised-cosine waveform lasting for one cycle, i.e.,

$$F_w(x, t) = \delta(x)[1 - \cos(\omega_1 t)]\cos(\omega_0 t), \quad 0 \leq t \leq T, \quad (3.21)$$

where,

$$f_0 = 10 \text{ MHz},$$

$$\omega_0 = 2\pi f_0,$$

$$\omega_1 = \omega_0 / 3, \text{ and}$$

$$T = 1/f_1.$$

Therefore, $T = 3.0 \times 10^{-7}$ s. The excitation signal together with its spectrum is shown in Figures 3.4 and 3.5, respectively. The spectrum shows that the bulk of the energy is centered around 10 MHz.

We use a finite element model [110] to obtain the z component of the displacement at the surface of the specimen ($z = 0$).

The ultrasonic signal consists of multiple peaks even if no flaw is present in a test specimen. The multiple peaks originate from the reflection of incident signals by the specimen boundaries. The situation is further complicated due to mode conversions at the

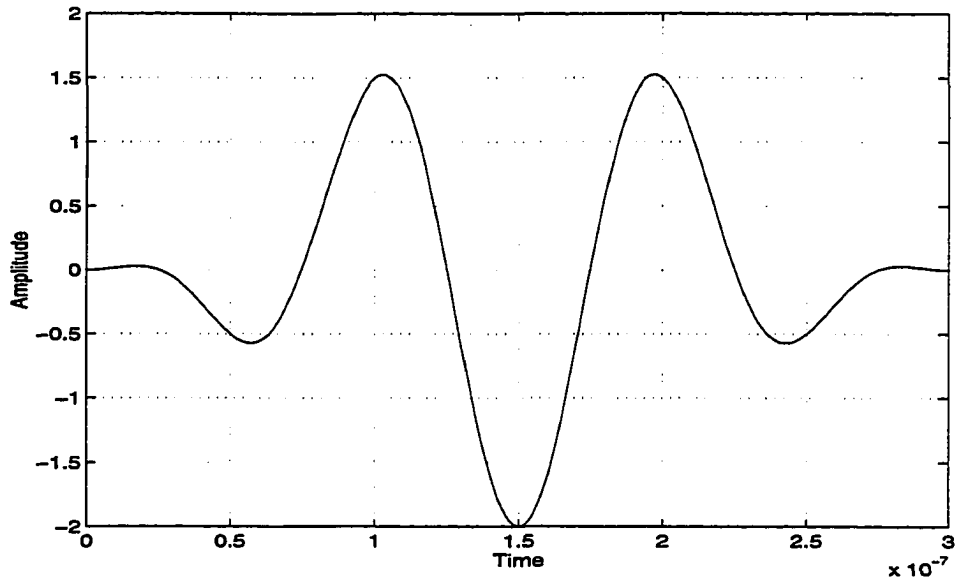


Figure 3.4. The raised-cosine excitation signal used in modeling studies

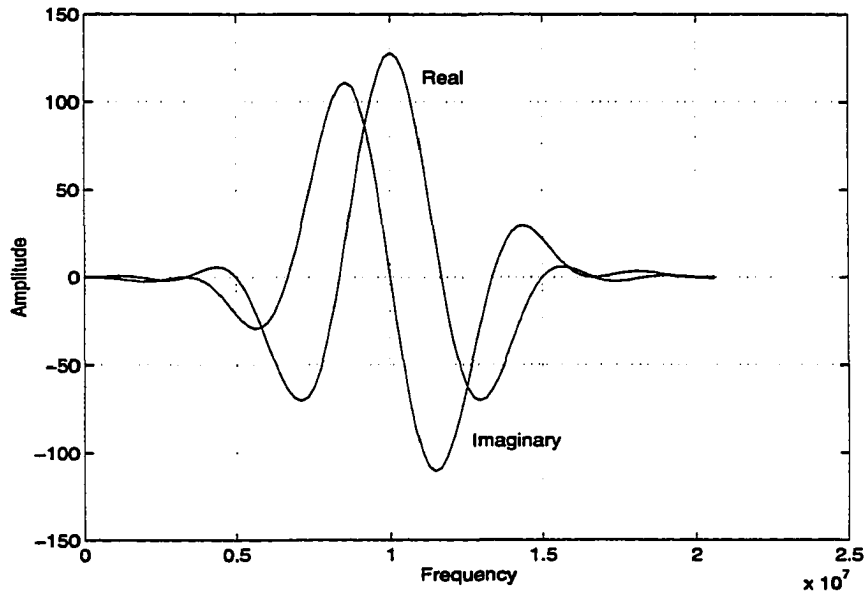


Figure 3.5. Fourier transform of the raised-cosine excitation signal

interfaces. Figure 3.6 shows the A-scan signal generated by the finite element model. Figure 3.7 shows an A-scan signal obtained without the flaw. The difference between the signal obtained with and without the flaw represents a contribution to the signal by the flaw. The difference signal generated by the spherical flaw is shown in Figure 3.8.

The flaw signals were computed using the finite element model over a circular grid at a variety of radii. The signals are assembled to produce a three dimensional image. The peak values of each A-scan was captured to generate a C-scan image which, each pixel has a gray level that corresponds to the amplitude of the peak value of the signal at that point. The C-scan image thus obtained is shown in Figure 3.9.

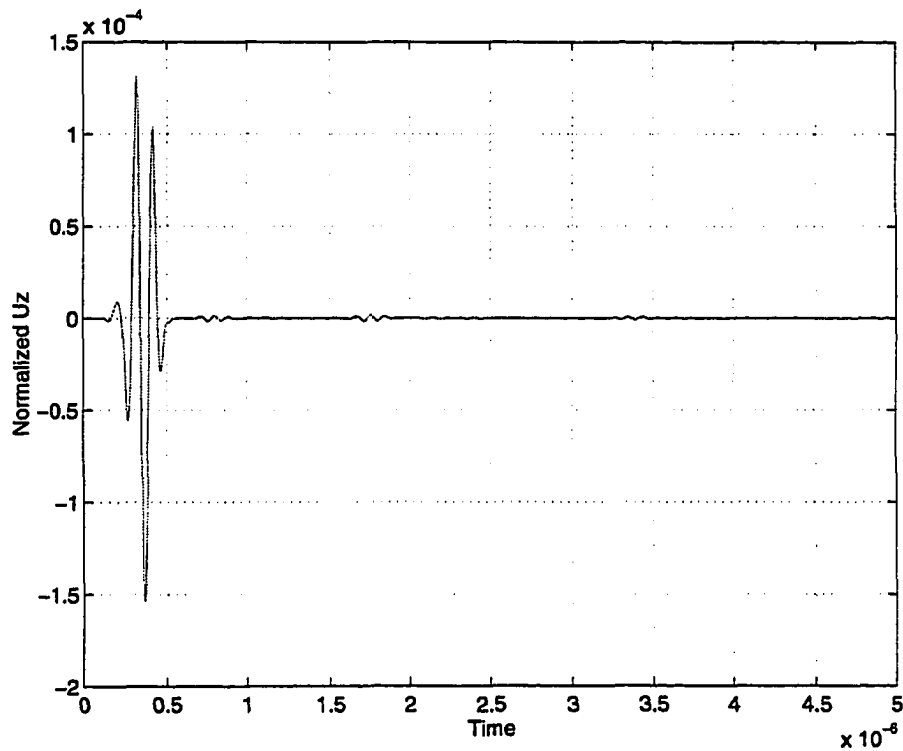


Figure 3.6. Ultrasonic A-scan signal with flaw

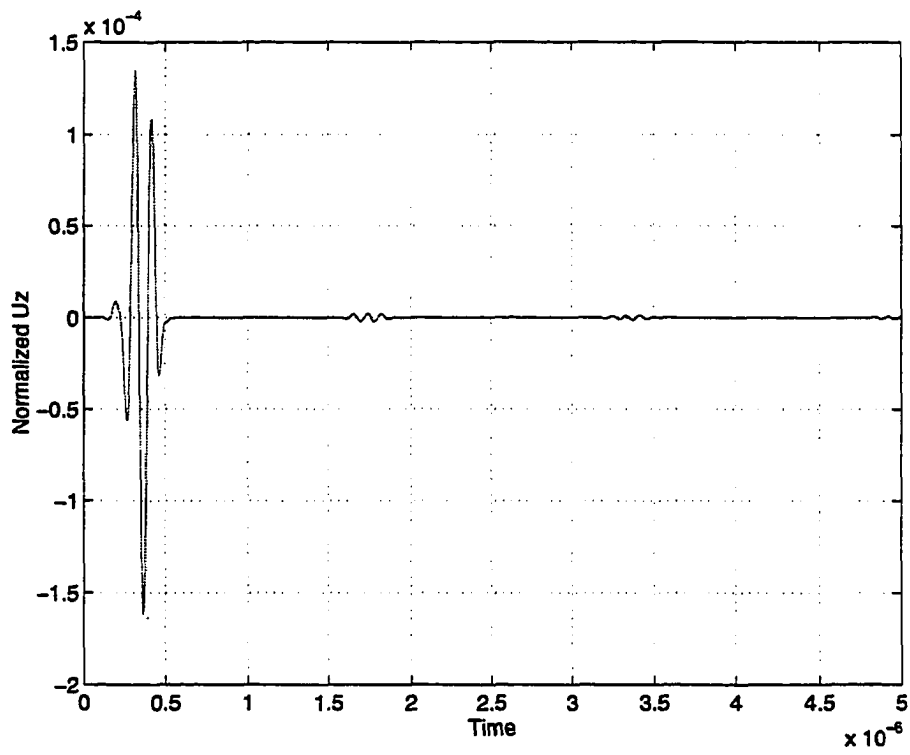


Figure 3.7. Ultrasonic A-scan signal without flaw

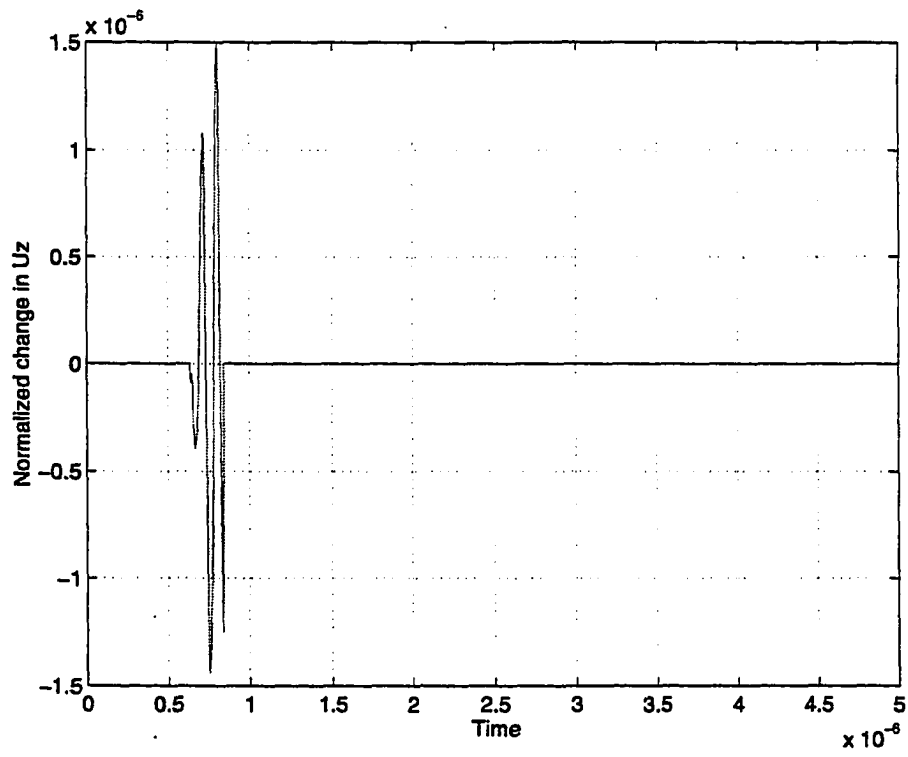


Figure 3.8. Ultrasonic A-scan signal due to flaw

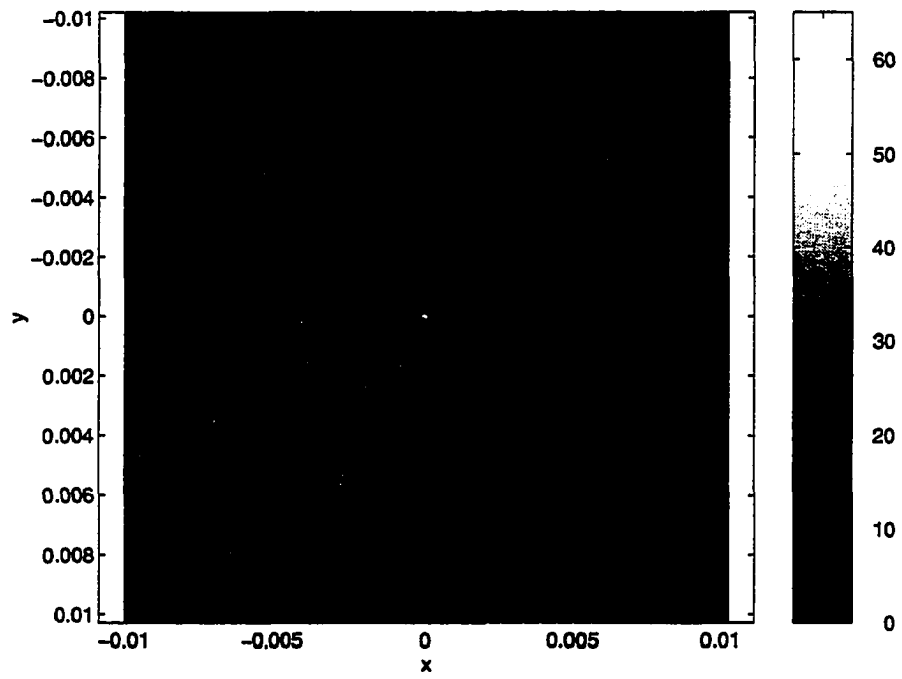


Figure 3.9. Ultrasonic C-scan image

3.3 Degradation of Ultrasonic Signals

Ultrasonic signals and images are often affected by noise that is introduced by the measurement process. Part of the noise is caused by unwanted artifacts generated within the specimen itself. The rest is due to electronic system noise. The sources of ultrasonic signal degradation is briefly presented below.

3.3.1 Specimen noise

Most of conducting materials have a granular micro-structure. In the case of aluminum and carbon steel, for example, they are composed of microscopic crystals which are bound together randomly. Each crystal has a size ranging from a few micrometers to as large as a few millimeters. Similarly, in many composite materials, the structure is composed of micro fabric molecules. Other materials, such as ceramic and cement, have porous microstructures. The microstructures have sizes that match ultrasonic wavelengths that are typically used in NDE applications. These microstructures contribute to strong diffraction effects. The diffraction signal contribution to the overall output signal represents noise. In many cases, the signal of interest (for example, flaw signal) is tiny in relation to noise. The problem caused by the granular structure diffraction places a severe limit on the detection ability.

3.3.2 Electronic noise

The other noise sources are due to analog-to-digital conversion and electronic system noise. The signal from the transducer is typically amplified and bandpass filtered. The flaw

signal is usually small and in many cases the signal has to be amplified significantly prior to analog-to-digital conversion. In the amplification process, any electronic noise present at the input is also amplified. There are many potential sources of noise at the input stage. These include digital switching noise, power line noise and EMI noise, just to name a few.

The analog-to-digital conversion process is another source of noise in an ultrasonic NDE system. Jitter in the data acquisition time base contributes to uncertainty in the output signal. This effect can be minimized by using a stable clock and utilizing an accurate synchronization method between the data acquisition unit and the pulser unit. The second contributory source is the quantization noise.

Consider a $(b+1)$ -bit quantizer where the quantization step is Δ . If the input range is $-X_m < x[n] \leq X_m$, then the error between the quantizer output $\hat{x}[n]$ and the input $x[n]$ is

$$e[n] = \hat{x}[n] - x[n] \quad (3.22)$$

It follows that

$$-\Delta/2 < e[n] \leq \Delta/2 \quad (3.23)$$

In general, one can assume that the error is uniformly distributed over its range. The variance of the quantizer error then is

$$\begin{aligned} \sigma_e^2 &= \int_{-\frac{\Delta}{2}}^{\frac{\Delta}{2}} \frac{1}{\Delta} e^2 de \\ &= \frac{\Delta^2}{12} \\ &= \frac{1}{12} \frac{X_m^2}{2^{2b}} \end{aligned} \quad (3.24)$$

Compared with the input variance of σ_x , the signal-to-noise ratio (SNR) of a quantizer is

$$\begin{aligned} SNR &= 10\log_{10}\left(\frac{\sigma_x^2}{\sigma_e^2}\right) = 10\log_{10}\left(\frac{12 \cdot 2^{2b} \sigma_x^2}{X_m^2}\right) \\ &= 6.02b - 20\log_{10}\left(\frac{X_m}{\sigma_x}\right) - 10.8 \end{aligned} \quad (3.25)$$

For example, for a 8-bit quantizer and an input variance of $\sigma_x = X_m/4$, the output signal-to-noise ratio is limited to a maximum of 47 dB.

In summary, ultrasonic NDE systems are characterized by low signal-to-noise ratio. Compared with eddy current NDE systems, however, ultrasonic NDE systems provide superior resolution and an ability to detect and characterize subsurface defects.

CHAPTER IV. DATA FUSION

4.1 Introduction to Data Fusion

During the 1980s [24], a new discipline called multisensor data fusion, or distributed sensing, has developed in response to a diverse set of problems. Multisensor data fusion is an evolving field that is concerned with the task of combining data from multiple, and possibly a diverse set, of sensors in order to draw inferences about a physical event or situation. Applications of data fusion span two broad areas. The first is concerned primarily with military applications while the other is focused on theoretical developments and nonmilitary applications. An example of the latter class of problems includes satellite remote sensing which is used extensively for the determination of the composition of ground vegetation or location of mineral resources.

The study of data fusion is complicated by the breadth of applications across these two communities and by the diversity of techniques that are employed. Data fusion techniques represent a seeming hodgepodge of mathematical and heuristic techniques drawn from the realms of statistics, artificial intelligence, pattern recognition, operations research, digital signal processing, and decision theory.

Data fusion techniques, in principle, are analogous to cognitive processes used by humans to integrate data continually from their senses to make inferences about the external world. Humans receive sensory data - sights, sounds, smells, tastes, and touch - which are then assessed to draw conclusions about the environment and what it means. For instance,

recognition of an acquaintance whom one has not seen for a long period of time may involve assessment of factors such as general facial shape, identification of distinctive visual features, identification of voice tonal patterns, or even distinctive ways of walking or gesturing. Many of the techniques developed for data fusion attempt to emulate the ability of humans to fuse multiple sets of data.

4.2 Data Fusion Systems

4.2.1 Generic data fusion model

A model for a generic data fusion system is shown in Figure 4.1.

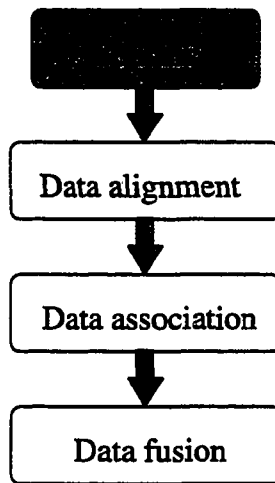


Figure 4.1. A generic data fusion system model

At the top, the model shows input data derived from multiple sensors, which can be either homogeneous or heterogeneous. The major functional blocks for data fusion systems include data alignment, data association and finally data fusion. The functions performed by each of the functional blocks are briefly explained below.

4.2.2 Sensors

Sensors covering a wide range of the energy spectrum have been developed. At the low frequency end, for example, there are acoustic detectors, utilizing the reaction of material elastic properties to incident acoustic waves. The frequency range of the acoustic detectors range from as low as a few Hertz to as high as a few hundred MHz. In the case of electromagnetic detectors, sensors capable of detecting static electric as well as magnetic field intensities have been developed. Eddy current probes, which in practice cover a frequency range of the order of several MHz, are used very widely. At the high frequency end, microwave detectors are used extensively. Progressively higher frequency sensors, leads one to infrared and visible light sensors, commonly used in satellite earth surveillance and x-ray and γ -ray detectors.

Sensors can utilize either an active or passive approach. An active sensor emits energy with the intent of inducing a detectable phenomenon in a target to be observed. Passive sensors observe natural emissions from a target or event.

A generic sensor detects and observes a combination of energy from a target as well environmental energy such as noise, multipath signals, and other interfering signals. The incident energy is detected and an electric signal is generated. As an internal function of the

sensor, the electric signal is often pre-conditioned. This signal conditioning process does not change the information content of the signal; instead it performs operations that facilitate subsequent processing. Examples of signal conditioning functions include frequency shifts, delaying the signal in time, etc.

A second function of internal sensor processing is front end signal processing. The goal here is to select or isolate the energy of interest from all the energy received by the sensor. Signal processing functions may include application of thresholding techniques to detect amplitudes above ground noise, interference canceling or limiting, and frequency band limiting (filtering). The output signal from a sensor may be analog or digital in form. However, for data fusion purposes, eventually all the sensor input signals are converted to digital form.

4.2.3 Data alignment

Data alignment functions transform data received from multiple sensors into a common spatial and temporal reference frame. Specific alignment functions include coordinate transformations, time transformations, and unit conversions.

4.2.4 Data association

A fundamental problem in a multisensor data fusion system is that of data association, or data registration. Data association tackles the problem of sorting or correlating observations from multiple sensors into groups, with each group representing data related to the same distinct entity. Therefore, the associated data set would describe the observed

objects in a coherent way. Association compares the observed data and determines which sections of the observation data belong together to form a group. Further signal processing in the data fusion system is performed based on the associated data.

Specifically, given n observations, y_i from sensor i , how do we relate the data y_i between the sensors?

For homogeneous sensors, the problem is relatively simple. The data from different sensors have the same spatial and temporal reference, as well as the same physical meaning. Data association can be accomplished using, for example, appropriate minimum distance measures. For example, an association matrix can be formed, with each element in the matrix representing a distance measure between two measured data vectors. Then data association can be determined by thresholding the association matrix. If the distance between two data vectors is above a predetermined or an adaptively determined threshold value, then the two observed data are said to be associated, representing the same entity. The choice of distance measure is wide open. For example, some distance measures used for data association are Euclidean distance, Weighted Euclidean distance, City block distance, Minkowski distance, Mahalanobis distance, etc. In addition to using distance as a measure of data association, correlation coefficients are a popular and long-established measure of association. Note that in dynamic situations, the measured data from different sensors could come at different times. In this case, a model prediction scheme has to be used to bring the measured data to the same time base before data association can be performed.

When sensors are of the heterogeneous type, data association takes on a new dimension although the problem can still be simple. For instance, if each sensor produces an output signal in the same data format, such as a two-dimensional image, data association can be performed simply at the pixel level. In other cases, each sensor output may have a distinguishably different data representation and physical meaning. Then data association can be performed based on some kind of data transformation. This dissertation studies the Q-transformation as a tool for associating data between eddy current and ultrasonic NDE signals.

4.2.5 Data fusion algorithms

Data fusion algorithms are highly application dependent. It is virtually impossible to talk about data fusion algorithms without referring to their application. Hall and Llinas [24] surveyed 30 data fusion systems and identified more than 75 algorithms used for data fusion. Those techniques cover a broad set of disciplines, including statistics, signal processing, artificial intelligence, pattern recognition, cognitive psychology, expert systems, and decision theory.

4.2.6 Data fusion system architectures

The transformation of the functional model described in Figure 4.1 into a physical data fusion system requires significant effort and resolution of many issues. First, the problem of algorithm selection depends strongly on the nature of the inferences sought by the data fusion system, the specific application, and the type of sensor data available. After

algorithms have been selected for data fusion, a fundamental issue involves determination of the process for performing fusion. This is closely related to the choice of the architecture of the data fusion system. Heistrand et. al. [41] describes three basic data fusion system architectural approaches: centralized architecture, autonomous architecture and hybrid architecture. The centralized architecture transmits unprocessed data from several sensors to a central fusion process that performs data alignment, association and fusion (classification, in many cases). This is illustrated in Figure 4.2. At the opposite extreme, the autonomous architecture allows each sensor to perform a maximum amount of preprocessing to generate preliminary results before final fusion. This is illustrated in Figure 4.3 using a classification system as an example. The third architecture is a hybrid combination of the centralized and autonomous architectures. The complexity of a hybrid system can be anywhere between a centralized system and an autonomous one.

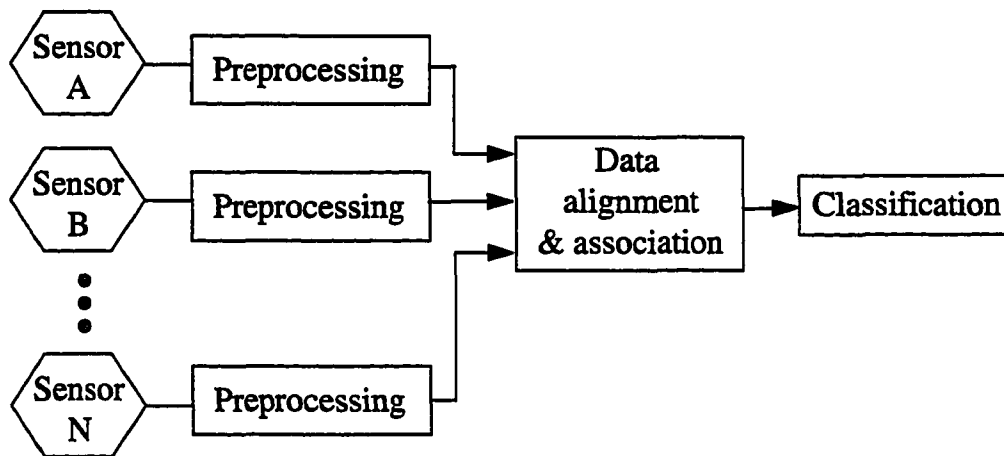


Figure 4.2. Centralized data fusion architecture

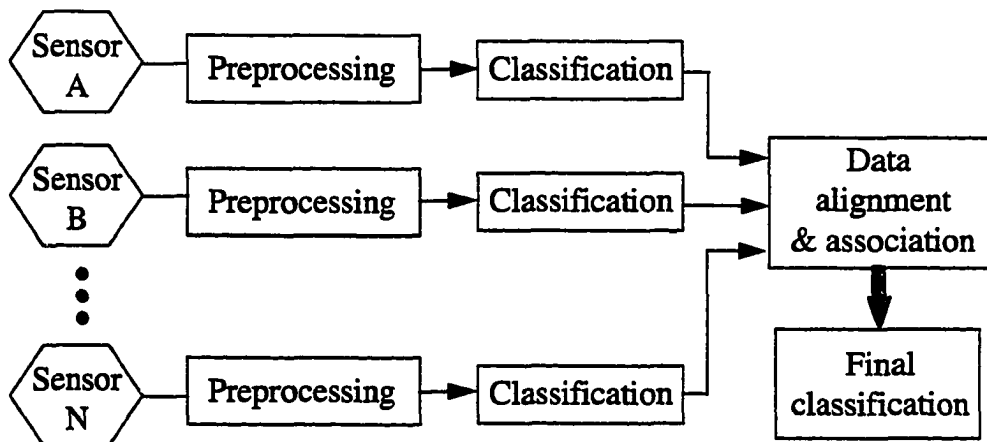


Figure 4.3. Autonomous data fusion architecture

4.2.7 Benefits of data fusion

The primary aim of data fusion is to estimate the system parameters and make higher level inferences that may not be feasible from a single sensor alone. Qualitatively, multisensor data fusion could bring the benefits of improved system operational performance, extended spatial or temporal coverage, increased confidence in estimation or inference, reduced ambiguity, improved probability of detection, enhanced spatial or temporal resolution, improved system reliability, etc.

4.2.8 Classification of data fusion systems

It is possible to roughly classify multisensor data fusion into three categories: (1) the fusion of multiple cues from a single image, (2) the fusion from different sensors with the same modality, and (3) the fusion from multiple modalities [30, 37].

The techniques employed in the first category are highly domain-dependent. An example is the use of modules of shape-from-X schemes to recover surface orientations in computer vision [116].

In the second type of data fusion, the physics in data sensing for all the sensors is the same. Consequently the data from different sensors have comparable formats. The data association can be relatively easily achieved. Therefore, the range of data fusion techniques that can be used is larger. These include methods that handle individual data at the point level to approaches that process at the feature level. Stereo image fusion is one classical example. Using two views with a known geometric relationship, it is possible to extract 3D structure information about the imaged objects, since the variance in the two stereo images are caused solely by the known displacement of the camera [31, 32].

The third type of multisensor data fusion will be the focus of this dissertation. Here, sensors in the fusion system have different modalities. For example, in NDE applications, the same test specimen can be scanned with an eddy current probe and an ultrasonic probe. The underlying physics associated with the two NDE schemes is diffusion and wave scattering, respectively. In this category, Tong *et al.* [33] discuss a target detection technique based on both radar and infrared images. Joshi and Sanderson [39] and Allen [34] report a system that integrates information from visual and tactile sensors to examine object surface in a robotic work cell. Joshi and Sanderson [39] use a minimal representation size criterion for the fusion of visual and tactile data. Visual and tactile sensors are modeled by general constraint equations and observed sensor data populate the space constrained by the model

equations. The data fusion algorithm, which is to estimate the model equation parameters, is based on a minimal representation size criterion which evaluates the complexity through correspondence and encoded errors weighted by relative sensor accuracy and precision. Jain and Hoffman [35] present an expert system for object recognition based on indoor range data. Gil *et al.* [36] use range and intensity data to extract edge maps independently. The two edge maps are then used to generate an integrated edge map. Terzopoulos [40] uses physically-based techniques for visual fusion, where deformable primitives and simulated force fields are modeled by dynamic differential equations to fuse multisensor data over space, time, and scale. Partial, noisy, multisensory data acquired at different spatial positions, at different instants in time, and/or at different scales of resolution are transformed into nonlinear force fields. The deformable primitives represent free-form curves, surfaces, and solids. The deformable primitives move and change shape in response to simulated forces and environmental constraints as if there were made of nonrigid materials such as rubber. In NDE applications, Yim *et al* [72, 73, 74, 86] apply a variety of nonphenomenological processing techniques to fuse the eddy current and ultrasonic data. In [72] and [73] radial basis function (RBF) and multilayer perceptron (MLP) neural networks are used for fusing eddy current and ultrasonic NDE data at the pixel level, as well as for the fusion of multifrequency eddy current images. The training of the neural networks involves the establishment of the relation between desired output and its corresponding inputs. In [86] an optimal image fusion approach is presented. The algorithm uses a linear minimum mean square error (LMMSE) filter to fuse multiple images, based on individual image noise

characteristics. [74] presents an image fusion algorithm using multi-resolution decomposition techniques for combining ultrasonic and eddy current images. Input images are decomposed into several subbands, each occupying a spectral band. Image statistics are estimated in each subband and LMMSE based fusion is performed using the subband image statistics.

4.3 Data Fusion Applications

Research in the field of data fusion had its initial thrust from defense applications, where the task for data processing has always been demanding. The increasing sophistication of data acquisition techniques have contributed to the application of data fusion techniques to a wider class of nonmilitary problems. New areas of application include law enforcement, remote sensing, automated monitoring of equipment, medical diagnosis and robotics.

Law enforcement applications, including trace amount explosive detection and drug interdiction, are similar to military intelligence and surveillance. For example, drug interdiction may involve patrol of a border to identify and locate drug shipments. As drug criminals become more sophisticated, the range of sensors and processing required for data fusion has become more extensive.

Remote sensing applications include the surveillance of the earth to identify and monitor crops, weather patterns, mineral resources, and environmental conditions. Special examples of remote sensing are NASA's use of Landsat satellites to monitor the earth's surface and space probes to investigate the planets and the solar system. The Hubble Space

Telescope employs passive sensors, such as visible and infrared cameras, to obtain input images covering different spectral regions to be used for data fusion.

Data fusion systems have also been developed for robotic applications. Industrial robots use pattern recognition and inference techniques to recognize three-dimensional objects, determine their orientation, and guide robotic appendages to manipulate the objects.

Data fusion applications made their way to the vision community, via the robotics community [38]. In the early 1980's, Herman and Kanade [26] combined passive stereo imagery from an aerial sensor. This early work characterized the problem as one of using incremental combination of geometric information. Smith and Cheeseman [27] argued for the use of Bayesian estimation theory in vision and robotics. An optimal combination function was derived and shown to be equivalent to a simple form of Kalman filter. Using estimation theory, Faugeras and Ayache [28] contributed an adaptation of this theory to solve problems in stereo vision.

Estimation theory techniques can be applied to combine numerical parameters. In the area of symbolic information processing, computational mechanisms employing symbolic inference techniques draw from such areas as artificial intelligence. In addition to brute force coding of inference procedures, rule based "inference engines" are used widely. Such inference may include the use of backward chaining procedure for solving diagnostic problems, consultation, or accessing data bases as in the case of Prolog [29].

A final example of fusion systems involves monitoring and control of industrial equipment and manufacturing processes. Certain systems, such as nuclear power plants and

modern aircraft, require complex monitoring procedures to ensure proper operation. Data from multiple sensors are monitored to assess the health of a system and to optimize its performance.

4.4 Data Fusion for NDE Applications

As a natural extension of data fusion applications to industrial systems monitoring, we investigate the application of data fusion to the area of nondestructive evaluation in this dissertation.

Potential benefits of data fusion include more accurate characterization and often an ability to observe features that are otherwise difficult to perceive with a single sensor. The benefits are closely connected to the notion of redundant and complementary information. We witness redundancy in information when sensors observe the same features from the test specimen. The fusion of such overlapping data improves the signal-to-noise ratio and contributes directly to enhancing the characterization accuracy. In contrast, the fusion of complementary information allows features in the specimen to be observed that would otherwise not be seen. If the features observed are from different dimensions, the information provided by each sensor constitutes a subset of the features forming the subspace in the feature space. In this case, one of the greatest challenges is the task of registration since the features derived from each complementary sensor are from different dimensions.

Very often, various sensors are employed in NDE applications to meet the challenge. These sensors may employ fundamentally different physical principles. Eddy current and ultrasonic imaging techniques can be used together to quantitatively assess the serviceability

of a sample. In this case, the sensors are inhomogeneous, covering different energy spectra and energy types. This investigation is an initial attempt to address issues in fusing eddy current and ultrasonic data, to obtain better characterization of the specimen under test.

Each NDE method offers its own set of advantages and disadvantages. Eddy current techniques are relatively insensitive to surface roughness conditions. This technique offers excellent sensitivity to surface breaking defects with relatively high signal-to-noise ratio. However, eddy current imaging techniques provide poor resolution. The support of flaw signal is at least equal to the combination of the size of the excitation and pickup coils. Another disadvantage of eddy current NDE is its inability to detect and characterize subsurface structures, due to the rapid decay of energy with increasing depth. On the other hand, ultrasonic imaging techniques offer excellent image resolution. It also offers excellent ability to detect surface as well as subsurface structures, since the energy loss in solid materials is linear with respect to penetration depth, instead of the exponential rate as in the eddy current case. However, the method is subject to the influence of a wide variety of measurement conditions, such as surface roughness and coupling. Data interpretation becomes extremely challenging due to such artifacts as multiple reflections generated by media boundaries and diffraction caused by microstructure boundaries. As a result, the method produces images with relatively low signal-to-noise ratio. It is, therefore, desirable to investigate a data fusion technique that combines the advantages of the two methods.

Data fusion algorithms can be broadly classified as either phenomenological or nonphenomenological. Phenomenological approaches utilize a knowledge of the underlying

physical processes as a basis for deriving the procedure for fusing data [75]. Non-phenomenological approaches, in contrast, tend to ignore the underlying physical process and attempt to fuse information using the statistics or some other properties associated with individual segments of data [72, 73, 74].

Non-phenomenological data fusion methods can be roughly classified into four different categories: signal level fusion, pixel level fusion, feature level fusion, and symbol level fusion. Signal level fusion methods can be applied when the sensors have identical or similar characteristics, or when the relationship between the signals from different sensors is explicitly known. Pixel level fusion methods can be applied when sensors are used to generate output image data in the same format. The statistical characteristics of the images combined with information concerning the relation between the sensors is used to develop the fusion strategy. Feature level fusion implies the fusion of a reduced set of data representing the signal, called features. The data features are an abstraction of the raw data intended to provide a reduced set that represents the original data accurately and concisely. Symbol level fusion represents the highest abstract level of fusion. Such techniques call for extracting abstract elements of information called symbols. The different set of symbols are manipulated using reasoning as a basis to generate better information.

The objective of this research is to develop methodologies for combining information from the eddy current diffusion signals and ultrasonic wave signals. More specifically, the research investigates data transformation techniques for registering ultrasonic signals with eddy current flaw signals to obtain composite images in the same domain. We proposed the

use of the Q-transform to accomplish this. This data registration approach is essentially phenomenological, since the transformation is based on treating eddy current NDE as a diffusion process and ultrasonic scattering as a wave process. After the data registration process is completed, the eddy current signals and the Q-transformed ultrasonic signals are in the same domain. This allows data from two different methods to be combined and presumably leading to better signal-to-noise ratio and hence contribute to superior defect characterization.

CHAPTER V. DATA FUSION USING Q-TRANSFORMATION

This chapter explores the use of the Q-transform as a basis for relating a diffusion signal with the corresponding wave signal [77, 78]. The technique is employed to combine an eddy current diffusion signal and an ultrasound wave signal. Specifically, ultrasonic signals are Q-transformed to the diffusion domain. The transformation allows the superposition of the transformed field on the eddy current field. It is anticipated that the resulting field will have a higher signal-to-noise ratio. The data registration scheme is illustrated in Figure 5.1.

Before we proceed to discuss the issue of registering eddy current and ultrasonic signals further, a brief review of the Q-transform and its properties are presented.

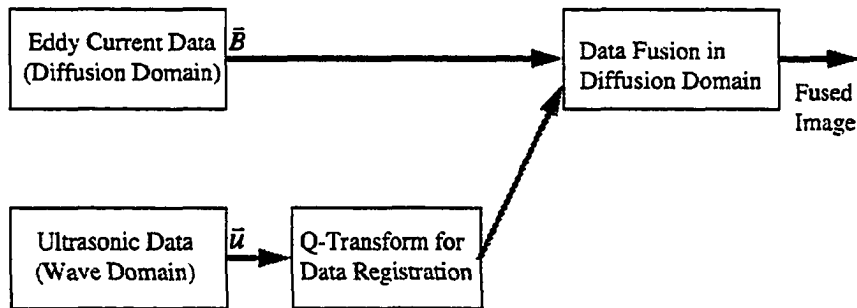


Figure 5.1 Eddy current and ultrasonic data registration approach using Q-transform

5.1 Introduction to Q-Transformation

Consider two differential equations. The first equation describes a general diffusion process.

$$\nabla \times \nabla \times \vec{E} + a^2 \frac{\partial \vec{E}}{\partial t} = \vec{S}(\vec{r}, t) \quad (5.1)$$

where \vec{E} is the electrical field and $a^2 = \mu\sigma$. A similar expression can be derived if the electric field is replaced by the magnetic field density or magnetic vector potential. When applied to the eddy current process, $\vec{S}(\vec{r}, t)$ represents a driving source, i.e.,

$$\vec{S}(\vec{r}, t) = -\mu \frac{\partial \vec{J}(\vec{r}, t)}{\partial t}, \text{ where } \vec{J}(\vec{r}, t) \text{ is the free electrical current.}$$

The initial and boundary conditions can be specified generally as:

$$\begin{aligned} \vec{E}(\vec{r}, 0) &= \vec{E}_0 \\ \vec{E}(\vec{r}_b, t) &= \vec{E}_T \end{aligned} \quad (5.2)$$

We now introduce a general wave equation:

$$\nabla \times \nabla \times \vec{U}(\vec{r}, q) + a^2 \frac{\partial^2 \vec{U}(\vec{r}, q)}{\partial q^2} = \vec{F}(\vec{r}, q) \quad (5.3)$$

In ultrasound, $\vec{U}(\vec{r}, q)$ corresponds to elastic displacement and q corresponds to time.

a is related to the ultrasound wave velocity v , $a = 1/v$. For now, we assume that the a

coefficients for the two processes are the same. The initial condition is $\vec{U}(\vec{r}, 0) = \vec{U}_I$. The

boundary condition imposed may be either of the first, second, or third type. Here, we impose the first type of boundary condition, $\bar{U}(\bar{r}_b, q) = \bar{U}_\Gamma$.

The relation between the diffusion equation and the wave equation is determined by comparing the two equations in the Laplace transform domain.

$$\nabla \times \nabla \times \hat{E}(\bar{r}, s) + a^2[s\hat{E}(\bar{r}, s) - \bar{E}(\bar{r}, 0)] = \hat{S}(\bar{r}, s) \quad (5.4)$$

with $\hat{E}(\bar{r}_b, s) = \hat{E}_\Gamma$

and

$$\nabla \times \nabla \times \hat{U}(\bar{r}, p) + a^2[p^2\hat{U}(\bar{r}, p) - p\bar{U}(\bar{r}, 0) - \frac{\partial}{\partial q}\bar{U}(\bar{r}, 0)] = \hat{F}(\bar{r}, p) \quad (5.5)$$

with $\hat{U}(\bar{r}_b, p) = \hat{U}_\Gamma$

Let $s = p^2$ in the transformed diffusion equation. Then,

$$\nabla \times \nabla \times \hat{E}(\bar{r}, p^2) + a^2[p^2\hat{E}(\bar{r}, p^2) - \bar{E}(\bar{r}, 0)] = \hat{S}(\bar{r}, p^2) \quad (5.6)$$

Comparing this equation with the one for $\hat{U}(\bar{r}, p)$, we see that $\hat{E}(\bar{r}, p^2)$ and $\hat{U}(\bar{r}, p)$ will be equal when the following conditions are satisfied.

$$\bar{U}(\bar{r}, 0) = 0 \quad (5.7)$$

$$\bar{E}(\bar{r}, 0) = \frac{\partial}{\partial q}\bar{U}(\bar{r}, 0) \quad (5.8)$$

$$\widehat{E}(\bar{r}_b, p^2) = \widehat{U}(\bar{r}_b, p) \quad (5.9)$$

$$\text{and } \widehat{S}(\bar{r}, p^2) = \widehat{F}(\bar{r}, p) \quad (5.10)$$

In other words, when the above relations for the initial and boundary conditions as well for the sources are met, the diffusion field $\bar{E}(\bar{r}, t)$ and wave field $\bar{U}(\bar{r}, q)$ are related to each other by the following equation in the s -domain.

$$\widehat{E}(\bar{r}, p^2) = \widehat{U}(\bar{r}, p) \quad (5.11)$$

That is,

$$\int_0^\infty \bar{E}(t) e^{-p^2 t} dt = \int_0^\infty \bar{U}(q) e^{-pq} dq \quad (5.12)$$

We see that the above relation is to be applied to both the source terms and the boundary conditions. The initial conditions need to be satisfied in a different manner. The initial value of the wave equation is to be zero while the initial velocity of the wave equation must equal to the initial value of the diffusion equation.

5.1.1 Q-Transform from wave to diffusion domain

The above relationship between $\widehat{E}(\bar{r}, p^2)$ and $\widehat{U}(\bar{r}, p)$ in the s -domain can be used to derive the relation between $\bar{E}(\bar{r}, t)$ and $\bar{U}(\bar{r}, q)$ in the time domain. Let $s = p^2$. Then

$$\int_0^\infty \bar{E}(t) e^{-st} dt = \int_0^\infty \bar{U}(q) e^{-\sqrt{s}q} dq \quad (5.13)$$

Taking the inverse Laplace transform of both sides, the Q-transform which maps a wave field to its corresponding diffusion field is derived.

$$\bar{E}(t) = \frac{1}{2\sqrt{\pi t^3}} \int_0^{\infty} q e^{-q^2/4t} \bar{U}(q) dq \quad (5.14)$$

In our application, only one field component is studied for both the diffusion and the wave field. Therefore, the above equation can be written in scalar form,

$$E(t) = \frac{1}{2\sqrt{\pi t^3}} \int_0^{\infty} q e^{-q^2/4t} U(q) dq \quad (5.15)$$

This Q-transform relationship allows the mapping of a wave signal to a diffusion signal. The transformation is numerically stable because of the highly damped nature of the kernel. We will investigate the use of this transform to fuse ultrasound and eddy current images based on this relation.

5.1.2 Inverse Q-transform from diffusion to wave domain

The inverse Q-transform which allows a diffusion signal to be transformed to its corresponding wave signal, can be derived in a similar manner. Performing an inverse s-transform over p , the following relation is obtained

$$U(q) = \frac{1}{2\pi j} \int_{\sigma-j\infty}^{\sigma+j\infty} dp e^{pq} \int_0^{\infty} E(t) e^{-p^2 t} dt \quad (5.16)$$

where σ is sufficiently large enough for $U(q)$ to converge.

Given a diffusion signal, the inverse Q-transform allows the corresponding wave signal, with matching initial and boundary conditions, as well as matching driving forces, to be synthesized.

Note that the inverse Q-transform is numerically unstable. The integration of p is along a line parallel to the imaginary axis. Thus the term in the integration kernel, $e^{-p^2 t}$, grows indefinitely as p moves along the integration path. Any noise in $E(t)$ can make the integration result deviate greatly. For this reason, we have confined our attenuation to using the forward Q-transform only.

5.2 Properties of Q-Transforms

5.2.1 Q-transform of the Green's functions

As Green's functions play a key role in the understanding of both the diffusion and wave processes, the Q-transform is first applied to the Green's function associated with the wave equation to investigate its behavior. The following derivation will show that, in a homogeneous medium, the Green's functions for wave propagation and the Green's functions for diffusion satisfy the Q-transform mapping for one-, two- and three-dimensional cases.

5.2.1.1 Q-transform of the Green's function of the one-dimensional wave equation The Green's function $g_w(x, t)$ for the one-dimensional wave propagation equation satisfies the following equation:

$$\begin{cases} \frac{\partial^2}{\partial x^2} g_w(x, t) - a^2 \frac{\partial^2}{\partial t^2} g_w(x, t) = 4\pi\delta(x)\delta(t) \\ g_w(x, 0) = 0 \\ \frac{\partial}{\partial t} g_w(x, t)|_{t=0} = 0 \end{cases} \quad (5.17)$$

Or equivalently,

$$\begin{cases} \frac{\partial^2}{\partial x^2} g_w(x, t) - a^2 \frac{\partial^2}{\partial t^2} g_w(x, t) = 0 \\ g_w(x, 0) = 0 \\ \frac{\partial}{\partial t} g_w(x, t)|_{t=0} = 4\pi\delta(x) \end{cases} \quad (5.18)$$

The general form of the solution for $\frac{\partial^2}{\partial x^2} g_w(x, t) - a^2 \frac{\partial^2}{\partial t^2} g_w(x, t) = 0$ is

$$\begin{aligned} g_w(x, t) &= g_1(ax - t) + g_2(ax + t) \\ &= \int_{-\infty}^{\infty} A_1(k) e^{jk(ax-t)} dk + \int_{-\infty}^{\infty} A_2(k) e^{jk(ax+t)} dk \end{aligned} \quad (5.19)$$

Now, let us apply the initial conditions to determine the coefficients $A_1(k)$ and $A_2(k)$.

$$\begin{cases} g_w(x, 0) = \int_{-\infty}^{\infty} (A_1(k) + A_2(k)) e^{jk(ax)} dk = 0 \\ \frac{\partial}{\partial t} g_w(x, t)|_{t=0} = \int_{-\infty}^{\infty} (-jkA_1(k) + jkA_2(k)) e^{jk(ax)} dk = 4\pi\delta(x) = 2 \int_{-\infty}^{\infty} e^{jk(ax)} dk \end{cases} \quad (5.20)$$

That is,

$$\begin{cases} A_1(k) + A_2(k) = 0 \\ A_1(k) - A_2(k) = -\frac{2}{jk} \end{cases} \quad (5.21)$$

We get $A_1(k) = -\frac{1}{jk}$ and $A_2(k) = \frac{1}{jk}$.

Therefore, the Green's function is

$$\begin{aligned}
 g_w(x,t) &= \int_{-\infty}^{\infty} A_1(k) e^{jk(ax-t)} dk + \int_{-\infty}^{\infty} A_2(k) e^{jk(ax+t)} dk \\
 &= -\int_{-\infty}^{\infty} \frac{1}{jk} e^{jk(ax-t)} dk + \int_{-\infty}^{\infty} \frac{1}{jk} e^{jk(ax+t)} dk \\
 &= -\frac{1}{a} \int_{-\infty}^{\infty} \left[\int_{-\infty}^x e^{jk(ax'-t)} dx' \right] dk + \frac{1}{a} \int_{-\infty}^{\infty} \left[\int_{-\infty}^x e^{jk(ax'+t)} dx' \right] dk \\
 &= -\frac{1}{a} \int_{-\infty}^x \left[\int_{-\infty}^{\infty} e^{jk(ax'-t)} dk \right] dx' + \frac{1}{a} \int_{-\infty}^x \left[\int_{-\infty}^{\infty} e^{jk(ax'+t)} dk \right] dx' \quad (5.22) \\
 &= -\frac{1}{a} \int_{-\infty}^x [2\pi\delta(ax'-t)] dx' + \frac{1}{a} \int_{-\infty}^x [2\pi\delta(ax'+t)] dx' \\
 &= -4\pi \frac{1}{2a} \begin{cases} 1, & ax > t \\ 0, & ax < t \end{cases} + 4\pi \frac{1}{2a} \begin{cases} 1, & ax > -t \\ 0, & ax < -t \end{cases} \\
 &= 4\pi \frac{1}{2a} \begin{cases} 1, & |ax| \leq t \\ 0, & |ax| > t \end{cases}
 \end{aligned}$$

Applying the forward Q-transform to the one-dimensional wave propagation kernel,

we obtain:

$$\begin{aligned}
 E(x,t) &= \frac{1}{2\sqrt{\pi a^3}} \int_0^{\infty} q e^{-q^2/4t} g_w(x,q) dq \\
 &= \frac{1}{2\sqrt{\pi a^3}} \int_{ax}^{\infty} q e^{-q^2/4t} 4\pi \frac{1}{2a} dq \\
 \xrightarrow{q^2=y} & \frac{1}{2\sqrt{\pi a^3}} 4\pi \frac{1}{4a} \int_{(ax)^2}^{\infty} e^{-y/4t} dy \quad (5.23) \\
 &= \frac{1}{2\sqrt{\pi a^3}} 4\pi \frac{1}{4a} \cdot 4t \cdot e^{-a^2 x^2/4t} \\
 &= 4\pi \frac{1}{2\sqrt{\pi a}} \frac{1}{a} \cdot e^{-a^2 x^2/4t}
 \end{aligned}$$

$E(t)$, the Q-transformed signal in the diffusion domain is exactly the Green's function for the one-dimensional diffusion equation.

5.2.1.2 Q-transform of the Green's function of the two-dimensional wave

equation In a homogeneous two-dimensional space, the Green's function for a wave equation satisfies:

$$\begin{cases} \left(\frac{\partial^2}{\partial x^2} + \frac{\partial^2}{\partial y^2} \right) g_w(R, t) - a^2 \frac{\partial^2}{\partial t^2} g_w(R, t) = 4\pi\delta(R)\delta(t) \\ g_w(x, y, 0) = 0 \\ \frac{\partial}{\partial t} g_w(x, y, t)|_{t=0} = 0 \end{cases} \quad (5.24)$$

where, $R = \sqrt{x^2 + y^2}$. If the media is homogenous, the Green's function is a function of R , and is independent of orientation. The derivation for $g_w(R, t)$ is readily available [42]. The solution is:

$$g_w(R, t) = \begin{cases} \frac{2}{\sqrt{t^2 - a^2 R^2}}, & aR < t \\ 0, & aR > t \end{cases} \quad (5.25)$$

Computing the Q-transform of the wave Green's function, we obtain

$$\begin{aligned}
E(R, t) &= \frac{1}{2\sqrt{\pi t^3}} \int_0^\infty q e^{-q^2/4t} g_w(R, q) dq \\
&= \frac{1}{2\sqrt{\pi t^3}} \int_{aR}^\infty q e^{-q^2/4t} \frac{2}{\sqrt{q^2 - a^2 R^2}} dq \\
&\xrightarrow{q^2 - a^2 R^2 = y^2} \frac{2}{2\sqrt{\pi t^3}} \int_0^\infty e^{-(y^2 + a^2 R^2)/4t} dy \\
&= \frac{1}{\sqrt{\pi t^3}} \cdot e^{-a^2 R^2/4t} \cdot \int_0^\infty e^{-y^2/4t} dy \\
&= \frac{1}{\sqrt{\pi t^3}} \cdot e^{-a^2 R^2/4t} \cdot \frac{\sqrt{\pi}}{2\sqrt{1/4t}} \\
&= \frac{1}{t} e^{-a^2 R^2/4t}
\end{aligned} \tag{5.26}$$

$E(R, t)$ is exactly the same as the two-dimensional Green's function for the diffusion equation, $g_d(R, \tau) = \frac{1}{\tau} e^{-a^2 R^2/4\tau}$.

5.2.1.3 Q-transform of the Green's function of the three-dimensional wave

equation The Green's function, $g_w(R, t)$, for a three-dimensional differential wave equation, satisfies:

$$\begin{cases}
\left(\frac{\partial^2}{\partial x^2} + \frac{\partial^2}{\partial y^2} + \frac{\partial^2}{\partial z^2} \right) g_w(R, t) - a^2 \frac{\partial^2}{\partial t^2} g_w(R, t) = 4\pi \delta(R) \delta(t) \\
g_w(x, y, z, 0) = 0 \\
\frac{\partial}{\partial t} g_w(x, y, z, t)|_{t=0} = 0
\end{cases} \tag{5.27}$$

where, $R = \sqrt{x^2 + y^2 + z^2}$. The solution for $g_w(R, t)$ is:

$$g_w(R, t) = \frac{1}{R} \delta(aR - t) \quad (5.28)$$

The Q-transform of $g_w(R, t)$ is:

$$\begin{aligned} E(R, t) &= \frac{1}{2\sqrt{\pi t^3}} \int_0^\infty q e^{-q^2/4t} g_w(R, q) dq \\ &= \frac{1}{2\sqrt{\pi t^3}} \int_0^\infty q e^{-q^2/4t} \cdot \frac{1}{R} \delta(aR - q) dq \\ &= \frac{1}{2\sqrt{\pi t^3}} a \operatorname{Re}^{-a^2 R^2/4t} \cdot \frac{1}{R} \\ &= \frac{a}{2\sqrt{\pi t^3}} e^{-a^2 R^2/4t} \end{aligned} \quad (5.29)$$

Again, $E(R, t)$ is exactly the same as the three-dimensional Green's function for diffusion in a homogeneous media, $g_d(R, \tau) = \frac{a}{2\sqrt{\pi \tau^3}} e^{-a^2 R^2/4\tau}$.

In summary, the one-dimensional, two-dimensional and three-dimensional Green's functions for the wave process and the diffusion process all satisfy the Q-transformation mapping. The Q-transform is performed purely between q in the wave domain and the time t in the diffusion domain. No operation is performed on the spatial coordinates. Therefore, the Q-transformation relates a wave field with a diffusion field regardless of the dimensionality of the problem. The verification of this property paves the way for additional investigation into using Q-transforms for the registration of wave and diffusion based images.

5.2.2 Q-Transform when the forcing function is a Dirac delta function

When the forcing function in the wave equation is a Dirac delta function, the transformed forcing function in the diffusion equation should also be a delta function. Indeed, this is a prerequisite for the Q-transform to be applied. We verify this property as follows. Let $U(q) = \delta(q)$. Then

$$\begin{aligned}
 E(t) &= \frac{1}{2\sqrt{\pi t^3}} \int_0^\infty q e^{-q^2/4t} U(q) dq \\
 &= \frac{1}{2\sqrt{\pi t^3}} \int_0^\infty q e^{-q^2/4t} \delta(q) dq \\
 &\xrightarrow{q_0 \rightarrow 0} \frac{1}{2\sqrt{\pi t^3}} q_0 e^{-q_0^2/4t}
 \end{aligned} \tag{5.30}$$

We see that $E(t)$ is zero when t is nonzero. When t approaches zero, let $t = q_0 = \varepsilon$, then

$$\begin{aligned}
 E(t) &\xrightarrow{q_0 \rightarrow 0, t \rightarrow 0} \frac{1}{2\sqrt{\pi t^3}} q_0 e^{-q_0^2/4t} \\
 &\xrightarrow{\varepsilon \rightarrow 0} \frac{1}{2\sqrt{\pi \varepsilon}} e^{-\varepsilon/4}
 \end{aligned} \tag{5.31}$$

Clearly $E(t)$ approaches infinity. Furthermore, the integration of $E(t)$ over t is one. In another words, the transformed $E(t)$ is a delta function $\delta(t)$. Therefore, the Q-transform of $U(q) = \delta(q)$ in the wave domain is indeed a delta function, i.e., $E(t) = \delta(t)$, in the diffusion domain.

The above two properties of the Q-transform, one relating to the Green's functions, and the other to delta functions, implies that convolution operation can be applied to the Q-transform.

5.2.3 Time shifting in Q-transform

The Q-transform is a time varying operator, unlike most commonly used linear system operators. Our investigation of the Q-transform time shift property is presented as follows.

Consider a wave signal $U_1(q)$, which is zero for nonpositive q values, and let the corresponding diffusion signal be $E_1(t)$. That is, there exists the following relation between $U_1(q)$ and $E_1(t)$:

$$E_1(t) = \frac{1}{2\sqrt{\pi t^3}} \int_0^{\infty} q e^{-q^2/t^4} U_1(q) dq \quad (5.32)$$

Now, given another time delayed version of signal $U_1(q)$, $U_2(q) = U_1(q - q_0)$, as shown in Figure 5.2, we wish to determine the Q-transformed signal $E_2(t)$ in the diffusion domain and establish the relationship between $E_2(t)$ and $E_1(t)$?

Let the Laplace transforms of $E_1(t)$ and $U_1(q)$ be $E_1(s)$ and $U_1(p)$, respectively.

Then,

$$E_1(p^2) = U_1(p) \quad (5.33)$$

The Laplace transform of $U_2(q)$, $U_2(p)$, is

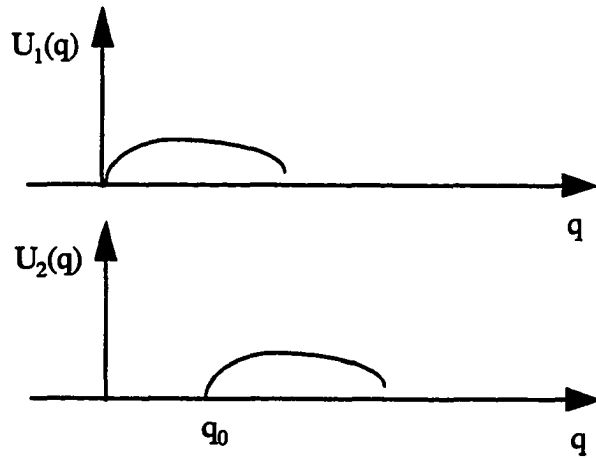


Figure 5.2. Time shifted signal $U_2(q)$ vs. the original signal $U_1(q)$

$$U_2(p) = e^{-q_0 p} U_1(p) \quad (5.34)$$

Using $p = \sqrt{s}$, the Laplace transform of $E_2(t)$ is:

$$E_2(s) = e^{-q_0 \sqrt{s}} U_1(\sqrt{s}) \quad (5.35)$$

We see that $E_2(s)$ is the product of two factors: $H(s) = e^{-q_0 \sqrt{s}}$ and $U_1(\sqrt{s})$. $U_1(\sqrt{s})$ corresponds to $E_1(t)$ in the time domain. It is easy to verify that the time domain signal $h(t)$, whose Laplace transform is $H(s)$, has the following expression:

$$h(t) = \frac{q_0}{2\sqrt{\pi}} e^{-q_0^2/4t} \quad (5.36)$$

$E_2(t)$ is the convolution of $h(t)$ and $E_1(t)$:

$$\begin{aligned}
 E_2(t) &= h(t) * E_1(t) \\
 &= \int_0^t E_1(\tau) h(t-\tau) d\tau \\
 &= \int_0^t E_1(\tau) \frac{q_0}{2\sqrt{\pi}} e^{-q_0^2/4(t-\tau)} d\tau
 \end{aligned} \tag{5.37}$$

We see that the effect of time shifting in the wave domain is to smear the signal in the diffusion domain. The smearing kernel $h(t)$ is plotted in Figure 5.3. The larger the shift in q , the stronger the smearing effect on the diffusion signal. The time varying nature of the transform can also be surmised from the fact that q has units of square root of time. This time varying property is undesirable. As will be seen later, the convolution effect makes the time alignment in the wave domain highly sensitive. A small amount of signal shift in the wave domain can lead to a significant change in the overall shape of the diffusion signal.

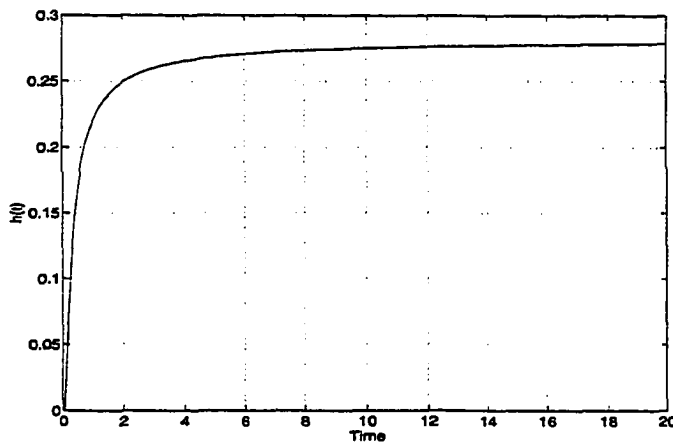


Figure 5.3. Smearing kernel $h(t)$

5.3 Q-Transformation in NDE Applications

Note that the previously derived Q-transform holds true only if the a coefficients in the two equations are equal. We recall that the two Green's functions $g_d(x,t)$ and $g_w(x,t)$ satisfying the following equations.

$$\begin{cases} \frac{\partial^2}{\partial x^2} g_d(x,t) - a^2 \frac{\partial}{\partial t} g_d(x,t) = 4\pi\delta(x)\delta(t) \\ \frac{\partial^2}{\partial x^2} g_w(x,t) - a^2 \frac{\partial^2}{\partial t^2} g_w(x,t) = 4\pi\delta(x)\delta(t) \end{cases} \quad (5.38)$$

However, the assumption of equal coefficient values is violated in the desired NDE application. The coefficient in the eddy current equation, let us call it a_1 , is related to the test specimen properties, i.e., $a_1 = \sqrt{\mu\sigma}$. The coefficient in the ultrasonic wave equation, labeled as a_2 , is related to the ultrasonic wave velocity v by $a_2 = 1/v$. If a copper slab is employed as the test specimen with $\sigma = 5.77e7$ in the eddy current setup, and assuming the ultrasound velocity to be $v=6.3 \times 10^3$ m/s, we find that the coefficient ratio is $a_1/a_2 = 5.4e4$. This deviates greatly from the nominal ratio of one for which the Q-transform results were derived. For this reason, a modified Q-transformation formula for mapping the diffusion signal has to be derived.

5.3.1 Q-transform between diffusion and wave signals with different a coefficients

The modified Q-transform will be derived for the following pair of equations. As noted earlier, the Q-transform links the variables t and q , and is independent of spatial

variables x , y and z . The derivation is based on a one-dimensional model. The result can be applied with equal validity to cases involving higher dimensions.

$$\begin{cases} \frac{\partial^2}{\partial x^2} g_d(x, t) - a_1^2 \frac{\partial}{\partial t} g_d(x, t) = 4\pi\delta(x)\delta(t) \\ \frac{\partial^2}{\partial x^2} g_w(x, t) - a_2^2 \frac{\partial^2}{\partial t^2} g_w(x, t) = 4\pi\delta(x)\delta(t) \end{cases} \quad (5.39)$$

The approach involves transforming one of the equations (we chose the second one) such that the transformed equation has the same coefficient as the other equation.

In the second equation, let us define

$$t = (a_2/a_1)y \quad (5.40)$$

The transformed equation is

$$\begin{aligned} \frac{\partial^2}{\partial x^2} g_w(x, y) - a_1^2 \frac{\partial^2}{\partial y^2} g_w(x, y) &= 4\pi\delta(x)\delta\left(\frac{a_2}{a_1}y\right) \\ &= 4\pi \frac{a_1}{a_2} \delta(x)\delta(y) \end{aligned} \quad (5.41)$$

We note the scaling factor of a_1/a_2 on the right hand side of the equation. Therefore the forward Q-transform in terms of y is

$$E(t) = \frac{1}{2\sqrt{\pi t^3}} \frac{a_2}{a_1} \int_0^\infty y e^{-y^2/4t} U(y) dy \quad (5.42)$$

Writing the transformation in terms of time q , and employing the relation

$y = (a_1/a_2)q$, we obtain

$$\begin{aligned}
E(t) &= \frac{1}{2\sqrt{\pi t^3}} \frac{a_2}{a_1} \int_0^\infty \left(\frac{a_1}{a_2} q\right) e^{-\frac{(a_1 q)^2}{4t}} U(q) d\left(\frac{a_1}{a_2} q\right) \\
&= \frac{1}{2\sqrt{\pi t^3}} \int_0^\infty \left(\frac{a_1}{a_2} q\right) e^{-\frac{(a_1 q)^2}{4t}} U(q) dq
\end{aligned} \tag{5.43}$$

The same result can also be obtained by operating in the Laplace domain. We see that, when the a coefficients are different in the differential equations, the q variable in the integrand is to be normalized by replacing it with $(a_1/a_2)q$.

5.3.2 Q-Transform of the Green's functions

The Green's functions can still be mapped by the modified Q-transform for different spatial dimensions. This is easy to verify and will not be presented here. The results are summarized below:

In one dimension cases,

$$g_w(x,t) = 4\pi \frac{1}{2a_2} \begin{cases} 1, & |a_2 x| \leq t \\ 0, & |a_2 x| > t \end{cases} \tag{5.44}$$

$$g_d(x,t) = 4\pi \frac{1}{2\sqrt{\pi t}} \frac{1}{a_1} \cdot e^{-a_2^2 x^2 / 4t} \tag{5.45}$$

In the two dimensional case,

$$g_w(R,t) = \begin{cases} \frac{2}{\sqrt{t^2 - a_2^2 R^2}}, & a_2 R < t \\ 0, & a_2 R > t \end{cases} \tag{5.46}$$

$$g_d(R, t) = \frac{1}{t} e^{-a^2 R^2 / 4t} \quad (5.47)$$

with $R = \sqrt{x^2 + y^2}$.

In the three dimensional case,

$$g_w(R, t) = \frac{1}{R} \delta(a_2 R - t) \quad (5.48)$$

$$g_d(R, t) = \frac{a}{2\sqrt{\pi^3}} e^{-a^2 R^2 / 4t} \quad (5.49)$$

with $R = \sqrt{x^2 + y^2 + z^2}$.

5.3.3 Time shift property of the modified Q-transform

The effect of time shift has been studied earlier for the case where the coefficients are equal. The Q-transform of the delayed version of the signal, $U_2(q) = U_1(q - q_0)$, $E_2(t)$ is related to the signal $E_1(t)$ by:

$$E_2(t) = h(t) * E_1(t) \quad (5.50)$$

where, $h(t) = \frac{q_0}{2\sqrt{\pi}} e^{-q_0^2 / 4t}$.

Now, the a coefficients are different. Taking the Laplace transforms of the two differential equations, we obtain

$$\nabla \times \nabla \times E(s) + a_1^2 s E(s) = S(s) \quad (5.51)$$

$$\nabla \times \nabla \times U(p) + a_2^2 p^2 U(p) = F(p) \quad (5.52)$$

Substituting $s = \frac{a_2^2}{a_1^2} p^2$, after transforming we obtain

$$E\left(\frac{a_2^2}{a_1^2} p^2\right) = U(p), \quad (5.53)$$

or equivalently

$$E(s) = U\left(\frac{a_1}{a_2} \sqrt{s}\right). \quad (5.54)$$

For a delayed version of signal in the wave domain, $U_2(q) = U(q - q_0)$, the corresponding Laplace transform is:

$$U_2(p) = e^{-q_0 p} U(p) \quad (5.55)$$

Therefore, the Q-transformed signal $E_2(t)$ has the following form in the Laplace domain:

$$E_2(s) = e^{-\frac{a_1}{a_2} q_0 \sqrt{s}} U_1\left(\frac{a_1}{a_2} \sqrt{s}\right). \quad (5.56)$$

The time domain signal $E_2(t)$, is obtained by convolving the two signals: $h(t)$ and

$$E(t), \text{ with } h(t) = \frac{1}{2\sqrt{\pi}} \cdot \frac{a_1}{a_2} q_0 e^{-a_1^2 q_0^2 / 4a_2^2 t}.$$

$$\begin{aligned} E_2(t) &= h(t) * E(t) \\ &= \int_0^t E(\tau) h(t-\tau) d\tau \\ &= \int_0^t E(\tau) \frac{q_0}{2\sqrt{\pi}} \frac{a_1}{a_2} q_0 e^{-a_1^2 q_0^2 / 4a_2^2 (t-\tau)} d\tau \end{aligned} \quad (5.57)$$

5.3.4 Q-transformation with arbitrary driving forces

The above discussion has been largely limited to impulse type driving forces. This step is essential since any arbitrary forcing function can be expressed in terms of impulse functions. In practice, a true impulse function is difficult to obtain. Instead, excitation functions with finite duration have to be used. For example, in eddy current and ultrasound NDE, the excitation can be single frequency excitation, square pulse excitation or a raised cosine function. In this study, single frequency and square pulse excitations are used for studying the eddy current process; raised cosine functions are used in the ultrasonic NDE study.

Again, we study the one-dimensional case. The result can be extended easily to higher dimensional cases. The differential equations for diffusion and wave processes with general driving sources are:

$$\begin{cases} \frac{\partial^2}{\partial x^2} U_d(x,t) - a_1^2 \frac{\partial}{\partial t} U_d(x,t) = F_d(x,t) \\ \frac{\partial^2}{\partial x^2} U_w(x,t) - a_2^2 \frac{\partial^2}{\partial t^2} U_w(x,t) = F_w(x,t) \end{cases} \quad (5.58)$$

In terms of impulse functions for the driving forces, the equations can be rewritten as

$$\begin{cases} \frac{\partial^2}{\partial x^2} U_d(x,t) - a_1^2 \frac{\partial}{\partial t} U_d(x,t) = \int_0^\infty \int_0^\infty F_d(x_0, t_0) \delta(x-x_0) \delta(t-t_0) dx_0 dt_0 \\ \frac{\partial^2}{\partial x^2} U_w(x,t) - a_2^2 \frac{\partial^2}{\partial t^2} U_w(x,t) = \int_0^\infty \int_0^\infty F_w(x_0, t_0) \delta(x-x_0) \delta(t-t_0) dx_0 dt_0 \end{cases} \quad (5.59)$$

If the Green's functions for the diffusion equation and the wave equation are $g_d(x,t)$ and $g_w(x,t)$, respectively, then, the general solutions for the diffusion equation $U_d(x,t)$ and wave equation $U_w(x,t)$ can be expressed as

$$\begin{cases} U_d(x,t) = \int_0^\infty \int_0^\infty g_d(x_0, t_0) \cdot F_d(x-x_0, t-t_0) dx_0 dt_0 \\ U_w(x,t) = \int_0^\infty \int_0^\infty g_w(x_0, t_0) \cdot F_w(x-x_0, t-t_0) dx_0 dt_0 \end{cases} \quad (5.60)$$

As investigated before, if $F_d(x,t)$ represents the Q-transform of $F_w(x,t)$, then $U_d(x,t)$ is the Q-transform of $U_w(x,t)$. An alternate approach is to view $U_w(x,t)$ as the convolution of $g_w(x,t)$ and $F_w(x,t)$.

$$\begin{aligned} U_w(x,t) &= \int_0^\infty \int_0^\infty g_w(x_0, t_0) \cdot F_w(x-x_0, t-t_0) dx_0 dt_0 \\ &= g_w(x,t) * F_w(x,t) \end{aligned} \quad (5.61)$$

In the Laplace domain,

$$U_w(x, p) = g_w(x, p) \bullet F_w(x, p) \quad (5.62)$$

Let the Q-transform of $U_w(x, t)$ and $F_w(x, t)$ be $QU_w(x, t)$ and $QF_w(x, t)$, respectively. We already know that the Q-transform of $g_w(x, t)$ is $g_d(x, t)$. Then,

$$QU_w(x, t) = g_d(x, t) * QF_w(x, t).$$

When the diffusion driving force and the Q-transform of the wave driving force are identical, the diffusion field would correspond to the Q-transform of the wave field, on the condition that the boundary conditions also satisfy the Q-transform mapping rules.

When the diffusion driving force does not correspond to the Q-transform of the driving force associated with the wave field, then in principle, the diffusion field can still be obtained from the Q-transform of the wave field, with spectral compensation. Specifically, a wave signal is to be transformed into frequency domain using Fourier or Laplace transforms. In the frequency domain, each frequency component is to be multiplied by a factor of $(FFT_F_d(x, \omega)/FFT_F_w(x, \omega))$, where $FFT_F_d(x, \omega)$ is the Fourier transform of $F_d(x, t)$ and $FFT_F_w(x, \omega)$ is the Fourier transform of $F_w(x, t)$. Similarly, in the Laplace domain, each s component is to be compensated by a factor of $(S_F_d(x, s)/S_F_w(x, s))$, where $S_F_d(x, s)$ is the Laplace transform of $F_d(x, t)$ and $S_F_w(x, s)$ is the Laplace transform of $F_w(x, t)$. This spectrally compensated wave signal is then to be Q-transformed, to obtain the diffusion signal. However during the process, error is likely to be introduced as a result of spectrum zero crossings in the denominator.

5.4 Q-Transformation for Registration of the Ultrasonic and Eddy Current Data

In this section, we investigate the use of the Q-transform as a technique for registering the ultrasonic data with the eddy current data.

The source excitation used in the ultrasonic model is a raised-cosine waveform lasting for one cycle, i.e.,

$$F_w(x, t) = \delta(x)[1 - \cos(\omega_1 t)] \cos(\omega_0 t), \quad 0 \leq t \leq T, \quad (5.63)$$

in which, $f_0 = 10$ MHz,

$$\omega_0 = 2\pi f_0,$$

$$\omega_1 = \omega_0 / 3, \text{ and}$$

$$T = 1/f_1.$$

Therefore, in this case $T = 3.0 \times 10^{-7}$ s, i.e., $0.0 \leq q \leq 3.0 \times 10^{-7}$.

We calculate the signal response over a circular grid and assemble a three dimensional image with the axes corresponding to time, location and amplitude. This data is

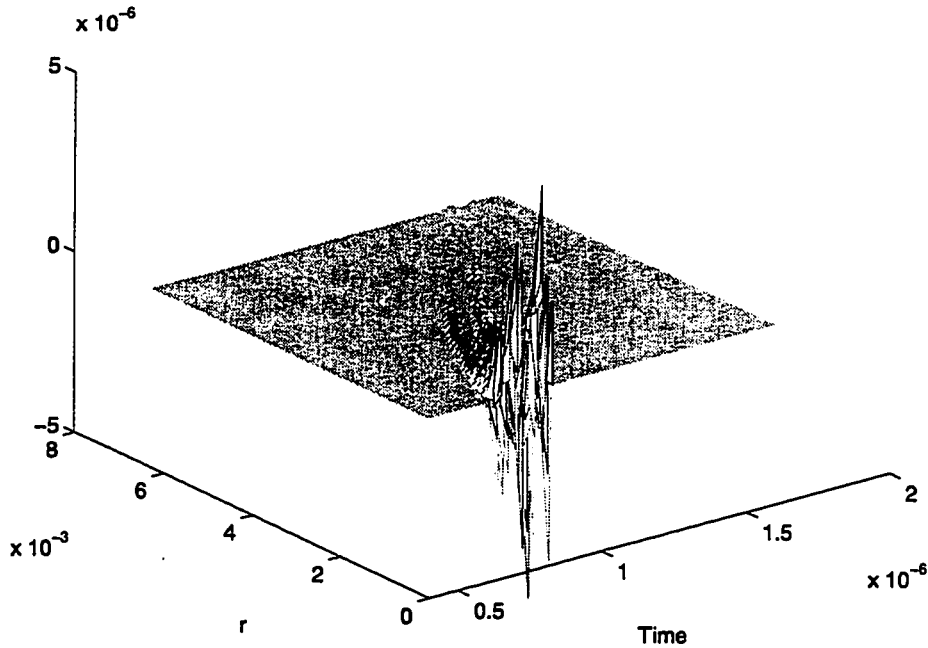


Figure 5.4. Ultrasonic scattering signal

then used for registration using the Q-transform. The ultrasonic signals due to a spherical flaw are shown in Figure 5.4.

In the eddy current setup, if the Fourier transform of the excitation signal $F_d(x, t)$ is $\Omega_d(x, \omega)$ and the change in the magnetic flux density at frequency ω is $B_z(\omega)$, then the total change in the magnetic flux density corresponding to the raised cosine excitation signal is

$$B_z(t) = \frac{1}{2\pi} \int_{-\infty}^{\infty} \Omega_d(\omega) B_z(\omega) d\omega \quad (5.64)$$

As derived earlier, we have the final form of the expression for $B_z(t)$:

$$B_z(t) = -\frac{3}{2\pi} \frac{1}{\Delta S_{z_2}} (Vol)\sigma \int_0^{\infty} \text{Im}[\Omega_d(\omega) \cdot \omega A_1(\omega) A_2(\omega) e^{j\omega t}] d\omega \quad (5.65)$$

The frequency components $\Omega_d(x, \omega)$ are calculated by calculating the FFT of the time domain signal $F_d(x, t)$.

Figure 5.5 shows the time dependent diffusion signal for a tiny spherical flaw at location $(r, z) = (0.0, -2.5 \text{ mm})$. The plot shows the change of magnetic field over time on the surface of the specimen, at each r location. The excitation current is a square pulse of duration $T = 1.0 \times 10^{-4}$ seconds.

The Q-transform of the wave signal is shown in Figure 5.6. We see that the

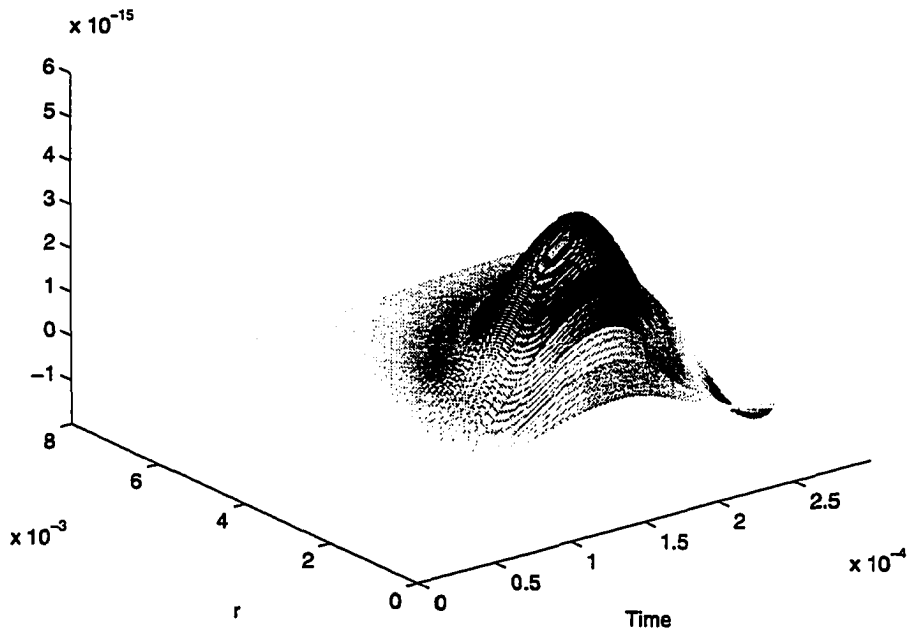


Figure 5.5. Eddy current change of magnetic field signal

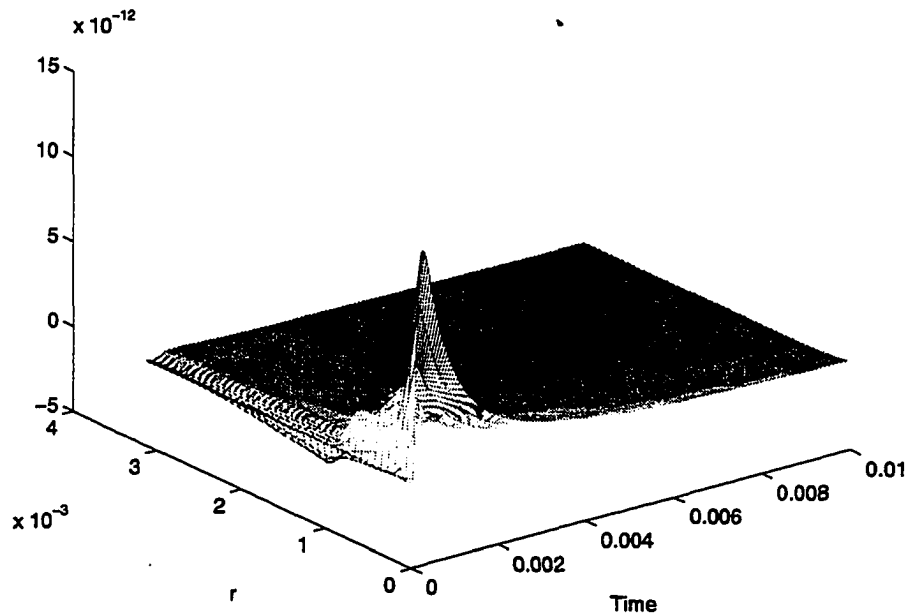


Figure 5.6. Q-transform of the ultrasonic wave scattering signal

transformed signal does not resemble the diffusion signal. At this stage, this is expected.

There are a few factors which contribute to the disagreement. First, the excitation signal in the ultrasonic wave scattering case is a raised cosine function, while the excitation current in the eddy current setup is a square pulse. The two signals are not related through the Q-transform. Therefore, the two field signals will not satisfy the Q-transform mapping either. Second, the method employed to define a common time origin for both the wave signal and the diffusion signal is arbitrary. A natural choice of time origin is to align the signals on the basis of the start of the excitation signal. In reality, this does not seem to lead to the right result, as further analysis shows. Third, there is a fundamental difference in signal shape

over space. Since the Q-transform is independent of spatial coordinates, it will not affect the signal spatial distribution of the signal.

As mentioned earlier, the difference in excitation signals will cause a mismatch between the Q-transformed wave signal and the diffusion signal. A condition for the field signals to satisfy the Q-transformation mapping is that the driving forces satisfy the same mapping rule. That is, the forcing function for the eddy current case has to be the Q-transform of the raised cosine function. This transformed signal is shown in Figure 5.7. The corresponding Fourier transform of the signal is shown in Figure 5.8.

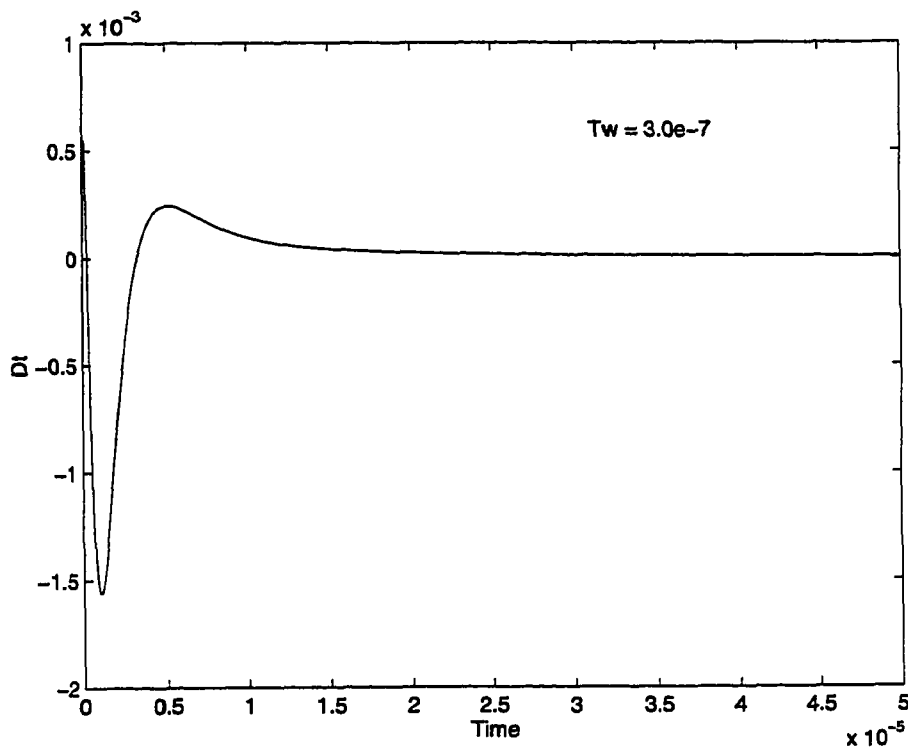


Figure 5.7. Q-transform of the raised cosine function with duration = 3.0×10^{-7} s

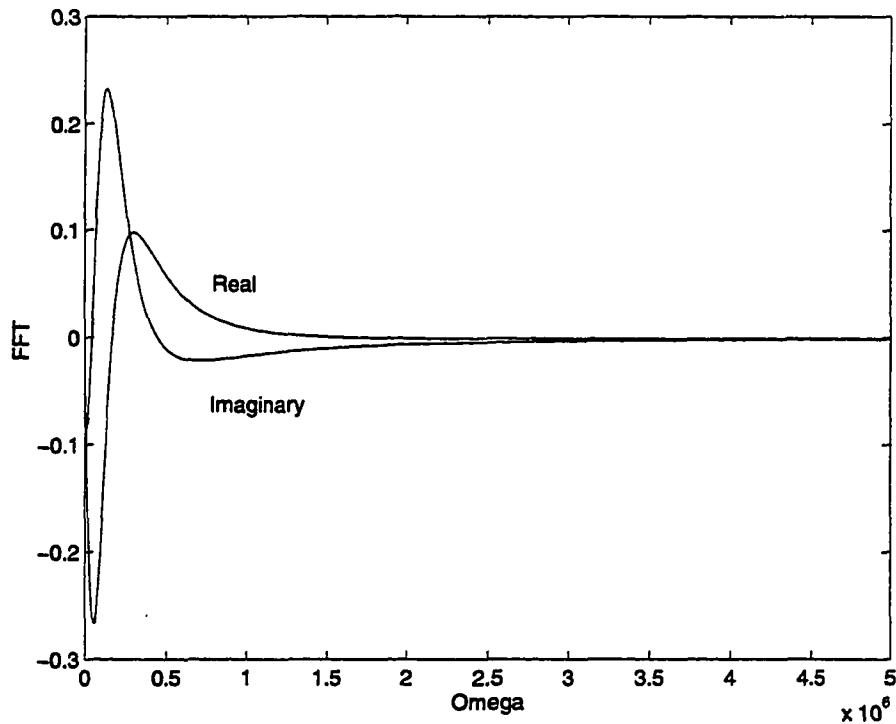


Figure 5.8. FFT of the raised cosine function Q-transform

The eddy current field generated by the spherical flaw with the new driving current excitation is again calculated. The calculation is based on the frequency components of the Q-transform of the raised cosine function. The resulting eddy current signal is shown in Figure 5.9.

Comparing this with the Q-transformed wave signal, we see that they still differ in shape and scale. Notice that the Q-transformed signal has a much larger region of support in time and has a shape that differs from the diffusion signal. The larger region of support of the Q-transformed signal is related to the signal range in the wave field. The wave signals

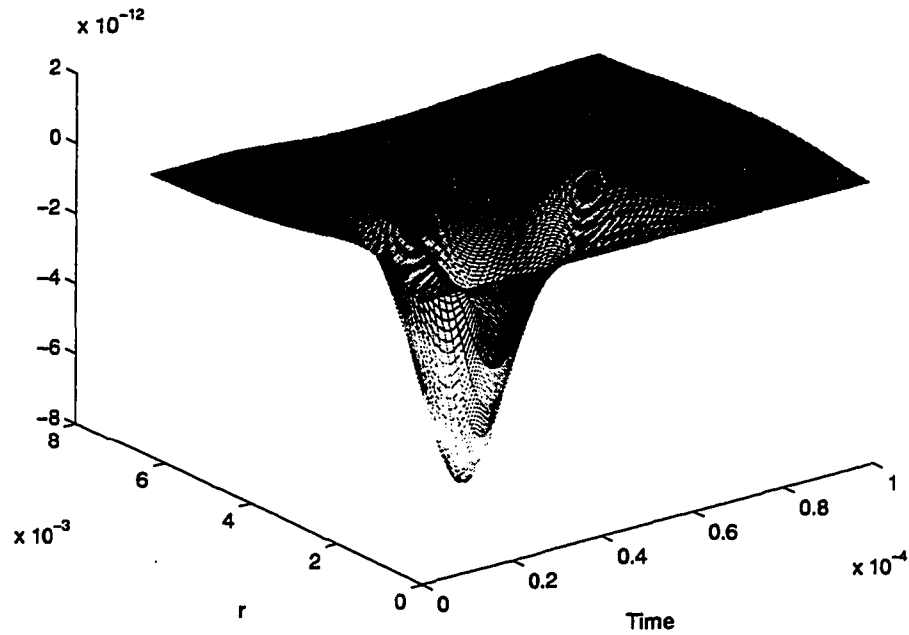


Figure 5.9. Eddy current signal with driving current corresponding to the Q-transform of the raised cosine function

have nonzero values around $q = 2.0 \times 10^6$ as is evident from the results shown in Figure 5.4.

In the Q-transformed result, the exponential term is $\left(\frac{a_1}{a_2}q\right)^2 / 4t$, and consequently the

transformed signals have nonzero values that extends approximately to $t \propto \left(\frac{a_1}{a_2}q\right)^2$. In this

case, the support of the transformed signal is about 0.01 seconds. This is much larger than the range of the eddy current signals, which is of the order of 1.0×10^{-4} s. In reality, the wave signal range is arbitrary and is dependent on the definition of the origin of the signals. As mentioned earlier, a shift in time of the wave signal smears out the corresponding Q-

transformed signal, thereby leading to much larger region of support. To further investigate this time shift effect, we examine the effect on the Q-transformed signal when the wave signal that has nonzero parts are shifted to the origin, before the transformation is implemented. The resulting Q-transformed signal is in shown Figure 5.10.

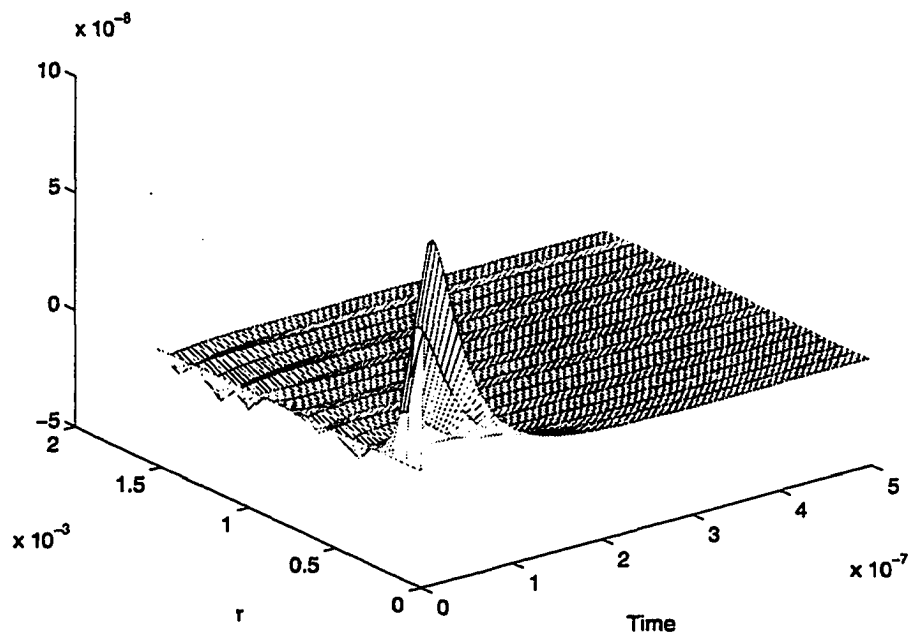


Figure 5.10. Q-transform of time shifted wave signals

The diffusion domain signal still appears to be different from the eddy current signal. One apparent difference lies along the r direction. Actually, the Q-transform does not directly alter the signal profile in the r direction. It does so indirectly through the change of each signal in time. Additionally, there is a fundamental difference between the ultrasonic signals and the eddy current signals with respect to their spatial distribution. For the

ultrasonic wave signals, the maximum scattering occurs at exactly the backward scattering direction ($r = 0$). In contrast, the eddy current signals are zero at the center $r=0$ position. The Q-transform operating on time does not alter this spatial difference. To overcome this difference, additional operations on the spatial coordinates may need to be performed.

As shown, the Q-transformed ultrasonic signals appear to be different from the eddy current signals, even though the driving forces match the Q-transformation condition and the experimental setups are identical. The flaw boundary conditions, however, are different for the ultrasonic and the eddy current cases. It is interesting to investigate the contribution of boundary conditions to the differences in the signals.

CHAPTER VI. CONCLUSIONS AND FUTURE WORK

The main objective of this dissertation is to undertake a theoretical feasibility study to determine if the Q-transform can be employed as a tool for data fusion. This chapter summarizes the work done in this dissertation and suggests areas for future research.

6.1 Summary of Dissertation

Electromagnetic models can play a vital role in enhancing an understanding of the physical processes that underly nondestructive evaluation phenomena. The novel analytical model developed in Chapter II is a very general model that is applicable for two-dimensional axisymmetric geometries. The model can be applied to study and analyze the following test configurations:

- 1) Excitation coil in free space.
- 2) Excitation coil above a conducting half plane.
- 3) Excitation coil above a conducting slab.

The governing equation underlying the model includes both the diffusion and the wave terms. Therefore, it can simulate a variety of test situations:

- Classical eddy current problems, which are essentially pure diffusion problems.
- High frequency wave propagation and radiation problems.

- Electromagnetic interactions in low conducting materials, where both the diffusion and the wave propagation take place.

The model allows simulation of defects in the test specimen. It computes the induced voltage by using current dipole model. The induced magnetic flux density is derived based on the same model. Once the magnetic flux density distribution is calculated, other terminal characteristics can be evaluated. Although the model assumes single frequency excitation, arbitrary excitation conditions can be simulated using Fourier decomposition techniques and superposing the results.

In Chapter III, wave scattering is studied. Although a first order analytical model of electromagnetic scattering is presented, the ultrasonic wave scattering process is actually modeled using the finite element method.

General issues relating to data fusion systems are presented in Chapter IV. The motivation for the application of data fusion concepts for combining eddy current and ultrasonic NDE data is discussed. In Chapter V, the central contribution of this dissertation, namely the issue of registration relating to eddy current and ultrasonic data is investigated. The use of the Q-transform as a tool for data registration is studied. The properties of Q-transforms are quantitatively analyzed. The effect of the Q-transform time shift property on data registration is investigated. A new modified Q-transform that is capable of accommodating differences in the coefficients is presented. Simulation results highlighting

causes for the reasons behind the discrepancy between the results are also presented in Chapter V.

6.2 Future Work

The work reported in this dissertation explores the interesting issue of ultrasonic and eddy current data registration. This dissertation presents an incremental step towards the development of a very novel phenomenological approach to the NDE data fusion. A lot of additional studies are still necessary. These include

- 1) Additional investigation of the effect of flaw boundary conditions on the output defect signals is required. This could provide information for performing the necessary steps required to obtain better registration results.
- 2) Issues concerning the stability of the transformation as well as methods for compensating for the effects of the time varying nature of the Q-transform need to be investigated.
- 3) This dissertation limits its study to the application of the forward Q-transform. A more interesting study that can be undertaken involves the use of the inverse Q-transform for mapping the diffusion field to a wave field. The attendant issues of stability need to be investigated.

BIBLIOGRAPHY

- [1] R. Palanisamy, "Finite Element Eddy Current NDT Model," Ph.D. Dissertation, Colorado State University, Fort Collins, Colorado, 1980.
- [2] C. V. Dodd and W. E. Deeds, "Analytical Solutions to Eddy-Current Probe-Coil Problems," *Journal of Applied Physics*, Vol. 39, No. 6, pp. 2829-2838, May 1968.
- [3] C. V. Dodd, W. E. Deeds and J. W. Luquire, "Integral Solutions to Some Eddy Current Problems," *International Journal of Nondestructive Testing*, Vol. 1, pp. 29-90, 1969.
- [4] B. P. Hildebrand and G. L. Fitzpatrick, "Inversion of Eddy Current Data Using Holographic Principles," *Review of Progress in Quantitative NDE*, Vol. 4A, pp. 507-515, 1985.
- [5] B. P. Hildebrand, A. J. Boland, and T. J. Davis, "Holographic Principles Applied to Low Frequency Electromagnetic Imaging in Conductors," *IEEE Proceedings of the 10th International Optical Computing Conference*, pp. 59-66, IEEE Computer Society Press, 1983.
- [6] L. Udpa and W. Lord, "Diffusion, Waves, Phase and Eddy Current Imaging," *Review of Progress In Quantitative Nondestructive Evaluation*, Vol. 4A, pp. 499-506, 1985.
- [7] J. H. Hippler, H. Ermert and L. V. Bernus, "Broadband Holography Applied to Eddy Current Imaging by Using Signals with Multiplied Phases," *Journal of Nondestructive Evaluation*, Vol. 12, No. 3, pp. 153-162, 1993.
- [8] Dominique Gibert, Benoit Tournier and Jean Virieux, "High-Resolution Electromagnetic Imaging of Conductive Earth Interior," *Inverse Problems*, Vol. 10, pp. 341-351, 1994.
- [9] J. M. Prince, B. P. Hildebrand and G. L. Hower, "The Eddy Current Probe as a Holographic Transducer," *Journal of Nondestructive Evaluation*, Vol. 12, No. 4, pp. 209-217, 1993.
- [10] Raidh Zorgati, Bernard Duchene, Dominique Lesselier and Francis Pons, "Eddy Current Testing of Anomalies in Conductive Materials, Part I: Qualitative Imaging via Diffraction Tomography Techniques," *IEEE Transactions on Magnetics*, Vol. 27, No. 6, pp. 4416-4437, 1991.
- [11] Raidh Zorgati, Bernard Duchene, Dominique Lesselier and Francis Pons, "Eddy Current Testing of Anomalies in Conductive Materials, Part I: Qualitative Imaging

- via Deterministic and Stochastic Techniques," *IEEE Transactions on Magnetics*, Vol. 28, No. 3, pp. 1850-1861, 1992.
- [12] P. A. Stucky, "Diffusion Effects in Eddy Current Nondestructive Evaluation," Thesis, Iowa State University, Ames, Iowa, 1991.
- [13] M. Burrows, "Theory of Eddy-Current Flaw Detection," Ph.D. Dissertation, The University of Michigan, Ann Arbor, Michigan, 1964.
- [14] Richard E. Duren, "General Fourier Solution and Causality in Attenuating Media," *IEEE Transactions on Electromagnetic Compatibility*, Vol. 36, No. 1, February 1994.
- [15] Henning F. Harmuth, "Propagation of Nonsinusoidal Electromagnetic Waves," Academic Press, Inc., New York, 1986.
- [16] K. H. Lee, G. Liu and H. F. Morrison, "A New Approach to Modeling the Electromagnetic Response of Conductive Media," *Geophysics*, Vol. 54, No. 9, pp. 1180-1191, Sept. 1989.
- [17] S. Ross, M. Lusk, W. Lord and J. Bent, "On Phase-Based Imaging of Eddy Current NDE," *Review of Progress in Quantitative NDE*, Vol. 14A, eds. D. O. Thompson and D. E. Chimenti, pp. 863-870, Plenum Press, New York, 1995.
- [18] S. Ross, M. Lusk and W. Lord, "A Transformation Approach to Imagine Eddy Current Nondestructive Evaluation Data," submitted to *IEEE Transactions on Magnetics*, August 1994.
- [19] S. Ross, M. Lusk, W. Lord and J. Bent, "A Comparison of Eddy Current and Millimeter Wave Imaging of Surface Flaws on Conducting Materials," *Review of Progress in Quantitative NDE*, Vol. 14A, eds. D. O. Thompson and D. E. Chimenti, pp. 629-636, Plenum Press, New York, 1995.
- [20] R. E. Hummel, "Electronic Properties of Materials," 2nd ed., Springer-Verlag, New York, 1992,
- [21] A. Akerman III, "Pyramidal Techniques for Multisensor Fusion," *Sensor Fusion V, Proceedings of SPIE*, Vol. 1828, pp. 124-131, 1992.
- [22] T. Huntsberger and B. Jawerth, "Wavelet Based Sensor Fusion," *Sensor Fusion VI, Proceedings of SPIE*, Vol. 2059, pp. 488-498, 1993.
- [23] R. Haberstroh and I. Kadar, "Multi-Spectral Data Fusion Using Neural Networks," *Signal Processing, Sensor Fusion, and Target Recognition II, Proceedings of SPIE*, Vol. 1955, pp. 65-75, 1993.

- [24] David L. Hall, "Mathematical Techniques in Multisensor Data Fusion," Artech House, Inc., Norwood, MA 1992.
- [25] D. L. Hall and J. Llinas, "A Survey of Techniques for CIS Data Fusion," *Proceedings of the Second International Conference on Command, Control and Communications and Management Information Systems*, pp. 77-84, Bournemouth, UK, IEEE, London, April 1987.
- [26] M. Herman and T. Kanade, "Incremental Reconstruction of 3D Scenes from Multiple Complex Images," *Artificial Intelligence*, Vol. 30, pp. 289-341, 1986.
- [27] R. C. Smith and P. C. Cheeseman, "On the Estimation and Representation of Spatial Uncertainty," *International Journal of Robotics Research*, Vol. 5(4), Winter, 1987.
- [28] O. D. Faugeras, N. Ayache and B. Faverjon, "Building Visual Maps by Combining Noisy Stereo Measurements," *IEEE International Conference on Robotics and Automation, San Francisco, CA*, April, 1986.
- [29] W. F. Clocksin and C. S. Mellish, "Programming in Prolog," Springer-Verlag, Berlin, 1981.
- [30] N. Nandhakumar, "Application of artificial Intelligence to Multisensory Vision," invited talk at *IEEE Computer Society Workshop on Artificial Intelligence for Computer Vision*, San Diego, June 5, 1989.
- [31] W. E. L. Grimson, "From Images to surfaces: A Computational Study of the Human Early Vision System," MIT Press, Cambridge, Massachusetts, 1981.
- [32] U. Dhond and J. K. Aggarwal, "Structure from Stereo: A Overview," *IEEE Transactions on System, Man, and Cybernetics*, SMC-19, No. 6,, pp. 1489-1510, 1989.
- [33] C. W. Tong, S. K. Rogers, J. P. Mills and M. K. Kabrisky, "Multisensor Data Fusion of Laser Radar and Forward Looking Infrared (FLIR) for Target segmentation and Enhancement," *Proceedings of SPIE*, Vol. 782, pp. 10-19.
- [34] P. Allen, "A Framework for implementing Multi-Sensor Robotic Tasks," *The Proceedings of DARPA Image Understanding Workshop*, pp. 392-398, 1987.
- [35] A. K. Jain and R. Hoffman, "Evidence-Based Recognition of 3-D Objects," *IEEE Transactions on Pattern Analysis and Machine Intelligence*, PAMI-10, No. 6, pp. 783-802, November 1988.

- [36] B. Gil, A. Mitiche and J. K. Aggarwal, "Experiments in Combining Intensity and Range Edge Maps," *Computer Vision, Graphics, and Image Processing*, Vol. 21, pp. 395-411, 1983.
- [37] J. K. Aggarwal and C. Chu, "The Issues, Analysis, and Interpretation of Multi-Sensor Images," *Multisensor Fusion for Computer Vision*, Springer-Verlag, pp. 37-62, 1993.
- [38] J. L. Crowley, "Principles and Techniques for Sensor Data Fusion," *Multisensor Fusion for Computer Vision*, Springer-Verlag, pp. 15-36, 1993.
- [39] R. Joshi and A. Sanderson, "Model-Based Multisensor Data Fusion: A Minimal Representation Approach," *Proceedings of the 1994 IEEE International Conference on Robotics and Automation*, pp. 477-484, 1994.
- [40] D. Terzopoulos, "Physically-Based Fusion of Visual Data over Space, Time, and Scale", *Multisensor Fusion for Computer Vision*, Springer-Verlag, pp. 63-69, 1993.
- [41] D. Heistrand, et. al., "An Automated Threat Value Model," *Proceedings of the 50th MORS*, March 1983.
- [42] P. Morse and H. Feshbach, "Methods of Theoretical Physics," McGraw-Hill, New York, 1953.
- [43] N. Ashby, "Relaxation of Charge Imbalances in Conductors," *American Journal of Physics*, 43:6, pp. 553-555, June, 1975.
- [44] E. J. Bochove, J. F. Walkup, "A Communication on Electrical Charge Relaxation in Metals," *American Journal of Physics*, 58:2, pp. 131-134, February 1990.
- [45] H. B. G. Casimir and J. Ubbink, "The Skin Effect," *Philips Technical Review*, Vol. 28, pp. 271-283, 1967.
- [46] D. J. Hagemaiier, "Eddy Current Standard Depth of Penetration," *Materials Evaluation*, Vol. 43, pp. 1438-1441, October, 1985.
- [47] A. E. Kennelly, F. A. Laws and P. H. Pierce, "Experimental Researches on Skin Effect in Conductors," *Trans. AIEE*, Vol. 34, pp. 1953-2018, 1915.
- [48] Z. Mottl, "The Quantitative Relations Between True and Standard Depth of Penetration for Air-Cored Probe Coils in Eddy Current Testing," *NDT International*, Vol. 23(1), pp. 11-18, February, 1990.
- [49] R. Mittra, O. Ramahi, A. Khebir, R. Gordon and A. Kouki, "A Review of Absorbing Boundary Conditions for Two- and Three- Dimensional Electromagnetic Scattering Problems," *IEEE Trans. on Mag.*, Vol. 25, pp. 3034-3040, July 1989.

- [50] M. Morgan and K. K. Mei, "Finite Element Computation of Scattering by Inhomogeneous Penetrable Bodies of Revolution," *IEEE Trans. on Ant. and Prop.*, Vol., AP-27, pp. 202-214, March 1979.
- [51] E. Marx, "Integral Equation for Scattering by a Dielectric," *IEEE Trans. on Ant. and Prop.*, Vol. AP-32, pp. 166-172, February 1984.
- [52] P. A. Martin and P. Ola, "Boundary Integral Equations for the Scattering of Electromagnetic Waves by Homogeneous Dielectric Obstacle," *Proceedings of the Royal Society of Edinburgh*, Vol. 123A, pp. 185-208, 1993.
- [53] D. Colton and R. Kress, "Integral Equation methods in Scattering Theory," Wiley and Sons, New York, 1983.
- [54] J. M. Jin and V. Liepa, "Application of Hybrid Finite Element Method to Electromagnetic Scattering From Coated Cylinders," *IEEE Trans. on Ant. and Prop.*, Vol. 36, pp. 50-54, January 1988.
- [55] T. Cwik, "Coupling Finite Element and Integral Equation Solutions Using Decoupled Boundary Meshes," *IEEE Trans. on Ant. and Prop.*, Vol. 40, pp. 1496-1504, December 1992.
- [56] C. A. Balanis, "Advanced Engineering Electromagnetics," John Wiley and Sons, New York, 1989.
- [57] Z. You, "Finite Element Study of Ultrasonic Imaging," Ph.D. Dissertation, Iowa State University, 1991.
- [58] R. Ludwig, "The finite Element Modeling of Ultrasonic NDT Phenomena," Ph.D. Dissertation, Colorado State University, 1986.
- [59] R. Ludwig and W. Lord, "Development in the Finite Element Modeling of Ultrasonic NDT Phenomena," *Review of Progress in Quantitative NDE*, Vol. 5A, eds. D. O. Thompson and D. E. Chimenti, pp. 73-81, Plenum Press, New York, 1986.
- [60] Z. You and W. Lord, "Finite Element Study of Elastic Wave Interactions with Cracks," *Review of Progress in Quantitative NDE*, Vol. 8A, eds. D. O. Thompson and D. E. Chimenti, pp. 109-116, Plenum Press, New York, 1989.
- [61] Z. You and W. Lord, "Numerical Modeling of Elastic Wave Propagation in Anisotropic Materials," *Review of Progress in Quantitative NDE*, Vol. 7A, eds. D. O. Thompson and D. E. Chimenti, pp. pp. 23-30, Plenum Press, New York, 1988.

- [62] W. Lord , S. Nath, Y. K. Shin and Z. You, "Electromagnetic Methods of Defect Detection," *IEEE Transactions on Magnetics*, Vol. 26, No. 5, pp. 2070-2075, September 1990.
- [63] S. S. Udpa and W. Lord, "A Fourier Descriptor Classification Scheme for Differential Probe Signals," *Materials Evaluation*, Vol. 42, No. 9, pp. 1136-1141, 1984.
- [64] L. Udpa and S. S. Udpa, "Eddy Current Defect Characterization Using Neural Networks," *Materials Evaluation*, Vol. 48, No. 3, pp. 342-347, March 1990.
- [65] I. Elshafiey, L. Udpa and S. S. Udpa, "A Neural Network Approach for Solving Inverse Problems in NDE," *Review of Progress in QNDE*, Vol. 11A, eds. D. O. Thompson and D. E. Chimenti, pp. 709-716, Plenum Press, New York, 1992.
- [66] W. Lord, "A Survey of Electromagnetic Methods of Nondestructive Testing," *Mechanics of Nondestructive Testing*, pp. 77-99, Edited by W. W. Stinchcomb, Plenum Press, New York and London, 1982.
- [67] B. D. Steinberg and H. M. Subbaram, "Microwave Imaging Techniques," *Wiley Series in Remote Sensing*, John Wiley and Sons, New York, 1991.
- [68] J. C. Bolomey and C. Pichot, "Microwave Tomography: From Theory to Practical Imaging Systems," *International Journal of Imaging Systems and Technology*, Vol. 2, pp. 144-156, 1990.
- [69] D. L. Waidelich, "Pulsed Eddy Currents," *Research Techniques in Nondestructive Testing*, pp. 383-416, Edited by R. S. Sharpe, Academic Press, New York, 1970.
- [70] J. L. Fisher and R. E. Beissner, "Pulsed Eddy-Current Crack Characterization Experiments," *Review of Progress in QNDE*, Vol. 5A, pp. 199-206, eds. D. O. Thompson and D. E. Chimenti, Plenum press, New York, 1986.
- [71] A. Pierce, "Wave Methods for an Inverse Problem in Diffusion," *Inverse Problems*, Vol. 2, pp. 205-217, 1986.
- [72] J. Yim, S. S. Udpa, L. Udpa and M. Mina, "Fusing Ultrasonic Image and Eddy Current Image Using Radial Basis Function," *Proceedings of the 3rd Annual Midwest Electro-Technology Conference*, pp. 10-13, Ames, IA, April 1994.
- [73] J. Yim, S. S. Udpa, L. Udpa, M. Mina and W. Lord, "Neural Network Approaches to Data Fusion," *Review of Progress in QNDE*, Vol. 14A, pp. 819-826, eds. D. O. Thompson and D. E. Chimenti, Plenum Press, New York, August 1994.

- [74] J. Yim, S. S. Udpa and L. Udpa, "Image Fusion Using Multi-Resolution Decomposition Techniques," *Proceedings of the 4th Annual Midwest Electro-Technology Conference*, Ames, IA, 1995.
- [75] K. Sun, S. S. Udpa, L. Udpa, T. Xue and W. Lord, "Registration Issues in Fusion of Eddy Current and Ultrasound NDE Data Using Q-Transformation," to be published in *Review of Progress in QNDE*, Seattle, WA, 1995.
- [76] W. Lord, Y. S. Sun, S. S. Udpa and S. Nath, "A Finite Element Study of the Remote Field Eddy Current Phenomenon," *IEEE Transactions on Magnetics*, Vol. 24, No. 1, pp. 435-438, January 1988.
- [77] K. H. Lee, G. Liu and H. F. Morrison, "A New Approach to Modeling the Electromagnetic Response of Conductive Media," *Geophysics*, Vol. 54, No. 9, pp. 1180-1192, September 1989.
- [78] K. H. Lee and G. Xie, "A New Approach to Imaging with Low-Frequency Electromagnetic Fields," *Geophysics*, Vol. 58, No. 6, pp. 780-796, June 1993.
- [79] J. C. Chao, "A boundary integral equation approach to three dimensional electromagnetic wave scattering problems," Ph.D. Dissertation, Iowa State University, 1994.
- [80] L. F. Richardson, "The Approximate Arithmetical Solution by Finite Differences of Physical Problems," *Trans. R. Soc.*, Vol. A210, pp. 307-357, London, 1910.
- [81] G. D. Smith, "Numerical Solution of Partial Difference Equation," Oxford University Press, London, 1965.
- [82] P. Zhou, "Numerical Analysis of Electromagnetic Fields," Springer-Verlag, New York, 1993.
- [83] R. C. McMaster, "Nondestructive Testing Handbook," Vol. 1, The American Society For Nondestructive Testing, Columbus, OH, 1959.
- [84] R. C. McMaster, "Nondestructive Testing Handbook," Vol. 2, The American Society For Nondestructive Testing, Columbus, OH, 1959.
- [85] W. K. H. Panofsky and M. Phillips, "Classical Electricity and Magnetism," Addison-Wesley, Reading, Mass., 1962.
- [86] J. Yim, "Image Fusion Using Multi-Resolution Decomposition and LMMSE Filter," Ph.D. Dissertation, Iowa State University, 1995.

- [87] I. Edwards, X. E. Gros, D. W. Lowden and P. Strachan, "Fusion of NDT Data," *British Journal of NDT*, Vol. 35, No. 12, pp. 710-713, Dec. 1993.
- [88] C. V. Dodd, C. C. Cheng and W. E. Deeds, "Induction Coils Coaxial With an Arbitrary Number of Cylindrical Conductors", *Journal of Applied Physics*, Vol. 45, No. 2, pp. 638-647, Feb. 1974.
- [89] D. Lovejoy, "Magnetic Particle inspection: A Practical Guide," Chapman & Hall, London, 1993.
- [90] C. E. Betz, "Principles of Magnetic Particle testing," Magnaflux Corp., Chicago, 1967.
- [91] M. M. Chao, "Neural Networks for Characterizing Magnetic Flux Leakage Signals," Thesis, Iowa State University, 1995.
- [92] W. Lord and J. H. Hwang, "Defect Characterization from Magnetic Leakage Fields," *British Journal of NDT*, Vol. , No. , pp. 14-18, 1977.
- [93] W. Lord, "Applications of Numerical Field Modeling to Electromagnetic Methods of Nondestructive Testing," *IEEE Transactions on Magnetics*, Vol. 19, No. 1, pp. 14-18, Nov. 1983.
- [94] S. S. Udpa, W. Lord and Y. Sun, "Numerical Modeling of Residual Magnetic Phenomena," *IEEE Transactions on Magnetics*, Vol. 21, No. 6, pp. 2165-2168, Nov. 1985.
- [95] W. Lord, J. M. Bridges, W. Yen and R. Palanisamy, "Residual and Active Leakage Fields Around Defects in Ferromagnetic Material," *Materials Evaluation*, Vol. 36, No. 8, pp. 47-54, July 1978.
- [96] X. R. Zhang, C. M. Gan, J.Y. Zhou, F. C. Wang and M. F. Ying, "Investigation of Thermal Diffusivity of Composite Materials by 'Mirage Effect'," *Review of Progress in QNDE*, Vol. 14A, pp. 467-474, eds. D. O. Thompson and D. E. Chimenti, Plenum Press, New York, August 1994.
- [97] P. R. Emeric and W. P. Winfree, "Thermal Characterization of Multilayer Structures from Transient Thermal Response," *Review of Progress in QNDE*, Vol. 14A, pp. 475-482, eds. D. O. Thompson and D. E. Chimenti, Plenum Press, New York, August 1994.
- [98] A. J. Bahr, "Experimental Techniques in Microwave NDE," *Review of Progress in QNDE*, Vol. 14A, pp. 593-600, eds. D. O. Thompson and D. E. Chimenti, Plenum Press, New York, August 1994.

- [99] H. C. Han and E. S. Mansueto, "Characterization of Dielectric Thin Films and Coatings," presented at *Review of Progress in QNDE*, Seattle, WA, July, 1995.
- [100] L. Udpa and S. S. Udpa, "Solution of Inverse Problems in Eddy Current Nondestructive Evaluation (NDE)," *Journal of Nondestructive Evaluation*, Vol. 7, Nos. 1/2, pp. 111-120, June 1988.
- [101] J. M. Mann, L. W. Schmerr and J. C. Moulder, "Neural Network Inversion of Uniform-Field Eddy Current Data," *Materials Evaluation*, Vol. 49, No. 1, pp. 34-39, Jan. 1991.
- [102] M. K. Hu, "Visual Pattern Recognition by Moment Invariants," *IRE Transactions on Information Theory*, Vol. IT-8, pp. 179-187, 1962.
- [103] R. Shankar, R. Williams and M. Avioli, "An Expert System for Power Plant NDE," *Review of Progress in QNDE*, Vol. 9A, pp. 665-672, eds. D. O. Thompson and D. E. Chimenti, Plenum Press, New York, August 1990.
- [104] L. D. Sabbagh and H. A. Sabbagh, "Eddy-Current Modeling and Flaw Reconstruction," *Journal of Nondestructive Evaluation*, Vol. 7, Nos. 1/2, pp. 95-110, June 1988.
- [105] D. K. Hsu, J. H. Rose, R. B. Thompson and D. O. Thompson, "Quantitative Characterization of Flaws Near a Surface Using Inverse Born Approximation," *Journal of Nondestructive Evaluation*, Vol. 3, No. 4, pp. 183-188, Dec. 1982.
- [106] A. J. Bahr and B. A. Auld, "An Electromagnetic Model for Eddy-Current Imaging," *Journal of Nondestructive Evaluation*, Vol. 7, Nos. 1/2, pp. 71-77, June 1988.
- [107] B. R. Groshong, G. L. Bilbro and W. E. Snyder, "An Eddy Current Transducer Model for Image Restoration," *Journal of Nondestructive Evaluation*, Vol. 10, No. 2, pp. 55-61, June 1991.
- [108] S. G. Ross, "Imaging and Inverse Problems of Electromagnetic Nondestructive Evaluation," Ph.D. Dissertation, Iowa State University, 1995.
- [109] E. Waltz and J. Llinas, "Multisensor Data Fusion," Artech House, Boston, 1990.
- [110] T. Xue, W. Lord and S. Udpa "Transient Fields of Pulsed Transducers in Solids," to be published in *RNDE*, Vol. 7, No. 1, 1996.
- [111] L. Filipczynski, "Scattering of a Plane Longitudinal Wave on a Free Surface of a Disc in a Solid Medium," *Proceedings of Vibration Problems*, Vol. 2, No. 1, pp. 41-54, 1961.

- [112] T. S. Lewis, D. W. Kraft and N. Hom, "Scattering of Elastic Waves by a Cylindrical Cavity in a Solid," *Journal of Applied Physics*, Vol. 47, No. 5, pp. 1795-1798, May 1976.
- [113] Y-H Pao and C. C. Mow, "Theory of Normal Modes and Ultrasonic Spectral Analysis of the Scattering of Waves in Solid," *Journal of Acoustical Society of America*, Vol. 59, pp. 1046-1056, 1976.
- [114] J. E. Gubernatis, E. Domany, J. A. Krumhansl and M. Huberman, "The Born Approximation in the Theory of the Scattering of Elastic Waves by Flaws," *Journal of Applied Physics*, Vol. 48, No. 7, pp. 2812-2819, July 1977.
- [115] J. M. Coffey and R. K. Chapman, "Application of Elastic Scattering Theory for Smooth Flat Cracks to the Quantitative Prediction of Ultrasonic Defect Detection and Sizing," *Nuclear Energy*, Vol. 22, pp. 319-333, 1983.
- [116] M. L. Moerdler and J. R. Kender, "An Approach to the Fusion of Multiple Shape From Texture Algorithms," *The Proceedings of IEEE Workshop on Spatial Reasoning and Multi-Sensor Fusion*, pp. 272-281, 1987.
- [117] S. S. Udpa, "Parametric Signal Processing for Eddy Current NDT," Ph.D. Dissertation, Colorado State University, 1983.
- [118] R. Ludwig and W. Lord, "Development in the Finite Element Modeling of Ultrasonic NDT Phenomena," *Review of Progress in QNDE*, Vol. 5A, pp. 73-81, eds. D. O. Thompson and D. E. Chimenti, Plenum Press, New York, 1986.
- [119] R. Ludwig and W. Lord, "A Finite Element Formulation for the Study of Ultrasonic NDT Systems," *IEEE Trans. on Ultrasonics, Ferroelectrics and Frequency Control*, UFFC-35, No. 6, pp. 809-820, 1988.
- [120] R. Ludwig and W. Lord, "A Finite Element Study of Ultrasonic Wave Propagation and Scattering in an Aluminum Block," *Material Evaluation*, Vol. 46, No. 1, pp. 108-113, 1988.
- [121] W. Lord, R. Ludwig and Z. You, "Developments in Ultrasonic Modeling with Finite Element Analysis," *Journal of Nondestructive Evaluation*, Vol. 9, pp. 129-143, 1990.